Individual dosimetry in disposal facilities for high-level nuclear waste

Zur Erlangung des akademischen Grades

Doktor der Ingenieurwissenschaften

der KIT-Fakultät für Maschinenbau
Karksruher Institut für Technologie (KIT)

genehmigte

Dissertation

von

Dipl.-Ing. Héctor Saurí Suárez

Tag der mündlichen Prüfung: 23. März 2018
Hauptreferent: Prof. Dr. Robert Stieglitz[1]
Korreferent: Prof. Dr. Horst Geckeis[2]

[1]Institut für Neutronenphysik und Reaktortechnik
[2]Institut für Nukleare Entsorgung

Erklärung

Hiermit erkläre ich, dass ich die vorliegende Arbeit selbständig angefertigt und keine anderen als die angegebenen Quellen und Hilfsmittel benutzt sowie die wörtlich und inhaltlich übernommenen Stellen als solche kenntlich gemacht und die Satzung des KIT zur Sicherung guter wissenschaftlicher Praxis in der jeweils gültigen Fassung beachtet habe.

Karlsruhe, den 22. Juni 2018

"Aw, people can come up with statistics to prove anything, Kent. Forfty percent of all people know that."

Homer Simpson

Abstract

Monte-Carlo methods offer an alternative to the traditional methods to estimate doses for persons occupationally exposed to radiation. In particular, they can be applied in the pre-job planning phase to optimize work-flows In this work a methodology to assess personal working in nuclear waste disposal facilities has been developed.

First, a validation of the selected tools has been performed. In the laboratory approach, it has been verified if the MCNP6 is able to reproduce experimental results and if simplifications of the model affect respective results. A neutron generator producing neutrons at 2.5 MeV is employed to simulate neutrons produced in spent nuclear fuel and neutron and gamma radiation are measured using a NE-213 detector. Layers of steel and polyethylene are positioned between the target of the neutron generator and the detector to mimic a shielding cask. Results of the measurements and corresponding simulations exhibit a good correlation confirming that MCNP6 can properly describe such scenarios. In the numerical approach, the impact of uncertainties in the cross section libraries on the simulated results has been studied, using the SAMPLER module of the SCALE package. Although results show that these perturbations impacts the obtained dose however, the magnitude is marginal and the confidence interval of calculated data to consider that the confidence interval of the results is practically not affected.

Second, the influence of different parameters of a nuclear waste disposal facility on the dose received by workers has been studied by numerical means. Therefore, POLLUX® casks with different spent nuclear fuel loadings are placed in different disposal galleries. The radiation field is calculated in the emplacement drifts as well as in a drift without surrounding walls to reveal the role of the backscattered radiation. Moreover, to study the effect of backscattered radiation on personal exposure, a mathematical phantom is used representing a worker inside a drift. Parametric simulations are performed where the orientations of the phantom to the cask is varied. Two conclusions are obtained. First, for the studied waste inventory neutrons dominate the radiation field. Second, the backscattered radiation plays an important role in such facilities. Therefore, it has been proposed that workers wear two dosimeters, one at the front and one at the back. The personal dose can then be derived by combining the dose rate obtained with both.

Finally, a comparison of the personal dose during the emplacement of casks in a rock salt drift and in a drift with a reinforcement of concrete has been performed. Since the load capacity per cask for disposal in clay is lower than that for disposal in a rock salt, the disposal of the same amount of spent nuclear fuel leads to a higher personal dose in a clay formation compared to emplacement in rock salt due to the significantly enhanced time required for disposal.

Kurzreferat

Monte-Carlo-Methoden bieten eine Alternative zu traditionellen Dosisabschätzungsmethoden. Sie können insbesondere im Vorfeld geplanter Arbeiten angewandt werden. In dieser Arbeit wurde eine Methodik entwickelt, um die Dosis für Mitarbeiter in Endlagerstätten für abgebrannte Kernbrennstoffe abzuschätzen.

Im ersten Teil wurde eine Validierung der ausgewählten Werkzeuge durchgeführt. Im Labormaßstab wurde verifiziert, ob MCNP6 in der Lage ist Experimente zu reproduzieren und ob Modellvereinfachungen die Ergebnisse beeinflussen. 2.5 MeV Neutronen wurden von einem Neutronengenerator produziert, um die von abgebrannten Brennelementen generierten Neutronen zu simulieren. Neutronen- und Gammastrahlung wurde mit einem NE-213 Detektor gemessen. Um einen Abschirmungsbehälter zu simulieren, wurden Polyethylen- und Stahlschichten zwischen dem Neutronengeneratortarget und dem Detektor positioniert. Ergebnisse der Messungen und entsprechenden Simulationen zeigten eine gute Korrelation auf und es wurde bestätigt, dass MCNP6 solche Szenarien in geeigneter Weise simulieren kann. In der numerischen Annäherung wurde untersucht, ob Datenunsicherheiten in den Wirkungsquerschnittsbibliotheken eine Auswirkung auf die Ergebnisse haben. Das SAMPLER-Modul des Programmpakets SCALE wurde benutzt, um zufällige Störungen in den Wirkungsquerschnittsdaten zu erzeugen. Obwohl die Ergebnisse zeigen, dass die Störungen einen Einfluss auf die erhaltenen Dosiswerte haben, ist dieser gering. Entsprechende Abweichungen liegen immer noch im Konfidenzintervall der Ergebnisse.

Im zweiten Teil wurde mittels MCNP6 der Einfluss verschiedener Parameter einer Einlagerungsstrecke auf die Dosis untersucht. POLLUX®-Behälter mit verschiedenen abgebrannten Brennelementbeladungen wurden in verschiedenen Einlagerungsstrecken untersucht. Das Strahlenfeld wurde in den Einlagerungsstrecken sowie in einer Strecke ohne Wände berechnet, um den Einfluss von der Rückstreuung aufzuzeigen. Weiterhin wurde ein mathematisches Phantom eingesetzt, um die Auswirkung der Rückstreuung auf die zuerwartete Personendosis zu analysieren. Dabei wurden Simulationen mit verschiedenen Phantomorientierungen zum Behälter durchgeführt. Es ergaben sich zwei Schlussfolgerungen: Erstens dominieren Neutronen beim untersuchten Abfallinventar die Dosis im Strahlenfeld. Zweitens spielt die Rückstreuung eine wichtige Rolle. Deswegen wird der Einsatz von zwei Personendosimetern auf Körpervorder- und Rückseite vorgeschlagen, um die von beiden Messgeräten ermittelte Personendosis zu kombinieren.

Zum Schluss wurde ein Personendosisvergleich während der Behältereinlagerung in eine Steinsalz- und Tonsteinstrecke durchgeführt. Da die Behälterbeladung in Tonstein geringer als in Steinsalz ist, führt eine Einlagerung der gleichen Menge abgebrannter Brennelemente in Tonstein zu einer höheren Personendosis als in Steinsalz.

Acknowledgement

My first work of thanks are for my advisers Prof. Dr. Robert Stieglitz and Prof. Dr. Horst Geckeis for giving me the opportunity to do my PhD Thesis at the Karlsruhe Institute of Technology. They have provided me with lots of valuable suggestions and efficient supervisions.

Furthermore, I extend my first thanks to my supervisors Dr. Frank Becker, Dr. Bo Pang and Dr. Volker Metz. Over the last three years they have provided my with lots of suggestions and they have oriented me through the necessary steps to write my thesis.

I am also very grateful to Dr. Vincenzo Romanello, Dr. Debora Leone and Dr. Wolfgang Klein for many very helpful discussions that helped me to solve many problems and also for our interesting discussions at the Mensa. Specially to Dr. Vincenzo Romanello for his support on MCNP and fuel calculations as well as his support with spectrum interpretations. I would like to thank also Andreas Benzler for helping me solving many problems with our cluster.

I would like to thanks the team of the Neutron generator of the Technische Universität Dresden for supporting us when conducting experiments in their facilities. Specially Dr. Axel Klix for his many suggestions and corrections when performing the experiments with the generator and the corresponding MCNP simulations. I extend my appreciation to all the members of the ENTRIA-Plattform for our interesting discussions and for make me see that sometimes science alone cannot solve a problem.

A very special thanks to my family. Their love, help and continuous support accompany me throughout the whole time. This thanks goes more intensely to Nadia because she was by my side every day and was able to make me smile even in the darkest hours. I couldn't have done it without them. Finally I would like to thank my friends from KIT Schwimmteam Karlsruhe. They have made my stay in Karlsruhe much funnier and made me feel at home.

This study was financially supported by the German Federal Ministry of Education and Research (BMBF) in the context of the ENTRIA project (grant number 15S9082E).

Contents

Abbreviations

ALARA	As Low As Reasonably Achievable
BOMAB	BOttle MAnnikin ABsorber
CLD	Concrete Lining Drift
ENDF	Evaluation Nuclear Data File
EW	Exempt Waste
FA	Fuel Assemblie
FIA	Free In Air
FWHM	Full Width at Half Maximum
FR	Fuel Rod
GEB	Gausian Energy Broadenig
$\dot{H}^*(d)$	ambient dose equivalent rate
$\dot{H}^*(10)$	ambient dose equivalent rate at 10 mm
HLW	High-Level Waste
$\dot{H}_p(d)$	personal dose equivalent rate
$\dot{H}_p(10)$	personal dose equivalent rate at 10 mm
HZDR	Helmholtz Zentrum Dresden Rossendorf
IAEA	International Atomic Energy Agency
ICRP	International Commission on Radiological Protection
ICRU	International Commission on Radiation Units and measurements
ILW	Intermediate-Level Waste
JEFF	Joint Evaluated Fission and Fusion
JENDL	Japanese Evaluated nuclear data library

LNT Linear no-threshold model

LLW Low-Level Waste

MCNP Monte Carlo N-Particle

MOX Mixed OXide

NPS Number of Particles per Simulation

PWR Power Water Reactor

RSD Rock Salt Drift

SF Spontaneous Fission

SNF Spent Nuclear Fuel

TUD-NG Neutron generator of the Technische Universität Dresden

UOX Uranium diOXide

VLLW Very Low-Level Waste

VSLW Very Short Lived Waste

Dedicado a mis padres y a mi abuela María. Gracias a vuestra educación he llegado a ser lo que soy hoy en día. Aunque este lejos siempre os querre como si estuvierais a mi lado.

Chapter 1

Introduction

1.1 Problem statement

A long-term and safe disposal of heat generating nuclear waste is a challenge for the research community since there are many uncertainties in different fields such as technological, legal, social, environmental and ethical aspects.

The traditional methods to estimate personal dose of occupational exposure are not precise enough, since they are generally based on averaged measurement data. Moreover, many of these methods are based on measurement techniques with passive dosimeters, which mean that the dose received by the workers is recorded during their working activities, and only after the dose has been recorded, it is possible to perform an assessment of the radiological risk related to the received dose. Numerical simulations offer a powerful alternative to occupational radiation protection since they can be used to estimate the doses for workers in the pre-job planning phase. Monte-Carlo codes can be used to simulate working activities and provide dose estimations.

Most concerns related to nuclear waste disposal are connected with the possible radiation exposure of the population as a consequence of the potential radionuclide release from a repository to the biosphere in the long-term after thousands of years, while less attention is draw to possible dose exposure to workers during operational phase. However, certain activities performed in a nuclear waste disposal or storage facility might lead to elevated exposure of workers during the operational phase of a repository. Therefore, it is advisable to keep a surveillance of the occupational radiation exposure.

1.1.1 Challenges, requirements and boundary conditions

Nuclear waste comes mainly from the use of nuclear energy to produce electricity but also from other applications like research, industry and medicine. An important amount of this waste is composed of radionuclides with long half-lives that can be a risk to the population and the environment and must be properly disposed.

The disposal of highly radioactive waste is therefore, a primarily challenge since the selection of a location for a repository is socially very controversial and critically discussed and since a proof of safety over a period of 1 million years is required. One of the most accepted options is the disposal in deep geological formations (BMWi 2015). According to (Röhlig et al. 2014), with the actual and in short future expected technology, the disposal in deep geological formations is independent of other extra measures like partitioning, conditioning, transmutation or long-term intermediate storage, the only way to dispose the waste safely and in the long term as well as environmentally friendly.

Although the disposal in deep geological formations is feasible with the actual technology, the selection of the suitable location is not trivial since there are many boundary conditions (geological, technical, socio-technical, and socio-economical, etc.) that affect this decision. Hence the actual challenge is to evaluate these boundary conditions to determine their impact in the location selection.

The selection of the host rock as well as the proper location of a repository must be made according to the geoscientific criteria defined by the local regulations like the "Standortauswahlgesetz" in Germany (StandAG 2017), which are intended to guarantee the best possible safety for a repository and aim at long-term safety in order to protect the population from radiation exposure. The optimization of the radiation protection for employees during the operational phase, which is ensured by properly planning the work processes, the provision of shields, etc., is also required. However, it is not the only parameter to be taken into account and does not definitely influence the selection of a repository site or a host rock.

In a disposal facility, the main contributor to the dose received by the workers is the radiation coming from the nuclear waste stored in shielding casks, but there are also many other boundary conditions that can have an influence on the received dose. The study of these parameters is, as described in the following sections, the main aim of this thesis.

1.1.2 The ENTRIA Platform

The ENTRIA platform (in German "**ENT**sorgungsoptionen für **R**adioaktive Reststoffe: **I**nterdisziplinäre **A**nalysen und Entwicklung von Bewertungsgrundlagen") was set up to gather experts of the various areas to compare three different nuclear waste management options, i.e., final disposal in deep geological repository without provisions of retrieval, final disposal in deep geological repository with provisions of monitoring and retrieval, as well as long-term above-ground storage from different points of view (technological, legal, social etc.) (Geckeis et al. 2012).

Eleven German research institutes and universities as well as a Swiss partner work together in the ENTRIA platform. The aim is to be a research group independent from politics, operation companies, and stakeholders. However, the objective of ENTRIA is not to state the suitability of a concrete location for a nuclear waste disposal facility, but to stablish some guidelines and criteria that can help to take this decision (Röhlig et al. 2014).

This thesis is framed in the ENTRIA working group interdisciplinary risk research. This transversal project studies the possible risks in the deep geological options from different perspectives. A list of the work published during the development of the thesis can be found in Appendix D.

1.2 Objectives of the thesis

The aim of this thesis is to develop a methodology that can be used to asses personal working in nuclear waste disposal facilities. Since many parameters have an influence in the dose received by workers in such facilities, the methodology will be orientated to elucidate the impact that these parameters have on workers. The operational application of the developed methodology will be the estimation of the personal dose during working activities in the different nuclear waste disposal options and to compare different disposal options.

To develop and apply the methodology is not enough to confirm that there are available tools. It is also necessary to prove that the selected tools can properly represent the exposure that workers may receive The second objective of this thesis is therefore, to validate the tools and to prove that the different uncertainties do not distort the obtained results. Two approaches are followed. First, the possible distortions due to the uncertainties in the simulations of a real scenario must be quantified. For this purpose, experiments are performed and compared with simulations with the selected codes. The

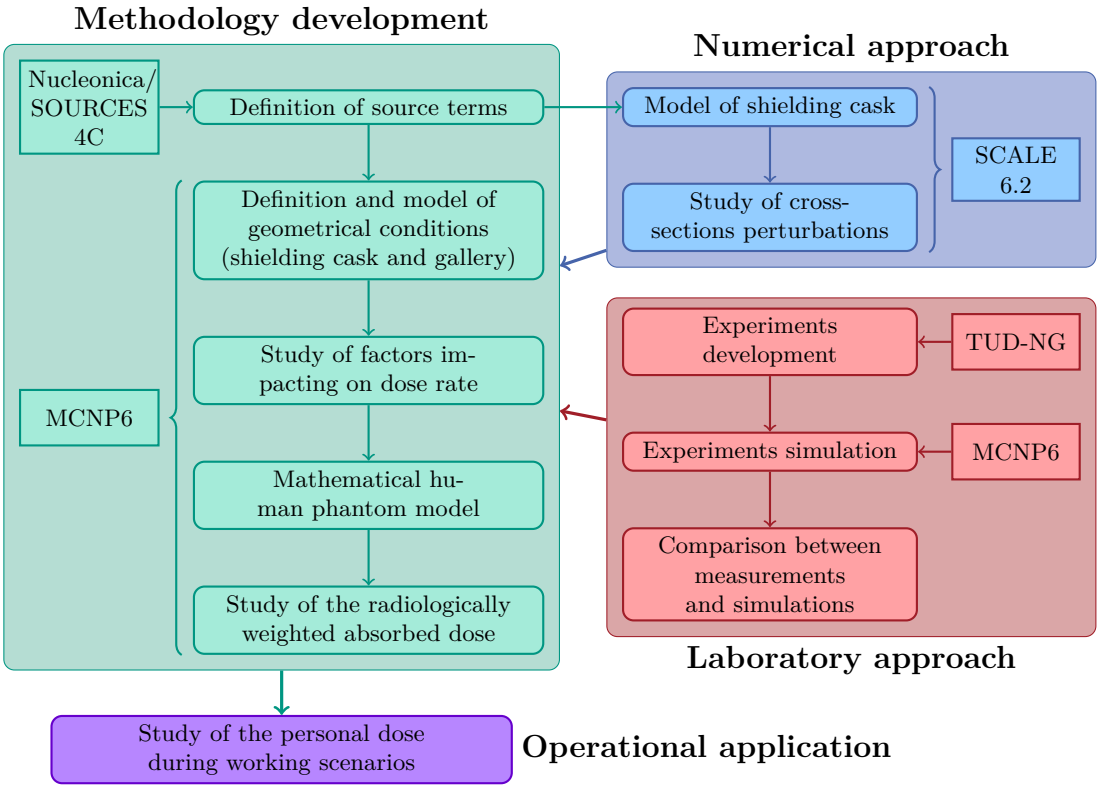

FIGURE 1.1: Flow diagram of the developed work showing the main steps in the methodology, numerical and laboratory approaches.

second approach studies the uncertainties in the code itself to determine if variations of them will have an impact in the results.

If both approaches are validated, the developed methodology can be considered appropriate to compare different disposal scenarios. Figure 1.1 includes a flow diagram with the main steps performed in this work for each approach.

1.3 Organization of the thesis

In chapter 2 an overview of the different disposal options with their advantages and disadvantages is presented. Furthermore, for the concept of deep geological repository the characteristics of the candidate host rocks are explained. Also in chapter 2, the generic characteristics of shielding casks and the specifications of the POLLUX® cask are presented. Finally, the concept of radiological protection is introduced.

The required tools to develop the methodology are explained in chapter 3. The Monte-Carlo and the uncertainty and sensitivity analysis methods are introduced and an overview of the employed codes to perform these methods is presented. Finally, the applications of these methods to the external dosimetry is discussed.

In chapter 4 a detailed description of the neutron, gamma and beta sources that has been employed in the calculations of chapter 6 and chapter 7 is presented.

The chapter 5 and chapter 6 take care of the laboratory and numerical approaches described in the previous section. The experiments performed with the Neutron generator of the Technische Universität Dresden (TUD-NG) and the comparison with the simulations performed with MCNP are presented in chapter 5. In chapter 6 the uncertainty and sensitivity analysis of the cross-section libraries with the package SCALE and a comparison with MCNP is presented.

Once the interval of confidence of measurements and calculations has been establish, the dose assessment in a deep-geological repository can be performed. This is the highlight of chapter 7. In this chapter, the ambient dose and the personal dose is studied. The influence of different parameters on the measured dose, i.e. the disposed waste, the selected host rock or the position of the worker, are discussed. Finally, as example of the operational approach, a comparison between the absorbed dose during a working scenario in different host rocks is conducted.

To conclude this thesis, a resume of the obtained results will take place in chapter 8. An overview of the future possible working lines to improve the developed methodology and the application area in radiation protection are also discussed.

Chapter 2

Nuclear waste disposal options

2.1 Nuclear waste categories

The International Atomic Energy Agency (IAEA) classifies nuclear waste in six categories from lower to higher riskiness in terms of radiological protection. A detailed classification of which waste is included in each category and what are the measurements to be followed can be found in (IAEA 2010). The categories head to:

- Exempt Waste (EW): Waste that cannot properly be considered as radioactive waste. Waste that enters in this category no longer has to follow special radiation protection measures and can be handled as normal waste.
- Very Short Lived Waste (VSLW): Waste in this category is composed by radionuclides with a very short half-life. It needs to be stored in special conditions for a limited period up to a few years. After that time it enters in the EW category.
- Very Low-Level Waste (VLLW): Waste composed by short half-life radionuclides but it also includes small amounts of longer half-life radionuclides. Therefore, it cannot be directly considered as VSLW or EW. It has to be disposed in special facilities, but due to its low activity does not require high regulatory control. This waste is usually stored in above-ground facilities.
- Low-Level Waste (LLW): Waste inside this category already requires a special isolation for periods of up to a few hundred years. This class includes waste with high activity and short lived radionuclides but also long lived radionuclides with low activity. Usually it is enough to store this waste in above-ground facilities, but it can also be disposed in depth disposals.

- Intermediate-Level Waste (ILW): This category already includes waste with long lived radionuclides but low heat emission. Therefore, depth disposal at depths around ten to hundred meters is recommended.

- High-Level Waste (HLW): Waste in this category has a very high activity and generates a significant amount of heat that must be dissipated. Depth disposal of HLW requires usually stable geological formations at several hundred meters. The Spent Nuclear Fuel (SNF) of nuclear power plants is included in this category.

As shown in Table 2.1, the largest amount of nuclear waste can be handled as LLW (in the table VSLW and VLLW has been considered as LLW). For this waste near surface disposals at ground level are enough to keep the waste safe (IAEA 2010) and many countries already operate such facilities. However, countries like Germany require a deep geological disposal for LLW. On the other side, the HLW represents a very small volume of the total amount of generated nuclear waste. However, it is responsible for almost all the radiative emissions. Currently, the majority of this waste is stored in interim storage facilities, awaiting for an option for ultimate disposal. Since the disposal of HLW represents currently the main social challenge, it is the focus of this thesis.

TABLE 2.1: Volume and activity of the different types of radioactive waste (World Nuclear Association 2017).

	Volume (%)	**Radioactive content** (%)
LLW	90	1
ILW	7	4
HLW	3	95

2.2 Nuclear waste disposal options

As described in (Röhlig et al. 2014), the disposal of nuclear waste should meet at least the following requirements:

- Protection of population, workers, and environment from radio-toxic material.

- Protection of population and staff from direct radiation.

- Avoidance of a possible chain reactions of the fissile material.

- The generated heat should be properly dissipated to avoid damages in the structures of the cask and to preserve the integrity of the disposal facility.

- Waste should be protected against unauthorized access.
- Prevention of possible sabotage.

To consider a nuclear waste disposal option as reliable it must satisfy all the above described requirements. If necessary, technical measures must be employed matching all required criteria.

2.2.1 Rejected Options

In the last decades many options have been proposed to dispose HLW. The majority of these options have never been realized due to technological limitations, or because they are internationally not accepted. Others were just applied for a period of time and rejected due to changes in international laws or because they lost sustainability. Some of the options scope:

- Disposal in the outer space: It consists in the launch of space shuttles transporting nuclear waste into space. It was investigated by the NASA in the late 1970s and early 80s (Burns et al. 1978). Due to the high costs and the risk of waste dispersion in case of a launch failure it was abandoned.
- Rock melting: The method consists in the introduction of capsules with nuclear waste at 2 km depth. Once there, the heat emitted by the waste would melt the rock around it, burying the capsule deeper. At the same time, the rock above the waste will solidify again (Logan 1974; Heuze 1981). This option is currently not implemented anywhere since it presents drawbacks related to safety issues like heat induced fracturing/fissuring leading to water access.
- Sub seabed disposal: Radioactive waste would be buried in a geological setting under the seabed. The repository would be accessed from land or an offshore structure (Hollister et al. 1981; Bishop et al. 1974). Theoretically it would be possible to monitor and retrieve the waste (Hinga et al. 1982). However, the method was never implemented due to the impossibility to predict consequences from radionuclide dispersion and it is forbidden by the international agreements (*International Convention on the Prevention of Marine Pollution by Dumping of Wastes and Other Matter* 1972).
- Disposal at subductive zone: In a subductive zone a tectonic plate slides under another one. Nuclear waste can be disposed in these zones and it would be carried to the earth mantle (Uyeda 1984). Theoretically, the main advantage of this

method is the impossibility of return of the radionuclides since their average diffusion (1 mm/year) is slower than the subduction rate (2.1 cm/year) (Rao 2001). However, the method is not implemented anywhere since uncertainties due to seismic and volcanic events in the subduction zones are present and is not permitted by international agreements.

- Disposal in ice sheets: Casks with HLW would be placed in stable ice formations. The heat generated by the waste would melt the ice and be drawn deep into the ice sheet. The ice would refreeze above the cask creating an isolation barrier (B. Philberth 1961; K. Philberth 1977). However, a possible climate changes may affect these ice formations and be no more stable. This method is forbidden by the Antarctic Treaty (Council et al. 1959).

- Direct injection: Consist in the injection of liquid radioactive waste into a layer of rock deep underground. It was investigated by the USA but abandoned for deep geological disposal. Russia implemented this technique from 1963 to 2002 (Rybalchenkoa et al. 2005). The long-term evolution of such systems is unclear and may be a risk of groundwater pollution.

- Disposal in boreholes: Inspired on the direct injection method, it consist in drilling deep holes (5 km or deeper) to dispose cask with HLW. Afterwards, the bore would be filled with some special layers (mainly crushed rock and cement) (Beswick 2008; Brandy et al. 2009). However, the required technology is not available and it is not expected to be ready in short (Bates et al. 2014).

- Multinational repositories: Not all countries are suitable to store their own radioactive waste. Some are limited in area or have not enough radioactive waste to make the construction and operation of their own repositories economically feasible. International repositories would be located in a host country that would accept waste from several countries (Chapman et al. 2014). However, the actual regulations rule that each country has to be responsible for its own nuclear waste.

All the options explained above were rejected since they do not achieve some of the requirements that a repository of nuclear waste should have. Currently, the options in discussion in the majority of countries are long-term above-ground storage and deep geological repository with and without provision of monitoring and retrieval. These three options are explained in detail in the following sections.

2.2.2 Long-term above-ground storage

For this disposal option, mainly technical barriers are employed to contain the nuclear waste (Thomauske 2002). These facilities are usually not considered as a final solution but as intermediate storage for several decades to a few hundred years. After this period, if any new final solution is available, nuclear waste should be disposed in deep geological repositories (Röhlig et al. 2014).

These facilities have the advantage that they are easier to construct than deep-geological repositories. Moreover waste can be easily retrieved if necessary. Their construction cost are much lower than other options, but they have significant operating costs since regular maintenance is required. Another disadvantage is that waste is less protected against natural catastrophes or unauthorized access. Moreover, they present some important socio-political challenges that make them inappropriate as final disposal option. The institutional control cannot potentially be guaranteed for extended operational times and they imply also that a great amount of knowledge has to be transferred to the future generations to guarantee a proper operation (IAEA 2003).

Many countries already operate this type of installations. Countries like Germany have central and local storage facilities near their power plants (Thomauske 2002) forseen to be operated for about 40 years.The Netherlands have a central storage facility (Figure 2.1), where all the nuclear waste of the country is stored (Kastelein et al. 2005). For this facility, a possible operation time up to 300 years is envisaged. For countries with small amounts of nuclear waste this centralized storage is easier that for countries with facilities producing nuclear waste across the country since it implies a higher amount of transport (Röhlig et al. 2014).

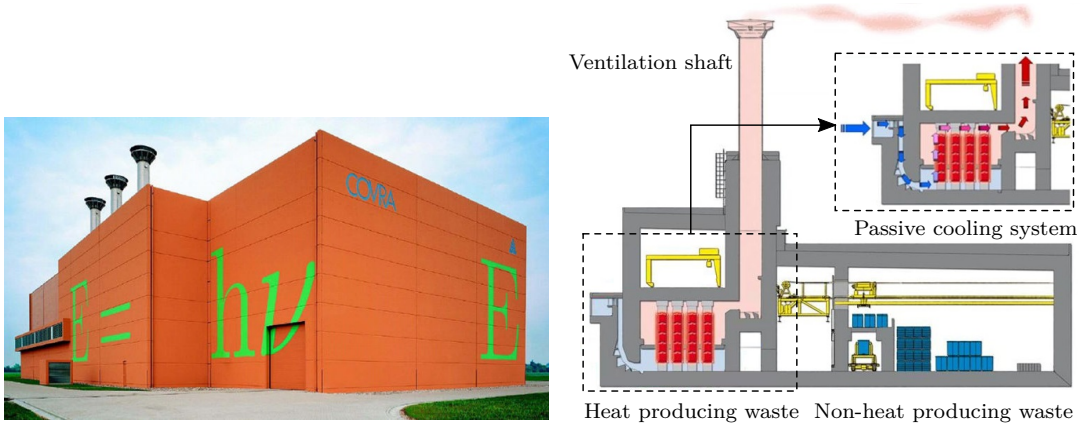

(a) Outside view (extracted from (Hardy Stevenson and Associates Limited 2008))

(b) Cross-section view (extracted from (Powering the Grid 2011))

FIGURE 2.1: Long-term above-ground storage facility in Netherlands (HABOG) for LLW, ILW, and HLW

2.2.3 Deep geological repository without provision of retrieval

Deep geological repositories use the long stability of geological formations to dispose the nuclear waste where a combination of engineered and natural barriers keeps it isolated (Röhlig et al. 2014; World Nuclear Association 2017). The nuclear waste is disposed several hundred meters deep in excavated drifts or boreholes (Figure 2.2). If no provision of retrieval is intended, once the waste is allocated the drift or borehole is filled with material again and the access installations are dismantled and sealed (World Nuclear Association 2017).

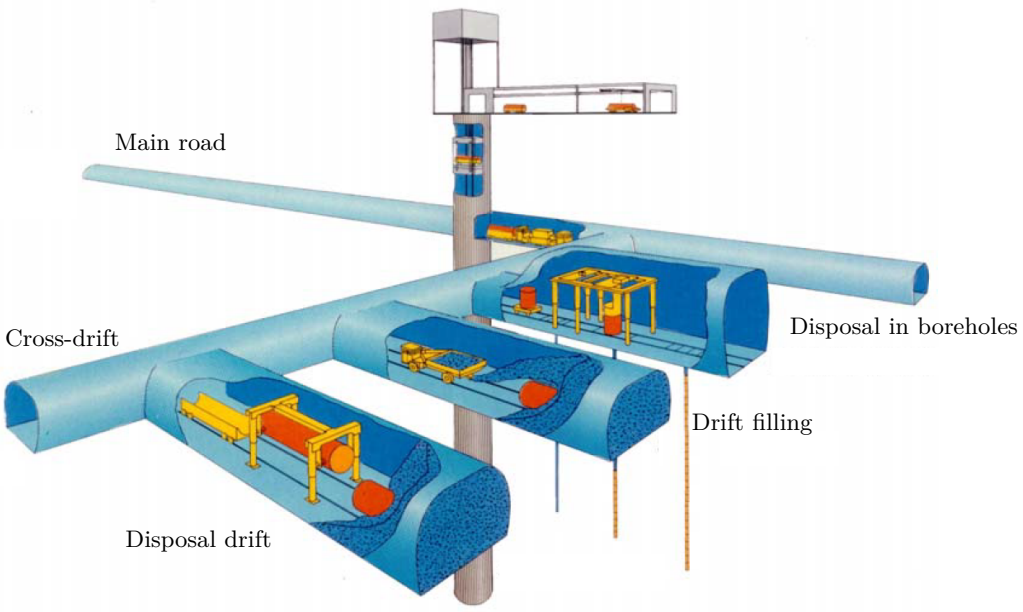

FIGURE 2.2: Representation of a possible deep geological repository for HLW and operational equipment for transfer and disposal. Extracted from (Bollingerfehr, Filbert and Reinhold 2009)

In contrast to above-ground storage facilities, external ambient and social changes like long-term climate changes, catastrophes, wars or changes in the governmental policies have a lower impact an a geological disposal. Moreover, once the repository is closed the risk unauthorized human intrusions is reduced (Röhlig et al. 2014).

The main disadvantage from this option is the complexity of the construction and the associated costs. Moreover, once the repository is sealed, the retrieval is very complicated and monitoring is impossible.

2.2.4 Deep geological repository with provision of monitoring and retrieval

Unlike the disposal without prevision of retrieval, this option considers the possibility to extract the nuclear waste in the future. The idea is similar to the retrieval without provision, but the drifts are kept open, or if they are closed, it is done in a way that the waste can been relatively easily retrieved.

This option is the favourite for many countries since it keeps the advantages of the disposal in host rocks (protection against external changes, unauthorized human intrusions, etc.) but it adds the advantage that nuclear waste can be retrieved in the future if new technologies allow a better solution or if new findings disqualify the site as safe disposal option (Röhlig et al. 2014; U.S. Department of Energy 2014).

Deep geological repositories and above-ground storage facilities require personal working in the proximity of HLW. Therefore, a study of the radiological impact is necessary to determine how the surrounding conditions affect to both the individual and the collective received dose. In (Zhang 2011), a study for quantifying the radiation field in an above-ground storage facility is performed. Furthermore, facilities of this class are already operational in many countries allowing to perform direct measurements. Hence, this work would only focus in the study of the deep geological repository since it is the favourite option for long time disposal but many variables still have to be studied.

2.3 Host rock characteristics

The host rock is in many cases the main barrier to contain the high-level nuclear waste in a deep geological repository. Therefore, it should be selected carefully. A deep geological repository requires a proof of safety over a period of 1 million years which implies that the selected host rock should have a high stability and should be located in a region with low geodynamical impacts (earthquakes, tectonic plate movements, etc.). Therefore, only a few areas are good candidates to allocate a deep geological repository.

According to the last version of the "Standortauswahlgesetz" (StandAG 2017) the temperature at the outer surface of the disposal cask should not exceed 100 °C. Moreover because of the arrangements for retrievalbility and monitoring the air temperature in the open drifts is limited to 52 °C (Leon Vargas et al. 2017). This should ensure the occupational health of the staff operating the repository.

Another important characteristic is the water permeability. A geological repository should have a very low water permeability to avoid the access of water inside the drift

or at least minimize the amount of water. If water finally has access to the drift, it will enter in contact with the disposal cask leading to a corrosion of the cask and a corresponding production of gases. If the host rock is not able to absorb or dissipate these gases, pressure increases and could affect to the barrier integrity. A long term cask corrosion may affect its integrity and radionuclides can be released. Therefore, to restrict the propagation of radionuclides, it is necessary a host rock with high sorption capacity.

Figure 2.3 shows for different host rocks, regions with potentially suitable geological formations in Germany. In this section, an overview of the three main host rocks in discussion as candidates to allocate a deep geological disposal, i.e. rock salt, clay and claystone formations and crystalline rock are provided. In general none of them match all the above mentioned criteria (Bollingerfehr, Herklotz et al. 2011) and some technical barriers must be designed to supply some lacks from the host rocks.

2.3.1 Rock salt

Rock salt formations form due to the evaporation of water from sediments of marine salts. It is one of the most studied host rocks and used to be one of the favourite candidates for a deep geological repository in Germany in the past (FZKA 2008). Other countries like USA (Macfarlane et al. 2006) are also considering rock salt as possible host rock.

An important advantage of rock salt is its high thermal conductivity and resistance allowing the denser disposal of heat producing waste and reducing the necessary space. Another positive properties are its extremely low impermeability almost preventing ingress of water to the disposal drift and the high homogeneity of the rock salt domes. The high mechanical resistance of salt rock formations allows to drill a repository directly in the host rock without supporting reinforcements (Bollingerfehr, Herklotz et al. 2011). This makes a repository easier and cheaper to built. However, the viscoplastic characteristics are certainly the most striking advantage of rock salt. Openings, fractures and pores close with time under the lithostatic pressure of the rock and overlays.

As disadvantages, rock salt is water soluble. In case of extensive water access from outside due to inappropriate sealing or brine pockets in the host rock, the container may corrode. Released radionuclides are then less efficiently retarded by sorption reactions as compared to other host rocks.

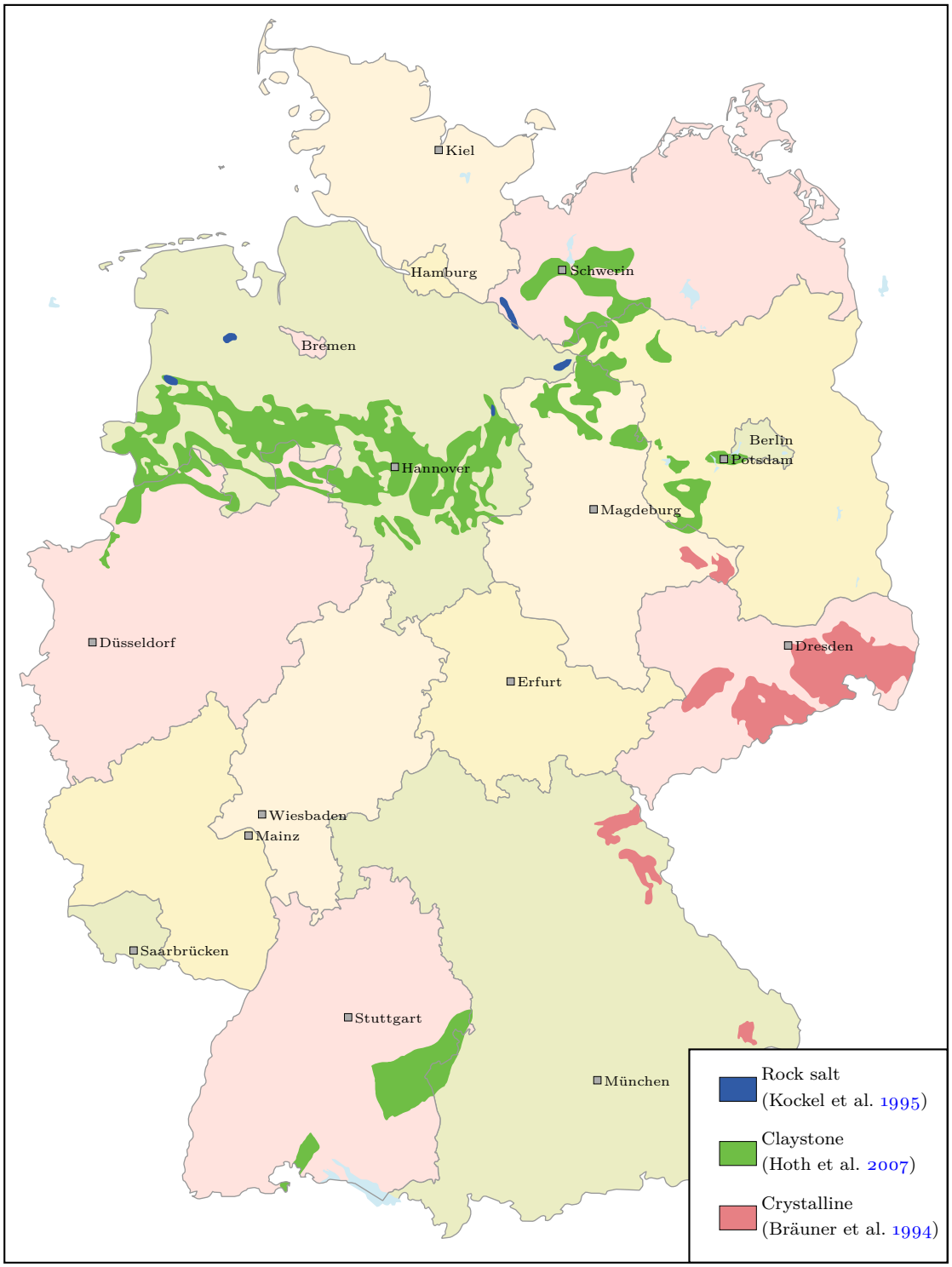

FIGURE 2.3: Distribution of the possible locations for a deep geological repository in Germany according to the different host rock configurations

2.3.2 Clay and Claystone

Clay is an unconsolidated sediment mainly consisting of particles smaller than 2 µm. It is composed of phyllosilicate minerals with traces of metal oxides and organic matter containing a variable amount of water trapped in the mineral structure. When the clay is compressed, the sediments consolidate giving room to claystone formations. Even when both host rocks have many differences, they have similar advantages and disadvantages for the drilling of a deep geological repository and therefore, can be studied together.

Claystone formations are the favourite option for countries like France (ANDRA 2001), Spain (Gens et al. 2009), and Switzerland (BFE 2008; HSK 2007). Germany is also considering claystone as potential host rock option (FZKA 2008). Clay formations as potential host rock are only considered in Belgium (Neerdaela et al. 1998).

The main advantages are a very small permeability and in contrast to salt rock a very small solubility. This makes clay and claystone formations very resistant to water penetration. On the other hand side, in contrast to a repository in rock salt, pore water access to the waste is the expected long-term evolution scenario of a repository in clay rock. Moreover, even if water ingresses into the drift, this formations still have a very hight sorption capacity retarding the diffusion of sorbing radionuclides. However, long lived fission and activation products like ^{129}I and ^{36}Cl are not retained.

However, in contrast to a repository in rock salt, drifts and access galleries of a repository in soft rock, such as clay and specially claystone, have to be reinforced with concrete lining with a thickness of several decimetres (Chen et al. 2014; Leon Vargas et al. 2017) increasing the complexity and costs of the construction. Furthermore, their heat resistance is much lower. This forces to reduce the density of disposed heat producing waste within one cask (Leon Vargas et al. 2017) and thereby, demands larger storage capacities.

2.3.3 Crystalline

Crystalline formations include different rocks from magmatic (granite, granodiorite, syenite etc.) and metamorphic origin (granulite, basalt, etc.). They are characterized by a block structure on any scale with undulation orientation of the fractures and fracture zones (Pusch et al. 2015).

Crystalline is considered by countries like Spain (Gens et al. 2009) but as secondary option. However, some countries must select crystalline as host rock, since no other domestic formations are available. This is the case of Sweden (Bollingerfehr, Herklotz et al. 2011) and Finland (Hammer et al. 2009)

The main advantages of crystalline formations are a high stability, a very low solubility and in principle a good heat resistance.

However, the main disadvantage of the crystalline formations is the hardness and brittleness of the rock. This gives rise to the formation of water conducting fractures in case of seismic movements. Usually bentonite barriers are emplaced surrounding and protecting the container against shear forces. As fracturing cannot be excluded an thus water access to the container surface must be considered, containers in the Scandinavian disposal concept are designed with a corrosion resisting copper coating. This bentonite barriers have temperature restrictions similar to the ones from clay and claystone formations (Bollingerfehr, Herklotz et al. 2011; Appel et al. 2002).

Table 2.2 compares the main properties of each host rock. As explained above, all have pros and contras. Therefore, the selection of the ideal host rock is not a simple task.

To account for possible interactions of the radiation, only the first decimetres of the drift walls have a relevant impact. Therefore, to study the radiation field and the personal dose, it is necessary to define only two types of drifts. The ones directly drilled in the host rock, i.e. rock salt drift, and the ones with a reinforcement of concrete, i.e. clay, claystone and crystalline. The first one from now on referred as Rock Salt Drift (RSD). The second one from now on referred as Concrete Lining Drift (CLD).

2.4 Shielding of nuclear waste

In a deep-geological disposal facility or above-ground storage facility of high-level nuclear waste, the SNF is contained inside a shielding cask. This cask is designed as a technical barrier to prevent the dispersion of the radioactive nuclides contained in the nuclear waste as well as to facilitate a proper protection of the workers from radiation (Bollingerfehr, Filbert, Lerch et al. 2011). To properly contain the radionuclides, a shielding cask should have a good mechanical resistance, high heat conductivity to dissipate the heat of the SNF outside the cask and resistance to corrosion since water may come in contact with the cask. To shield the radiation emissions, the cask should be constructed with materials of high density to attenuate the gamma rays emissions and moderator materials to reduce the neutron kinetic energy should also be present.

Depending on the disposal facility different concepts of shielding cask have been developed with characteristics according to the requirements of the disposal option. In Germany these are the POLLUX® concept for deep geological disposal, the CASTOR family for transport and above-ground storage and the BSK 3 concept for disposal in

TABLE 2.2: Properties of the main host rock candidates to allocate a deep geological repository.

Property	Salt rock	Clay	Claystone	Crystalline
Density (kg/m^3)	2.11 to 2.19[a]	2[b]	2.37 to 2.65[c]	2.6 to 2.8[b]
Young's modulus (GPa)	31.0[d]	0.2 to 0.4[b]	3.2 to 15.1[e]	73.8[f]
Poisson's ratio (-)	0.27[a]	0.43[b]	0.27[e]	0.22[f]
Bulk modulus (GPa)	20.70[c]	0.48 to 0.95[c]	3.9 to 8.3[c]	43.90[f]
Shear modulus (GPa)	12.40[c]	0.07 to 0.14[c]	2.2 to 4.5[c]	30.2[f]
Permeability (m^2)	1.10×10^{-21}[b]	3.06×10^{-19}[b]	3.50×10^{-22}[e]	2.04×10^{-11}[b]
Thermal conductivity (W/(m K))	5.5[a]	1.69[b]	1.54 to 1.86[e]	1.35 to 3.4[g]

[a] Bräuer et al. (2011)
[b] Brasser et al. (2008)
[c] Stahlmann et al. (2015)
[d] National Research Council (1996)
[e] Nagra (2002)
[f] Itasca Consulting Group Inc. (2009)
[g] Schön (2011)

vertical boreholes in rock salt. Other countries like France have also their concepts like the C-Overpack for horizontal disposal in claystone boreholes with retrievability option or the C-1/2 for disposal without retrievability option.

In general, these casks have a double shell design, i.e. the SNF is stored inside an inner cask to shield the radiation surrounded by a neutron moderator (e.g. polyethylene, graphite). To preserve the mechanical integrity, this body is contained in a thick cask of cast iron or analogous materials. In this context, the POLLUX® concept has been selected since it may be considered as a reference concept for a deep-geological repository in Germany.

2.4.1 The POLLUX® concept

The POLLUX® cask has a cylindrical shape and it is composed of an external cask of nodular cast iron and an internal cask of stainless steel. A set of polyethylene rods serving as neutron moderator is placed inside the external cask. The nuclear waste is then stored inside the internal cask as shown in Figure 2.4. The maximal loading capacity is the Fuel

Rods (FRs) of 10 Power Water Reactor (PWR) Fuel Assemblies (FAs) which contains 5.45 tonnes heavy metal (t HM).

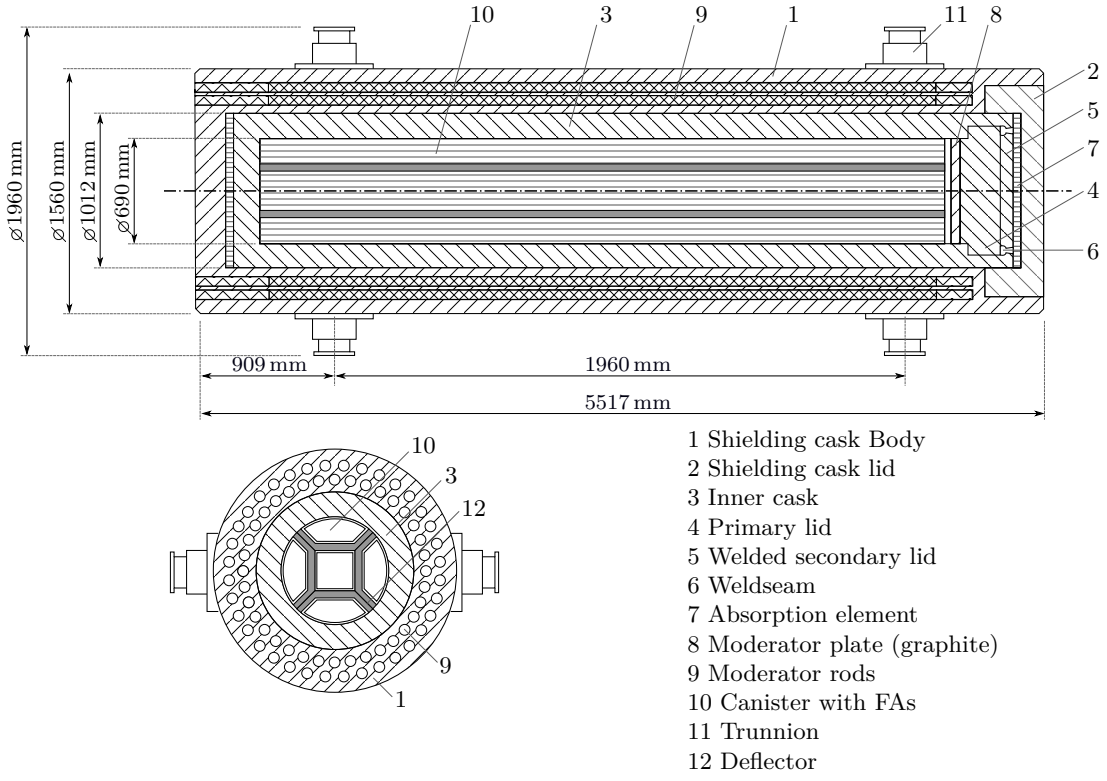

FIGURE 2.4: Horizontal (top) and vertical (right) cut of a POLLUX® cask according to (Janberg et al. 1998) and its dimensions. The finned elements are not represented.

Each FA contains 236 FRs with a diameter of 0.93 cm, an active length of 390 cm and an inactive length of 63.8 cm. A description of the geometrical parameters and the materials according to the specifications from (Janberg et al. 1998; Filbert, Tholen et al. 2011) is summarized in Table 2.3. Due to the geometrical complexity and some uncertainties in the POLLUX® dimensions, the following simplifications are assumed to model the POLLUX® cask:

- The FRs are not simulated in detail. Instead, the SNF stored inside the internal cask is assumed as a homogeneous mixture. In general, the Mixed OXide (MOX) FRs are supposed to be placed in the centre of the cask surrounded by the Uranium diOXide (UOX) FRs. This arrangement provides an additional shielding for neutrons coming from MOX FRs. Hence, a homogeneous mixture will give conservative results since the MOX SNF (see in chapter 4) is the main contributor to the neutron emissions, is homogeneously distributed and less shielded.

- Two zones are defined in a FR, i.e. an active zone containing the fuel pellets and an inactive zone which corresponds to the top and bottom of the FR mainly composed of zircaloy. The effective density in these zones is calculated according to Equation 2.1:

$$\rho_{zone} = \frac{m_{zone}}{V_{canister_{zone}}}, \tag{2.1}$$

where m_{zone} is the mass of the corresponding zone and $V_{canister_{zone}}$ is the total volume available in the POLLUX® cask for that zone.

TABLE 2.3: Material and geometrical parameters of the POLLUX®-cask

Zone	**Material**	**Density (g/cm³)**	**Layer height (cm)**	**Radius (cm)**
Fuel active zone	Spent fuel + Zircalloy[a]	-[e]	390.0	34.50
Fuel inactive zone	Zircalloy-4[b]	-[e]	453.8	34.50
Internal cask	Stein Steel MnNi[c]	7.85	508.6	50.55
Neutron moderator rods	Polyethylene	0.96	496.9	3.75
Top moderator	Graphite	2.10	10.0	34.50
Bottom moderator	Graphite	2.1	4.5	50.55
External cask	Nodular Cast Iron[d]	7.55	551.7	78.00

[a] Peiffer et al. (2011)
[b] Kearns (1967)
[c] Smailos et al. (1992)
[d] Kursten et al. (2003)
[e] Density depends of the m_{zone} according to Equation 2.1

For disposal in RSD, the maximal loading capacity of a POLLUX® cask is the FRs of 10 PWR FAs, so about 5.45 t HM. A homogeneous mixture of 90 % PWR-UOX and 10 % PWR-MOX SNF is used as a representative waste inventory according to the estimated total amount of SNF available in Germany as given by (Peiffer et al. 2011) (the POLLUX® cask with an homogeneous mixture of one MOX FA and nine UOX FAs herein after referred to as POLLUX-10). Due to temperature restrictions of nuclear waste disposal in formations with a bentonite backfill, for disposal in CLD the maximum amount of FAs per cask is set to 3, as recommended by Leon Vargas et al. (2017). Therefore, one POLLUX® cask with an homogeneous mixture of two thirds PWR-UOX and one third PWR-MOX SNF corresponding to 1 MOX FA and 2 UOX FAs and 1.64 t HM (herein after referred to as POLLUX-3M) and two POLLUX® casks with an homogeneous mixture of PWR-UOX corresponding to 3 UOX FAs and 1.64 t HM (herein after referred to as POLLUX-3U) are employed for simulating emplacement in CLD. The composition of each cask is resumed in Table 2.4.

TABLE 2.4: Percentage of MOX and UOX for each POLLUX®-cask

Cask	MOX (%)	UOX (%)	Density active zone[a] (g/cm^3)	Density active zone[a] (g/cm^3)
POLLUX-10	10	90	5.19	0.95
POLLUX-3M	33	67	1.56	0.29
POLLUX-3U	0	100	1.56	0.29

[a] Density calculated with Equation 2.1

2.5 Concept of radiological protection and dosimetry

2.5.1 Concept of radiological protection

The ionizing radiation is radiation with enough energy to remove tightly bound electrons from the orbit of an atom during an iteration with it, causing the atom to become charged or ionized. If these iterations takes place in human tissue they can potentially inflict damage on biomolecules e.g. the DNA structure, with potential consequences for health.

The biological effects of the ionizing radiation can be classified in deterministic and stochastic (see Figure 2.5). Deterministic effects only appear once a determined threshold level of exposure is exceeded and the severity of damages in human tissue increases monotonously with the absorbed dose. Examples of them are skin burn, organ atrophy or changes in the blood composition. Stochastic effects however, are assumed to follow a statistical risk for a radiation induced disease increasing linearly with increasing dose. A dose threshold in this case is not known to exist. The severity of the effects however, is not directly dose related. This model is known as Linear no-threshold model (LNT). The typical example of stochastic effect is the risk of suffering a cancer.

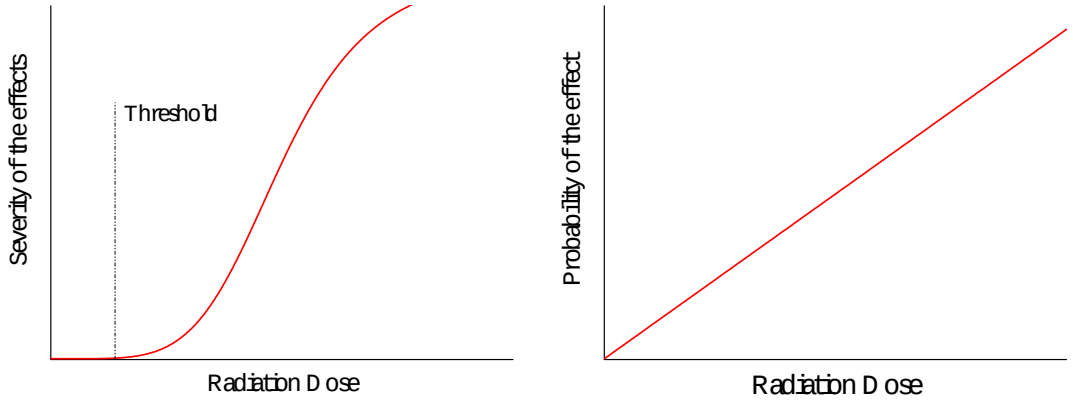

(a) Deterministic effects (b) Stochastic effects

FIGURE 2.5: Deterministic and stochastic effects of ionizing radiation

Deterministic effects can be "easily" avoided with the appropriated radiation protection mechanisms and occupational exposure dose limits since there is a particular level of exposure associated to them. Stochastic effects however, due to their statistical origin may present even by the lowest exposition a latent risk. Although the latent risk due to low radiation exposures is just an assumption, the LNT concept is a provisional radiation protection concept.

To reduce radiological risks, the ALARA concept (As Low As Reasonably Achievable) is developed. The ALARA concept considers a risk acceptable when a further reduction of it would imply disproportionated costs (economical, material, etc.) for the gained benefit. The ALARA concept is based in three principles:

- Distance: Increasing the distance to the radioactive source reduces the received dose.
- Time: The lower the exposure time the lower the received dose.
- Shielding: The creation of barriers between the source and the irradiated subject reduces the received dose.

2.5.2 Dosimetry

Dosimetry is the science that takes cares of the measurement of the absorbed dose delivered by ionizing radiation and to assess the impact of the radiation dose received by the human body. Depending on the location of the radioactive source, the dosimetry is divided in external dosimetry, if the ionizing radiation is coming from radionuclides outside the human body, and internal dosimetry if it is coming from radionuclides incorporated by the human body. The International Commission on Radiological Protection (ICRP) and the International Commission on Radiation Units and measurements (ICRU) are the international organizations in charge of the definition of the dosimetry quantities. The description of the radiological units below is extracted from (Allisy, Jennings, Kellerer and Müller 1993; Allisy, Jennings, Kellerer, Müller et al. 1998; ICRP 2007).

In a high-level nuclear waste repository the SNF is contained inside a shielding cask. Therefore, the assessment of the radiation dose under normal operation conditions, i.e. when the cask is not damaged and there is no radionuclide release, corresponds to the external dosimetry. The dose is characterized by the energy of the ionizing energy but also by the activity of the radionuclides and the radiation type. The activity A defined as the number of disintegrations in radioactive matter at a given time. It reads to:

$$A = \frac{dN}{dt}, \tag{2.2}$$

where dN is the number of disintegrations and dt the time interval. It is measured in desintegration s^{-1} which is named Becquerel (Bq).

The fluence Φ is the number of particles passing through a medium. It is given by

$$\Phi = \frac{dN}{da}, \tag{2.3}$$

where dN is the number of particles and da is the cross-sectional area of a sphere through which the particles pass. By using a sphere, the area perpendicular to the direction of each particle is accounted for, so that all particles passing through this volume of space are included. Fluence is measured in particles cm^{-2}.

The absorbed dose D defined as the energy absorbed by a certain amount of mass is given by:

$$D = \frac{d\bar{\epsilon}}{dm}, \tag{2.4}$$

where $d\bar{\epsilon}$ is the mean energy and dm is a certain mass. It is measured in $\mathrm{J\,kg}^{-1}$ which receives the name of Gray (Gy).

The absorbed dose does not take into account the biological impact of the different radiation types. Instead, the dose equivalent H is used which is defined as:

$$H = Q \cdot D, \tag{2.5}$$

where D is the absorbed dose and Q is the quality factor to weight the relative biological effectiveness of the radiation defined as a function of the linear energy transfer L_Δ. It is measured in $\mathrm{J\,kg}^{-1}$, which is named Sievert (Sv). The linear energy transfer L_Δ of a material, for charged particles, describes how much energy an ionizing particle transfers to the material traversed per unit distance. It is given by:

$$L_\Delta = \frac{dE_\Delta}{dl}, \tag{2.6}$$

where dl is the travelled distance and dE_Δ is the energy lost by a charged particle due to electronic collisions in dl minus the sum of the kinetic energies of all the electrons released with kinetic energies in excess of Δ. It is measured in $\mathrm{J\,m}^{-1}$.

Finally, the effective dose E is the sum of the equivalent doses in tissues or organs, multiplied each one by the corresponding tissue weighting factor. The tissue weighting factor is a multiplier that accounts for the different sensitivity of organs and tissues in the body to ionising radiation. The effective dose is given by:

$$E = \sum_T w_T \cdot H_T, \tag{2.7}$$

where H_T is the equivalent dose for the tissue T and w_T is the tissue weighting factor. The effective dose is also measured in Sv.

2.5.2.1 Source and far field detection

In (Allisy, Jennings, Kellerer and Müller 1993) the ICRU sphere (Figure 2.6) is defined as a sphere of 30 cm diameter made of tissue equivalent material with a density of 1 g/cm^3 and a mass composition of 76.2 % oxygen, 11.1 % carbon, 10.1 % hydrogen, and 2.6 % nitrogen used as a reference phantom in defining dose equivalent quantities.

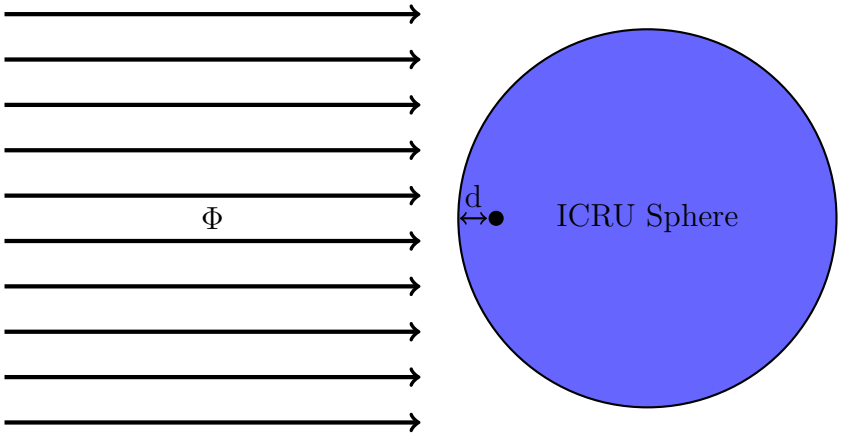

FIGURE 2.6: ICRU sphere where d is the depth where $H^*(d)$ is measured .

To calculate the dose equivalent inside the disposal drift, the ambient dose equivalent $H^*(d)$ can be employed. $H^*(d)$ is defined as the dose equivalent that would be produced by the corresponding expanded and aligned field, in the ICRU sphere at a depth d on the radius opposing the direction of the aligned field (see Figure 2.6). $H^*(d)$ is measured in Sievert.

Sometimes it is desirable to compare exposures with different durations or simply the length of the radiation exposure is unknown. In these cases the ambient dose equivalent rate $\dot{H}^*(d)$, which is defined as the amount of received $H^*(d)$ in an interval of time, can be employed. It is given by:

$$\dot{H}^*(d) = \frac{dH^*(d)}{dt}, \tag{2.8}$$

where $dH^*(d)$ is the increment of ambient dose equivalent and dt is the time interval. It is measured in J kg^{-1} s^{-1} which is named Sievert per second (Sv s^{-1}).

The operational quantities recommended by (ICRP 2007) for ambient dose equivalent are $H^*(0.07)$ for weakly penetrating radiations and $H^*(3)$ and $H^*(10)$ for strongly penetrating radiations.

2.5.2.2 Personal dose

The radiation field provides information about the dose distribution in the gallery. However, a proper assessment requires an estimate of the individual dose received by the workers. Therefore, the personal dose equivalent $H_p(d)$, which is the dose equivalent in soft tissue at an appropriate depth d below a specified point on the body, usually the position of the personal dosimeter, is applied. Like $H^*(d)$, $H_p(d)$ is also measured in Sievert.

Similar to the ambient dose equivalent, there are situations where the duration of the exposure is unknown or different exposition times are compared. The personal dose equivalent rate $\dot{H}_p(d)$, defined as the amount of received $H_p(d)$ in a interval of time is given by:

$$\dot{H}_p(d) = \frac{dH_p(d)}{dt}, \tag{2.9}$$

where $dH_p(d)$ is the increment of ambient dose equivalent and dt is the time interval. It is measured in Sievert per second.

Similar to the ambient dose equivalent, $H_p(0.07)$ (skin dose), $H_p(3)$ (eye lens dose) and $H_p(10)$ (personal deep dose) are the operational quantities for individual human dose monitoring recommended by (ICRP 2007).

Two different protection concepts are defined in (ICRP 2007), the constraints and reference levels and the dose limits. The constraints and reference levels, as illustrated in Figure 2.7a, define for a source in all exposure situations the radiological protection requirements. The dose limits concept, as indicated in Figure 2.7b, defines for one person the maximal amount of dose that should not be exceeded irrespective of its direction. This amount takes in account the dose received from all regulated sources in planned exposure situations. Table 2.5 presents the dose limits according to (ICRP 2007).

Since many countries are still using the old limit of 150 mSv for the eye lens, the 10 mm depth is used here as standard to perform ambient and personal dose calculations.

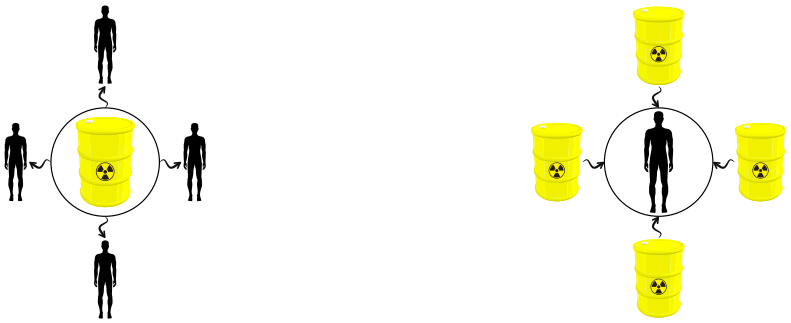

(a) Constraints and reference levels (b) Dose limits

FIGURE 2.7: Dose limits contrasted with dose constraints and reference levels for protecting workers and public

TABLE 2.5: Recommended dose limits in planned exposure situations (Partially extracted from (ICRP 2007))

Type of limit	**Occupational**	**Public**
Effective dose[a] (E)	20 mSv/yr (averaged over 5 years)[b]	1 mSv/yr[c]
Equivalent dose ($H_p(d)$) in:		
Skin[d] ($H_p(0.07)$)	500 mSv/yr	50 mSv/yr
Eye lens ($H_p(3)$)	20 mSv/yr[e] (averaged over 5 years)[b]	15 mSv/yr

[a] $H_p(10)$ should give a conservative estimation even in cases of lateral or isotropic radiation incidence (ICRP 2007)
[b] With the further provision that it should not exceed 50 mSv in one year
[c] In special circumstances a higher value could be allow in one year, provided that the average over 5 years do not exceed 1 mSv/yr
[d] Average over 1 cm^2
[e] The old limit was 150 mSv it has been reduced in (ICRP 2012) . However many countries like Germany still use the old limit (BMJV 2001).

Chapter 3

Methods to evaluate radiological dose

3.1 Approaches to assess dose rates

To assess the dose rates in radiation protection problems, the interaction of particles with matter is calculated. The transfer of electromagnetic radiation trough a medium is affected by phenomena like absorption, emission and scattering. A transport equation describes these interactions. Two methods are available to solve these problems, deterministic and Monte-Carlo methods. The deterministic methods solve the transport equation for the average particle behaviour giving complete information throughout the phase space of the problem (Booth et al. 2003).

Monte-Carlo methods obtain solutions by simulating the track of individual particles and recording then in tallies. From these, the average behaviour of the physical system is obtained, in the consider domain. These methods, in contrast with the deterministic, provide information about specific tallies requested by the user. Since Monte-Carlo methods does not use phase space boxes, there are no averaging approximations required in space, energy, and time. Therefore, it is adequate to solve complicated three-dimensional, time-dependent problems (Booth et al. 2003).

3.2 Monte-Carlo methodology

Monte-Carlo methods use algorithms to model the probability of different events to calculate problems, which can be hardly solved with classic analytic methods. Let's assume an irregular shaped object (Figure 3.1) with an area A_{shape}, which is unknown.

If the shape is framed by an square with a well known area A_{square} and a number of particles n_{total} are randomly thrown into the square, A_{shape} is given by

$$A_{shape} = A_{square} \frac{n_{shape}}{n_{total}}, \tag{3.1}$$

where n_{shape} is the number of particles that are inside the irregular shaped object.

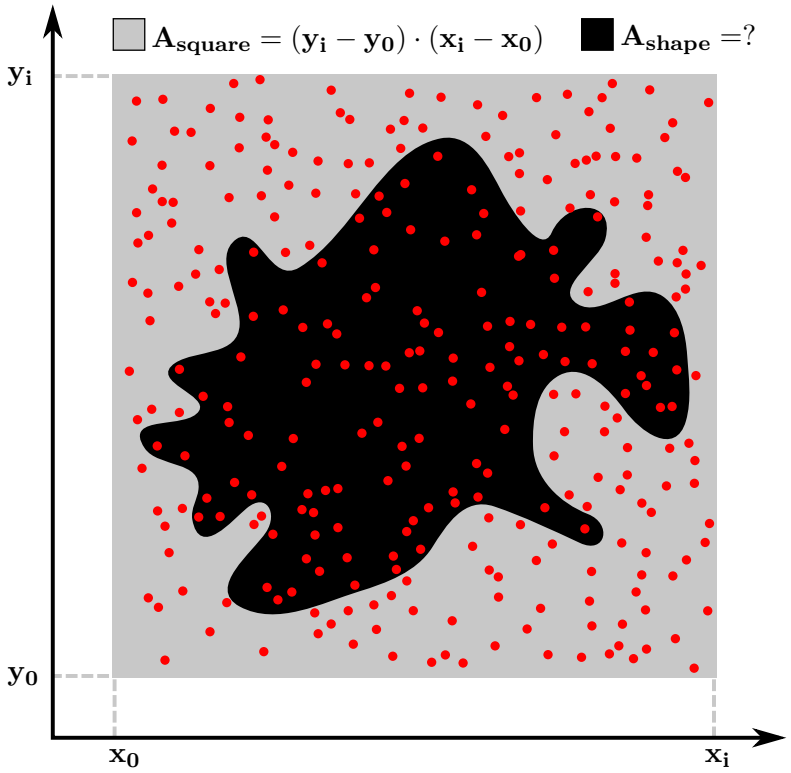

FIGURE 3.1: Example of the Monte-Carlo method to calculate an irregular area.

In general, to calculate the mathematical expectation of a stochastic variable, many statistical experiments need to be performed. If each of them gives a sample of the problem, the approximate solution of the problem is the average value of all the experiments. Many problems can be simplified with a probabilistic model. However, to obtain an adequate solution, the number of experiments must be sufficiently large.

3.2.1 Model approach and numerical means

In a transport problem particles interact with matter where the reaction type between the projectile particle and target atom follows a probabilistic distribution. Therefore, these interactions can be sampled with Monte-Carlo methods with a set of random reactions based on the distribution. Solutions can be obtained by simulating individual particles and recording their average behaviour at points of interest (tallies). To employ

Monte-Carlo simulations to solve a radiation transport problem, the following boundary conditions have to be defined:

- Geometry of the problem, including materials;
- a description of the source and
- physics of the interaction of particles

Based on these conditions, the Monte-Carlo code simulates the transport of particles emmited by the source and secondary particles through matter with a given geometry, as illustrated in Figure 3.2, until they leave the geometry of the system or are "killed" by the physics defined on the problem.

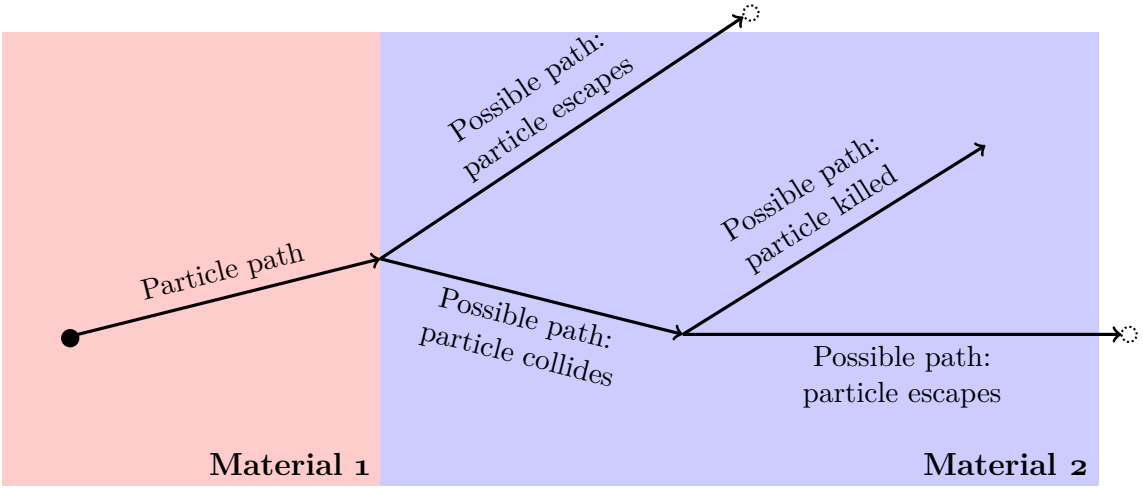

FIGURE 3.2: Sketch of potential interactions of an incident particle transport through two materials.

Since Monte-Carlo simulations are based on statistical experiments it is necessary to introduce some random perturbation in the model to generate the different solutions. This random perturbations are based on random numbers which are usually sampled from an uniform distribution in $[0, 1]$.

Monte-Carlo codes generate some statistical parameters that a simulation have to accomplish. This statistical checks give an idea of the reliability of the results. The description of the statistical parameters and the conditions that they have to achieve can be found below and are based on (Goorley et al. 2013; Shultis et al. 2010):

- **Tally Mean ($\overline{x}$):** is the average value of the values obtained in each experiment and is given by:

$$\overline{x} \equiv \frac{1}{N} \sum_{i=1}^{N} x_i, \tag{3.2}$$

where N is the total Number of Particles per Simulation (NPS) and x_i are the obtained values for each source particle. For a reliable result, the values should monotonically converge to a value, except near the beginning of the simulation.

- **Relative Error (R):** The relative error estimates the uncertainty of the tally mean and is given by:

$$R \equiv \frac{S_{\overline{x}}}{\overline{x}},$$

where $S_{\overline{x}}$ is the standard deviation of the tally mean and $\overline{x}$ is the tally mean. The value of R is determined by the scoring efficiency and the dispersion in non-zero scores. Therefore, R is defined as:

$$R^2 = R_{eff}^2 + R_{int}^2, \tag{3·3}$$

where R_{eff} measures the spread caused by scoring inefficiency (if every source particle contributes to the tally $R_{eff} = 0$) and R_{int} measures the uncertainty produced by the spread of non-zero scoring events (if all the scoring particles produce the same score $R_{int} = 0$).

To be acceptable, the value of R should be lower than 0.1 (10 %) except for point detector tallies (see next section) that should be lower than 0.05 (5 %) and should decrease monotonically with N as $1/\sqrt{N}$, except near the beginning of the simulation.

- **Figure of Merit (FOM):** It is an estimator of the efficiency of the simulation. It takes in account the simulation time and the obtained error. It is defined by:

$$FOM = \frac{1}{R^2 T}, \tag{3·4}$$

where T is the running time. Since T and R both depend of the total NPS, to be acceptable the FOM should remain relatively constant except near the start of the simulation and not exhibit oscillations.

- **Variance of the Variance (VOV):** Gives the accuracy of R and is defined as:

$$VOV = \frac{S^2(S_{\overline{x}}^2)}{S_{\overline{x}}^2} = \frac{\sum_{i=1}^{N}(x_i - \overline{x})^4}{\left[\sum_{i=1}^{N}(x_i - \overline{x})^2\right]^2} - \frac{1}{N}, \tag{3·5}$$

where $S^2(S_{\overline{x}}^2)$ is the variance of $S_{\overline{x}}^2$. Since the VOV includes third and fourth moments of the tally distribution it is more sensible to fluctuations for large history scores. To be acceptable the FOM should be lower than 0.1 and decrease monotonically as $1/N$, except near the beginning of the simulation.

Although the statistical checks provide an indication of the results reliability they cannot be directly considered as a proof of the validity of the results. Errors in the geometric configuration or rare events are not detected by the tallies. Therefore, the user has to understand the physics of the problem to avoid these errors (Goorley et al. 2013).

3.2.2 Monte-Carlo Codes

Several general purpose Monte-Carlo codes are available to calculate radiation transport problems. In this work, the Monte Carlo N-Particle (MCNP) code developed and maintained by Los Alamos National Laboratory and the MONACO module from the SCALE package developed by the Oak Ridge National Laboratory have been employed.

MCNP deals with the transport of neutrons, gamma rays, and coupled transport phenomena like the transport of secondary gamma rays resulting from neutron interactions. The MCNP code can also treat the transport of electrons, both primary source electrons and secondary electrons created in gamma-ray interactions. As described in their homepage (LANS 2010) "specific areas of application include, but are not limited to, radiation protection and dosimetry, radiation shielding, radiography, medical physics, nuclear criticality safety, detector design and analysis, nuclear oil well logging, accelerator target design, fission and fusion reactor design, decontamination and decommissioning."

MCNP has a powerful capacity to process geometries, allowing to represent complex structures. In difference with other codes, MCNP does not require programming skills since the MCNP input consists of a list of predefined commands to define the geometry, physics, source and boundary conditions. These characteristics make MCNP one of the most used programs for transport calculations. In this work, the last version of MCNP, MCNP6 (Goorley et al. 2013) which is the combination of the codes MCNP5 and MCNPX (Monte-Carlo N-Particle eXtended) has been used.

MONACO deals with transport of neutrons, gamma rays, and coupled transport, like the transport of secondary gamma rays resulting from neutron interactions. As described in the manual (Rearden et al. 2016) "Monaco was developed to address a number of long-term goals for the Monte-Carlo shielding capabilities in SCALE. The principal goals for this project included (1) unification of geometric descriptions between the SCALE shielding and criticality Monte-Carlo codes, (2) implementation of a mesh-based importance map and mesh-based biased source distribution so that automated variance reduction could be used, and (3) establishment of a code using modern programming practices from which to continue future development."

MCNP is specially designed for Monte-Carlo problems while MONACO is part of a larger software package that can perform many other nuclear problems. Although both programs can solve almost the same problems, MCNP provides in general a more intuitive input, making its use easier. Moreover, parallel computing of MCNP is more developed than in MONACO making calculations faster. Finally, MCNP presents a larger variety of tallies. These characteristics make MCNP more preferable to perform the calculations of this thesis. However, the main reason to also use MONACO is that it can be easily coupled with other modules from the SCALE package. The latest version of SCALE, SCALE 6.2 (Rearden et al. 2016) includes the SAMPLER module which, as described in section 3.3, is developed to perform uncertainty analysis.

3.2.3 Concept of tally

Tallies are provided by the user to define in Monte-Carlo code which information (fluence, energy, etc.), for which particles (neutrons, photons, electrons...), and in which position (cell, surface) should be investigated. Tallies register all the requested information and give a human-readable output. MCNP has 8 different tallies (numerate from F1 to F8) each of them with two possible units (denominated by F and *F). For the tallies employed in this work, a brief description based on (Booth et al. 2003; Shultis et al. 2010) can be found below.

- **Average Cell Flux Tally (F4):** It measures the average flux Φ of neutrons, photons, electrons or neutrons and photons in a cell normalized per source particle. If a particle of weight W and energy E travels through a certain track length T_l inside a cell of volume V it makes a contribution $W\frac{T_l}{V}$ to the flux in the cell. If $\Phi(r, E, \Omega)$ is the fluence with a given energy and angular distribution as a function of the position, the F4 tallies would measure:

$$F4 = \frac{1}{V}\int_V dV \int_E dE \int_{4\pi} d\Omega\ \Phi(r, E, \Omega), \tag{3.6}$$

$$^*F4 = \frac{1}{V}\int_V dV \int_E dE \int_{4\pi} d\Omega\ E\ \Phi(r, E, \Omega), \tag{3.7}$$

  where $F4$ is measured in $\#/(\mathrm{cm}^2\,\mathrm{source\,particle})$ and $^*F4$ in $\mathrm{MeV}/(\mathrm{cm}^2\,\mathrm{source\,particle})$.

- **Point Detector Tally (F5):** It measures the average flux of neutrons or photons in a specific point in space, normalized per source particle. This tally uses the "next event estimator" technique, which for each source particle and each collision event performs a deterministic estimate of the fluence contribution at the detector point.

The main advantage of this tally is that it requires a much lower NPS to obtain good statistical results, but it has to be used carefully or can give wrong results.

If a particle of energy E and weight W travels a distance R from the source (or collision event) to the detector its contribution to the fluence at the detector point is given by:

$$\frac{W\ p(\hat{\Omega}_p)e^{-\lambda}}{R^2}, \tag{3.8}$$

where $p(\hat{\Omega}_p)$ is the probability density function for scattering (or starting) in the direction $\hat{\Omega}_p$ towards the point detector and λ the total number of mean free paths from particle location to detector. If $\Phi(r_p, E, \hat{\Omega})$ is the energy and angular distribution of the fluence as a function of position, the F5 tallies would measure:

$$F5 = \int_E dE \int_{4\pi} d\Omega\ \Phi(r_p, \hat{\Omega}, E), \tag{3.9}$$

$$^*F5 = \int_E dE \int_{4\pi} d\Omega\ E\ \Phi(r_p, \hat{\Omega}, E), \tag{3.10}$$

with $F5$ and $^*F5$ measured in $\#/(\mathrm{cm}^2\,\mathrm{source\,particle})$ and $\mathrm{MeV/cm^2 persource/particle}$, respectively.

The main limitation of the F5 tally is that it has to be located in a uniform medium where particles do not suffer to much interactions. Therefore, it is mainly recommended for calculations in vacuum and air (Goorley et al. 2013).

- **Energy Deposition Tally (F6):** It measures the deposited energy of neutrons, photons or neutrons and photons in a cell normalized per source particle. If a particle of weight W and energy E travels a certain track length T_l inside a cell of atom density ρ_a and mass m its contribution to the energy deposition in the cell is given by:

$$W\ T_l\ \theta_f(E)\ H(E)\ \frac{\rho_a}{m}, \tag{3.11}$$

where $\theta_f(E)$ is the total microscopic cross section of the cell and $H(E)$ the heating number. Both quantities are energy dependent. If $\Phi(r, E, \Omega)$ is the energy and angular distribution of the fluence as a function of position, the F6 tallies would measure:

$$F6 = \frac{\rho_a}{m} \int_V dV \int_E dE \int_{4\pi} d\Omega\ \theta_f(E)\ H(E)\ \Phi(r, E, \Omega), \tag{3.12}$$

$$^*F6 = 1.602\,19 \times 10^{-22}\ \frac{\rho_a}{m} \int_V dV \int_E dE \int_{4\pi} d\Omega\ \theta_f(E)\ H(E)\ \Phi(r, E, \Omega), \tag{3.13}$$

where $F6$ and $^*F6$ are measured in $\mathrm{MeV/(g\,source\,particle)}$ and $\mathrm{jerk/(g\,source\,particle)}$, respectively.

MONACO has tallies that are equivalent to F4 and F5. These are named point detector tally and region tally, see (Rearden et al. 2016). Since their physics and units are the same as the described for the MCNP tallies, no further explanation is required.

3.2.4 Variance reduction techniques

For deep penetration problems or problems with very large geometries analogue simulations require a large amount of NPS to obtain acceptable results, since many of them are not able to reach the tally detectors increasing the value of R_{eff} in Equation 3.3. This holds even if paralleling computing can divide this work in many processors and therefore, reduce considerably the calculation time. In this case the so called "variance reduction techniques" (Goorley et al. 2013) are employed. These techniques modify the simulation process making certain events more or less probable than occurring physically (non-analogue simulations). Variance reduction techniques reduce the error of the simulations by increasing the scoring efficiency and hence reducing R_{eff} and decreasing the spread in non-zero scores making R_{imp} to decrease (see Equation 3.3).

Lets assume a volumetric source producing photons and a 26 cm shielding of stainless steel divided in 13 slides of 2 cm as shown in Figure 3.3. If an analogue simulation is performed almost no photon arrives to the tally detector (slide 14) as listed in Table 3.1. A possible approach to solve the problem is to increase the NPS until enough particles arrive to the detector to obtain reliable results. The disadvantage of this method is that for deep shielding, the necessary NPS could be unmanageable large for the computer. Hence, the simulation would take so long time that it would be impractical.

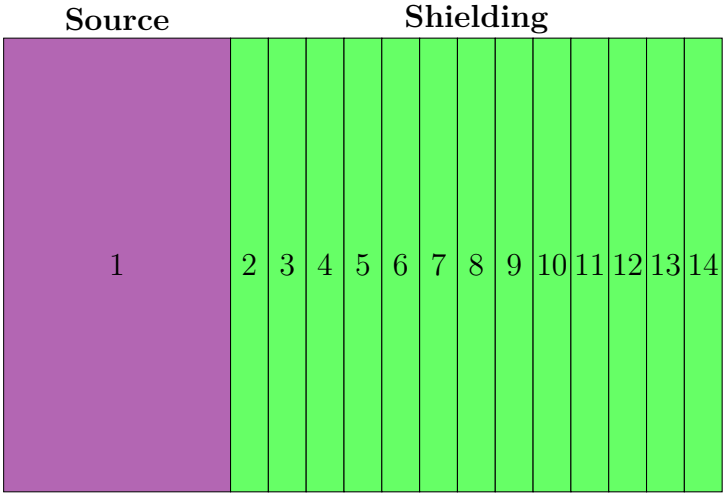

FIGURE 3.3: Source and shielding slides to keep a constant population with the "Geometry Splitting" method

TABLE 3.1: Photons in each cell for a 1×10^5 particle simulation

Slides according to Figure 3.3	**Analogue simulation $\mathbf{Imp_n = 1}$**	**Geometry splitting $\mathbf{Imp_n = 2 \cdot Imp_{n-1}}$**
1	182 189	182 757
2	5685	11 852
3	3172	13 294
4	1648	13 896
5	858	14 508
6	458	14 940
7	224	14 874
8	115	14 583
9	55	14 236
10	30	14 158
11	15	13 824
12	9	13 242
13	5	13 360
14	0	13 422

Many variance reduction techniques like "geometry splitting", "weight windows" or "virtual source generation" (Goorley et al. 2013) are provided by MCNP6 to solve this problem in a non-analogous way. One of the simplest ones to apply is the geometry splitting. Using geometry splitting, a weighting is assigned in the following way: regions near the tallies are correlated with a greater importance than regions farther away. When a particle leaves a region it is split/killed according to the importances ratio adjusting the weight of the remaining particles to leave the tally unbiased. Table 3.1 shows for the described shielding problem the NPS applying geometry splitting in each slide. In this example, the importance of the surviving particles is duplicated in each slide keeping the population approximately constant. Although very easy to apply, the main disadvantage of this method is that the geometry has to be rewritten several times until the proper configuration is reached.

The weight window method is similar to the geometry splitting but instead of dividing the geometry, a mesh is superimposed to represent the slides. The advantage of this feature is that the geometry does not need to be changed to adjust the importance since it is done automatically by MCNP6. However, this technique reveals two disadvantages. The first one is that this method cannot be applied in just one simulation. Instead, a sequence of simulations modifying parameters like density of the materials is required to allow some particles to reach the detector in order to estimate the required importance for the final simulation. The second disadvantage is that the user has no control of the importance variation leaving this decision to the program.

Another different approach is to use a virtual source. With this variance reduction technique only the interactions in a delimited geometry are calculated in the first simulation (for example inside the shielding cask) and the information of all particles which cross the outer surface are saved to a file. This file can be used as a virtual surface source in other simulations, while translations can be applied to other canisters of the same type and same source. However, this method has also some disadvantages. First, it cannot be applied if the geometry is strongly modified. For example, the cask cannot be simulated in void and later inside a disposal drift. Second, the virtual source needs to save a large amount of particles information to have reliable results in the following simulations. This is intrinsically associated to a very large calculation time and data file.

Since in this work three different cask configurations are studied (POLLUX-10, POLLUX-3M, and POLLUX-3U) and for each one neutron, gamma and beta sources are required (see chapter 4) the virtual source technique and the weigh windows technique does not save considerable time since 9 different sources have to be calculated. Moreover, the simulations performed in this work do not take place always in the same drift and simulations in vacuum are also performed. Although, the materials of the studied drifts are not always present (cask simulated free in air) they have always the same geometry. For the geometry splitting this is an advantage since the same splitting can be employed for all of them. Therefore, this technique has been chosen to perform the required non-analogue simulations.

3.3 Uncertainties and sensitivity analysis methodology

According to (Helton et al. 2002) uncertainties can be divided in two categories depending on their origin. Some uncertainties arise from the random nature of the system behaviour and cannot be reduced. These are the aleatory or stochastic uncertainties. However, a second source of uncertainties is the lack of knowledge of a certain parameter. These uncertainties are called subjective or epistemic and can be reduced if new knowledge is provided. Depending on the origin of these uncertainties and how important they are for the studied process, they can have a higher or a lower impact in the obtained results. This is called sensitivity.

For Monte-Carlo radiation transport problems the main sources of epistemic uncertainties are:

- Uncertainties due to simplifications of the simulated geometry and material composition model. For example, elimination of some elements present in the reality,

assumption of hypothesis or homogenization of some terms like density or temperature (up to now referred as "physical uncertainties").

- Uncertainties due to the nuclear cross sections. Monte-Carlo codes base their calculation on nuclear data libraries like the Evaluation Nuclear Data File (ENDF) (Chadwick et al. 2011), the Joint Evaluated Fission and Fusion (JEFF) (Kellett et al. 2009) or the Japanese Evaluated nuclear data library (JENDL) (Nakagawa et al. 1995). Therefore uncertainties on them can affect the results. (this uncertainties will be up to now refereed as "numerical uncertainties").

An uncertainty and sensitivity analysis can be divided in two parts. First, it is necessary to determine which variables may have uncertainties. Second, an evaluation of the effect that variations in these variables have on the results is required. According to the origin of the uncertainties, i.e. numerical or physical uncertainties, different approaches are possible.

To study the sensitivity of the physical uncertainties, the results obtained with the code have to be compared against experimental data. This allows to determine if the assumed simplifications have an important impact on the results. To study the sensitivity of the numerical uncertainties, an analysis including systematic variations of the cross section libraries are performed to evaluate their effect on the solution.

3.3.1 Uncertainty analysis codes

To study the physical uncertainties no especial code is required since their source is the simplifications and assumptions performed by the user when modelling the reality. Therefore, to study these uncertainties MCNP6 is used.

Although MCNP6 can be used to study the numerical uncertainties, the cross section libraries have to be perturbed manually, which is extremely time consuming and a high risk of errors. For this purpose, many codes are available to perform these perturbations and the corresponding analysis automatically.Here, the SAMPLER module from the SCALE package is taken. As described in the manual (Rearden et al. 2016) "Sampler is a “super-sequence” that performs general uncertainty analysis for SCALE sequences by statistically sampling the input data and analysing the output distributions for specified responses."

The main advantage of SAMPLER in comparison to other similar codes is that it can be easily combined with the Monte-Carlo module MONACO. SAMPLER performs random perturbations for nuclear cross sections and depletion data, which are pre-computed

by sampling covariance information and are stored in libraries read by the MONACO module to perform the Monte-Carlo calculations.

3.3.2 Definition of cross section data perturbations for transport calculations

Although the nuclear data libraries are continuously improved as new experimental data are available, the uncertainties of the measurements and the theoretical parameters still limit their precision. Therefore, it is of interest to analyze if variations of these libraries impact the solution of the transport problem.

The nuclear data files for MONACO are obtained from the AMPX library (Wiarda et al. 2016) based on the ENDF library and is distributed together with SCALE. According to the SCALE manual (Rearden et al. 2016), to generate perturbations in the cross section libraries SAMPLER assumes that the probability density functions are multivariant normal distributions with covariances given in the SCALE nuclear data covariance library. Multiplicative perturbation factors for fission product yields are generated by sampling the covariances for the independent yield uncertainties of the ENDF library. A random multiplicative perturbation factor for a cross section can be defined as

$$Q_{x,g} = 1 + \frac{\Delta\sigma_{x,g}}{\sigma_{x,g}} \tag{3.14}$$

where $\sigma_{x,g}$ is the cross section for the nuclide/reaction x and the energy group g. SAMPLER contains a master sample file with perturbation factors for 1000 samples. Each sample contains perturbation factors for all groups and reactions in all materials. The advantage of this master file is that is not necessary to perform the data sampling during the execution of SAMPLER, making calculations faster.

For each simulated case, SAMPLER selects random multiplicative perturbation factors to redefine the cross sections. Therefore, the cross sections for simulation i are defined as:

$$\sigma^i_{x,g} = Q^i_{x,g} \cdot \sigma_{x,g}. \tag{3.15}$$

Currently SAMPLER has two important limitations. First, perturbations are limited only to multi group cross section libraries and SAMPLER is not able to perform calculations with continuous energy cross section libraries. The second limitation is that the user has no control to determine which isotopes and libraries are going to be perturbed.

3.4 Application to external dosimetry

3.4.1 Monte-Carlo approach

Monte-Carlo codes are a powerful tool to perform calculations in external dosimetry. As concluded in (Behrens 2010), Monte-Carlo methods provide a more realistic approximation to the ICRP recommendations than the analytic methods. Monte-Carlo methods can include in the calculations all the relevant parameters for the results, i.e it handles the non-linear functions of the input quantities and can define better the physics and geometries of the problem. Some of the applications of Monte-Carlo codes to external dosimetry include:

- Dose distribution calculations: Monte-Carlo codes allow calculating dose at different positions or even the use of a mesh-based tally to obtain an evolution of the dose.
- Personal dose estimation: The procedures employed to estimate personal dose of occupational exposure are generally based on averaged measurement data. Moreover, doses received by the workers are recorded during working activities and afterwards, an assessment of the radiological risk can be performed. Monte-Carlo codes allow estimating the dose received before the working activities are performed.
- Dosimeter simulations: Response characteristics of the dosimeters can be simulated with Monte-Carlo codes to determine if they are appropriate for a certain radiation field. It allows also developing and testing new dosimeters without constructing them.

The study of the dose distribution and the personal dose estimation by means of MCNP6 utilization are subject of chapter 7.

3.4.2 Sensitivity and uncertainty analysis approach

When performing calculations to assess external dosimetry, many uncertainties are present. A proper quantification of them is necessary to provide an interval of confidence in the simulations. To consider the results of the dose assessment in this work as reliable the following questions have to be answered

1. Can the code properly represent the neutron-gamma mixed radiation field even after been shielded?

2. Do simplifications still provide a representative model?

3. Have perturbations on the cross sections an important impact on the calculated results?

The first and second questions are addressed in chapter 5 and are part of the laboratory approach (section 1.2) while the third aspect is discussed in chapter 6 and corresponds to the numerical approach.

Chapter 4

The high-level nuclear waste inventory in a POLLUX® cask

4.1 Introduction

In this chapter, the radionuclide source term to represent the SNF for the simulations with MCNP6 and SCALE are defined. The inventory provided in (Peiffer et al. 2011) is composed of hundreds of different isotopes, but many of them exhibit quite small activities. Therefore, only those isotopes, which contribute significantly to the total activity of the spent fuel, are considered in the source term definitions. Unloaded SNF will usually remain several years in a spent fuel pool before being stored in an interim storage. Even in the most optimistic scenario, the SNF will stay at least 40 years in the fuel pools before it can be disposed in the final disposal repository and some years will be required to prepare and transport it to its final location. Therefore, the SNF is considered to be 50 years old counting from the unloading from the reactor core and with an average burn-up of 55 GW d/(t HM). This duration corresponds to an assumed interim storage time before disposal of SNF in a deep geological disposal facility, which is planned according to BMUB (2015) from 2050 on.

Three different particle sources are calculated for each cask, i.e. neutron source, gamma source and beta source. Photons are strongly attenuated by the POLLUX® materials and inventory, but they reveal the highest activity. Therefore, they may represent a strong contribution to the total radiation dose. Neutrons generally show a lower attenuation, moreover their interaction with materials, like the iron of the shielding cask or the environment, can produce neutron-induced photons which also contribute to the total dose. Beta particles can hardly reach the outside of the POLLUX®, as they range of influence is only a few mm in solid matter. But bremsstrahlung-photons

produced by their interactions with the POLLUX® materials and environment increase the total radiation contribution.

The inventory from Peiffer et al. (2011) provides data for all the isotopes in the MOX and UOX FAs, the gamma and beta activity in Bq/(t HM) and the mass in g/(t HM) for different time intervals after the unloading from the reactor. However, no information about neutron activity is provided. Hence, to calculate the activity and other parameters like heat rate, the on-line program Nucleonica (Nucleonica 2014) is taken. For each cask (as described in section 2.4), the corresponding mixture of MOX and UOX, i.e. 10 % and 90 % for POLLUX-10, 33 % and 77 % for POLLUX-3M and 0 % and 100 % for POLLUX-3U, is assumed in form of isotopical mass in Nucleonica. Appendix B includes a list of the nuclides being considered to describe the material composition of each cask in MCNP6 and SCALE. Although many of these nuclide have none or negligible activities and do not affect to the source term characterization, their abundance is high enough to have an influence on the behaviour of the emitted particles moving through the SNF.

4.2 Neutron source

Table 4.1 shows the main contributors to the neutron emission according to Nucleonica. Since Nucleonica does not provide neutron spectra, the code SOURCES-4C (Wilson et al. 2002) is complementary used. SOURCES-4C is a code system that determines neutron production rates and spectra from (α,n) reactions, Spontaneous Fission (SF), and delayed neutron emission due to radionuclide decay. The (α,n) spectra are calculated using an isotropic angular distribution with a library of 107 nuclide decay α-particle spectra, 24 sets of measured and evaluated (α,n) cross sections and product nuclide level branching fractions, and functional α-particle stopping cross sections for effective atomic numbers $Z < 106$. The delayed neutron spectra are taken from an evaluated library of 105 precursors. Figure 4.1 shows the data flow of SOURCES-4C.

The user introduces in tape1 the atom fraction (at%) of the elemental constituents present in the material (to simplify only oxygen and uranium are considered since they represent more than 95 % of the total at%), the atom density (atoms/cm^3) of the source nuclide to be evaluated (see nuclides column from Table 4.1), the at% of the target nuclide (^{17}O and ^{18}O) and the neutron energy groups for the plotting spectra. The tapes2 to 5 provide the cross section libraries and the necessary data to perform the calculations. out, out2 and tapes6 to 9 provide the results of the calculations. Tape7 provides the output spectra, the activity (in n/(s cm^3)) and the contribution of each nuclide to the total activity.

TABLE 4.1: Main contributors to neutron emission for each cask according to Nucleonica

Nuclide	POLLUX-10 (n/s)	POLLUX-3M (n/s)	POLLUX-3U (n/s)
^{238}Pu	5.71×10^6	2.80×10^6	1.26×10^6
^{240}Pu	2.62×10^7	1.47×10^7	5.00×10^6
^{242}Pu	1.52×10^7	8.65×10^6	2.87×10^6
^{244}Cm	2.00×10^9	1.31×10^9	3.05×10^8
^{246}Cm	9.07×10^7	6.17×10^7	1.29×10^7
Sum	2.14×10^9	1.40×10^9	3.27×10^8
% total neutron emission	99.94 %	99.92 %	99.95 %

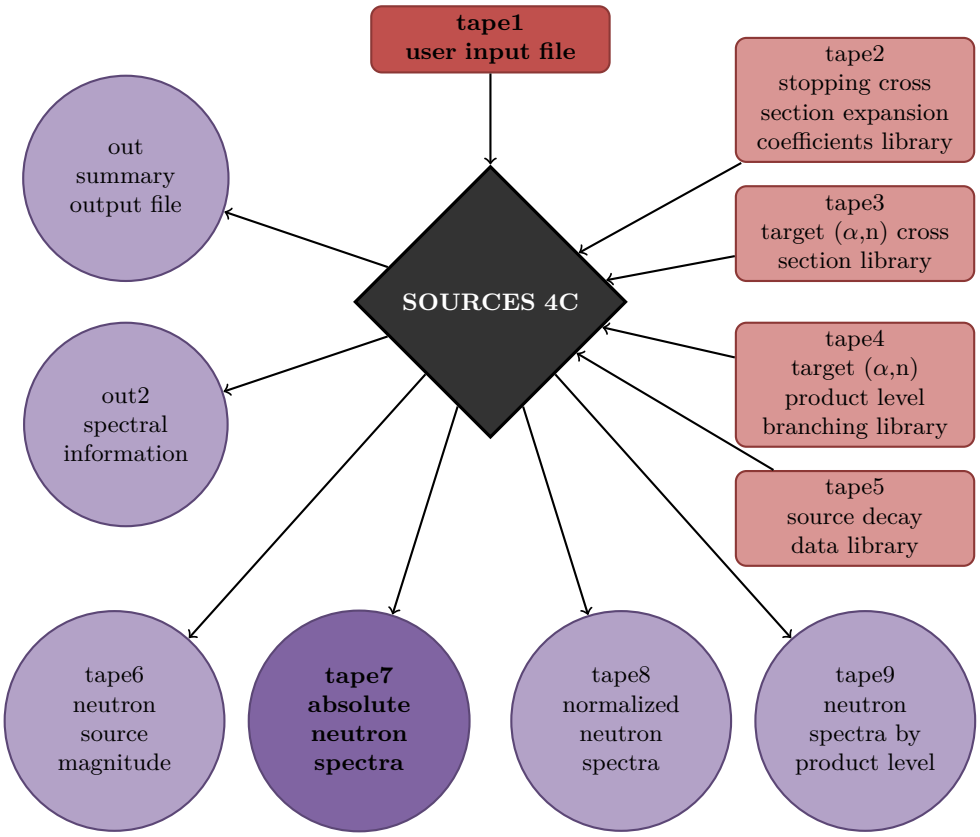

FIGURE 4.1: Schematic diagram of the data in-/output flow of the SOURCES-4C program.

Figure 4.2 shows the neutron emission probability of the SNF as a function of the neutron energy for each cask inventory (a tabular description can be found in Appendix B). Although all three cask compositions exhibit similar spectra, the contribution to the neutron emissions is different for each cask. For the considered fuel inventory, Table 4.2 shows the contribution of each nuclide to the total neutron activity. For POLLUX-10 the main contributor to neutron emissions is the SF of ^{244}Cm (93 % of the total emission) and ^{246}Cm (5 % of the total emission), while the contribution due

to (α,n) reactions is negligible. For POLLUX-3M, the contribution from ^{244}Cm and ^{246}Cm SF is 92 % and 5 %, respectively, while the contribution due to (α,n) reactions mainly stemming from interactions with ^{18}O, is 2 %. For POLLUX-3U, due to the absence of MOX the contribution from ^{244}Cm and ^{246}Cm SF decreases to 90 % and 4 %, respectively, while the contribution due to ^{18}O (α,n) reactions increases to almost 3 %.

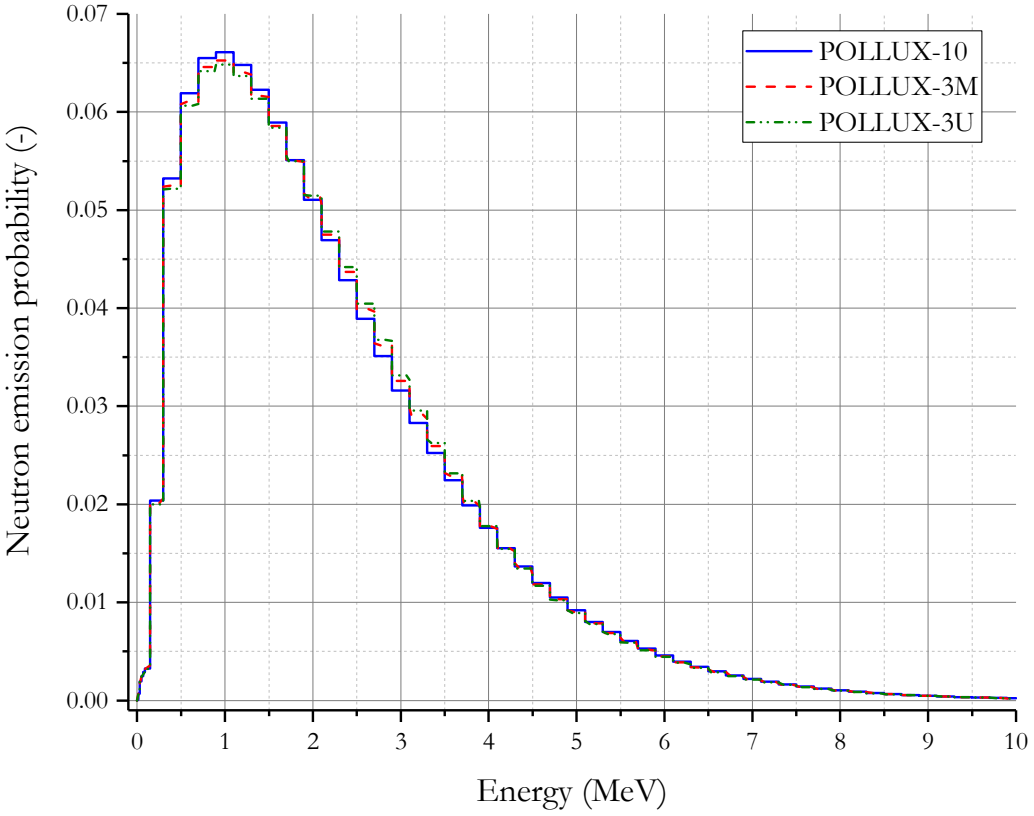

FIGURE 4.2: Neutron energy normalized distribution of SNF used as radiation source for simulations with the different casks

SOURCES-4C calculates the activity in n/(s cm^3). Hence, to obtain the real activity in n/s it must be multiplied by the volume of SNF in the cask. According to the characteristics of FAs described in section 2.4 the volume of SNF for POLLUX-10, POLLUX-3M, and POLLUX-3U is 6.25×10^5 cm^3, 1.88×10^5 cm^3 and 1.88×10^5 cm^3, respectively. Therefore, the total neutron source strength for the POLLUX-10 inventory is 2.13×10^9 n/s, while those for the POLLUX-3M and POLLUX-3U are 1.42×10^9 n/s and 3.34×10^8 n/s, respectively.

4.3 Gamma source

From the isotopical composition Nucleonica calculates the gamma activity for each nuclide. However, sorting the nuclides according to their activity is not the proper way

TABLE 4.2: Main contributors to neutron emission for each cask according SOURCES-4C

Isotope	**POLLUX-10** $(\mathbf{n/(s\,cm^3)})$		**POLLUX-3M** $(\mathbf{n/(s\,cm^3)})$		**POLLUX-3U** $(\mathbf{n/(s\,cm^3)})$	
Spontaneous Fission						
^{238}**Pu**	9.11×10^{0}	(0.300 %)	1.49×10^{1}	(0.200 %)	6.69×10^{0}	(0.400 %)
^{240}**Pu**	4.24×10^{1}	(1.30 %)	7.94×10^{1}	(1.10 %)	2.71×10^{1}	(1.50 %)
^{241}**Pu**	2.44×10^{1}	(0.700 %)	4.63×10^{1}	(0.600 %)	1.54×10^{1}	(0.900 %)
^{244}**Cm**	3.17×10^{3}	(93.2 %)	6.91×10^{3}	(91.5 %)	1.61×10^{3}	(90.2 %)
^{246}**Cm**	1.57×10^{2}	(4.60 %)	3.57×10^{2}	(4.70 %)	7.48×10^{1}	(4.20 %)
(α,n) reactions						
^{17}**O**	6.45×10^{-2}	(0.200 %)	1.18×10^{1}	(0.200 %)	4.24×10^{0}	(0.200 %)
^{18}**O**	7.55×10^{-1}	(0.0100 %)	1.38×10^{2}	(1.80 %)	4.95×10^{1}	(2.80 %)
Total	3.40×10^{3}		7.55×10^{3}		1.78×10^{3}	

to evaluate their contribution to the gamma emission since some of them have a high activity but their gamma energies are too low. Instead the decay heat can be employed since it implies also the energy of the emitted gamma rays. Table 4.3 shows for each SNF composition, the resulting gamma decay heat and the corresponding activity for the main contributors. Also included in the table is their decay heat sum together with the percentage they represent from total gamma heat generation. For the three compositions, ^{137m}Ba represents the main contribution to the gamma decay heat release, while ^{154}Eu and ^{241}Am contribute less than 1 %. Other nuclides exhibit negligible heat production.

TABLE 4.3: Main contributors for each cask to gamma decay heat rate (in W) and their gamma activity (in Bq) according to Nucleonica

Nuclide	**POLLUX-10**		**POLLUX-3M**		**POLLUX-3U**	
	(W)	**(Bq)**	**(W)**	**(Bq)**	**(W)**	**(Bq)**
^{137m}**Ba**	1.0×10^{3}	1.0×10^{16}	3.0×10^{2}	3.2×10^{15}	3.0×10^{2}	3.1×10^{15}
^{154}**Eu**	8.8×10^{0}	4.4×10^{13}	4.2×10^{0}	9.5×10^{14}	2.4×10^{0}	1.2×10^{13}
^{241}**Am**	7.7×10^{0}	1.8×10^{15}	3.2×10^{0}	1.6×10^{13}	1.5×10^{0}	3.5×10^{14}
Sum	1.02×10^{3}		3.1×10^{2}		3.1×10^{2}	
% total	99.85 %		99.74 %		99.88 %	

MCNP6 and SCALE require the gamma source as a discrete distribution with one probability for each energy emission. Nuclear libraries like ENDF, JEFF or JENDL provide for each nuclide the gamma emission probability. To adjust the probabilities P_i to the activity of each nuclide for the MCNP6 and SCALE inputs Equation 4.1 is used:

$$P_i^{SNF}(E_i) = \frac{P_i(E_i) \cdot A_{isotope}}{\sum_{isotope=1}^{n} \left(\sum_{i=1}^{n} P_i(E_i) \cdot A_{isotope} \right)}, \tag{4.1}$$

where $P_i(E_i)$ is the probability for each gamma emission energy of each isotope extracted from the ENDF libraries and $A_{isotope}$ is the activity of each isotope (see Table 4.3).

Figure 4.3 shows the probability of each gamma energy of ^{241}Am, 154Eu and 137mBa for each cask (a tabular description can be found in Appendix B). For all the configurations, the main contribution to the gamma emission from the decay of ^{137m}Ba (65 % for POLLUX-3M , 90 % for POLLUX-10 and 95 % for POLLUX-3U). The remaining fraction of the gamma emission depends strongly of the cask configuration.

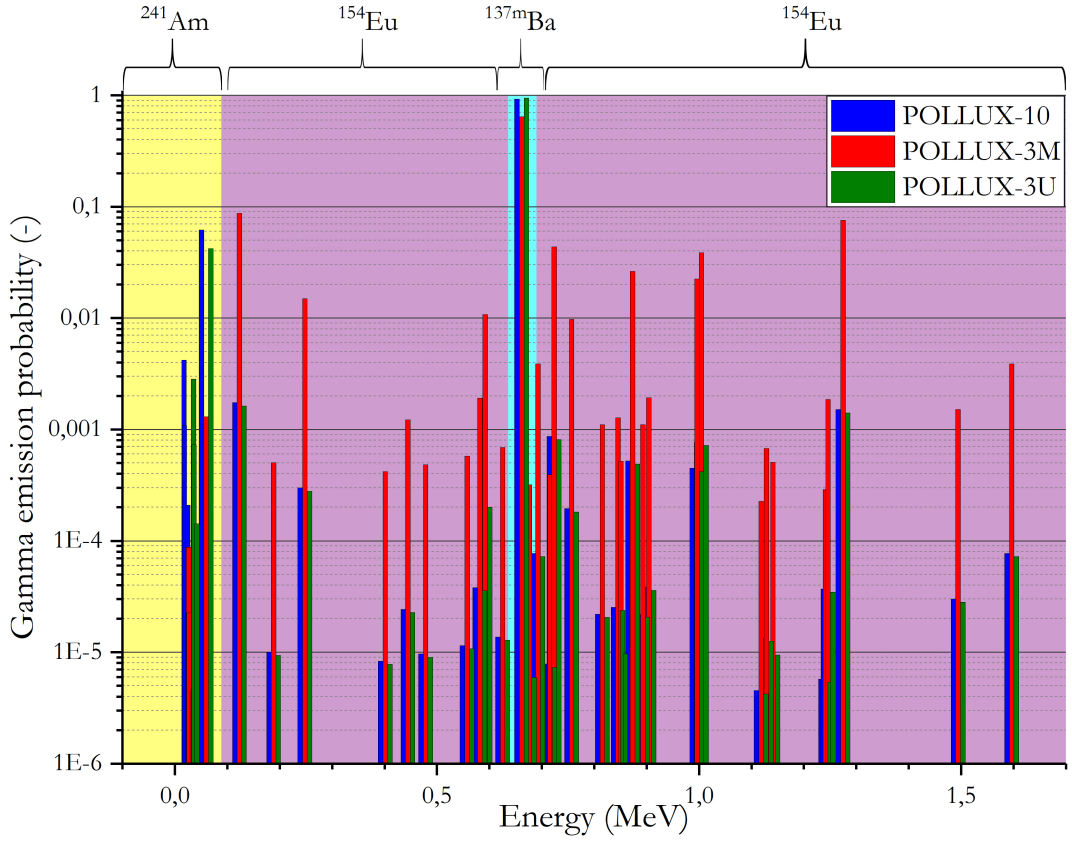

FIGURE 4.3: Normalized gamma emission as a function of the emission energy for ^{241}Am, 154Eu and 137mBa for the different casks.

4.4 Beta source

Beta particles can hardly reach the outside of a POLLUX® cask, but bremsstrahlung-photons produced by their interactions with the cask structure material and inventory can produce γ-radiation. As for the gamma source, the decay heat released is used as criterion to select the main contributors to the beta emissions. Table 4.4 shows the most relevant β emitting isotopes together with their activity for the three cask configurations. Since each nuclide has its specific beta spectrum, Eckerman et al. (1994) and Burrows (1988) provide energy emission vs. probability distribution tables that can be directly used as input. Figure 4.4 shows the beta spectra of ^{90}Y, ^{137}Cs and ^{90}Sr. To account the SNF in each cask, the spectra are multiplied by their corresponding activity, which is shown in Table 4.4.

TABLE 4.4: Main contributors for each cask to beta decay heat rate (in W) and their beta activity (in Bq) according to Nucleonica

Nuclide	**POLLUX-10**		**POLLUX-3M**		**POLLUX-3U**	
	(W)	**(Bq)**	**(W)**	**(Bq)**	**(W)**	**(Bq)**
^{90}Y	1.0×10^{3}	6.7×10^{15}	2.7×10^{2}	1.8×10^{15}	3.2×10^{2}	2.1×10^{15}
^{137}Cs	3.3×10^{2}	1.1×10^{16}	1.0×10^{2}	3.3×10^{15}	1.0×10^{2}	3.3×10^{15}
^{90}Sr	1.8×10^{2}	6.6×10^{15}	4.8×10^{1}	1.7×10^{15}	5.8×10^{1}	2.1×10^{15}
Sum	1.5×10^{3}		4.1×10^{2}		4.8×10^{2}	
% total	92.34 %		90.45 %		92.83 %	

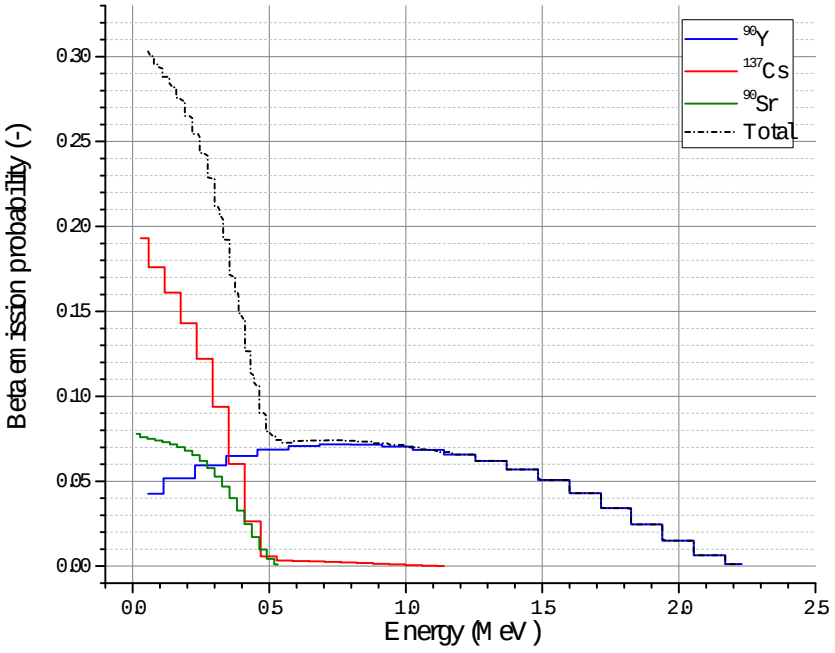

FIGURE 4.4: Beta emission probability SNF used as radiation source for the simulations with different casks

Chapter 5

Approach for dose calculations using a neutron generator

5.1 Goals

This chapter deals with the TUD-NG and the corresponding MCNP6 simulations. As described in section 3.3, to perform a proper Monte-Carlo evaluation of the dose rate and personal dose around a SNF shielding cask, it is necessary to contrast the numerical results with experimental data to determine their reliability, i.e. if the code is able to reproduce the results and if the simplifications of the model affect to these results. However, since detailed information about the SNF content of such casks is confidential, measurements of the radiation fields around a shielding cask with SNF cannot be compared to their respective simulations. Instead, to assess the modelling and simulation approaches, experiments with a set-up consisting of materials and radiation similar to a shielding cask are performed.

Therefore, a neutron source able to produce neutrons in an energy range close to the SNF is used. In this context, a neutron generator is chosen since it is able to emit neutrons in a well-defined energy range. Therefore, the TUD-NG, located at the Helmholtz Zentrum Dresden Rossendorf (HZDR) is employed. There, 2.5 MeV neutrons are produced to represent the average neutron energy stemming from SNF and a detector measures the neutron and gamma radiation.

Since simulations are an approximation of the performed experiments, some differences are expected between measurements and simulations. Moreover, the simulation of a neutron generator source is not trivial, since it has an angular dependence that cannot be directly calculated by MCNP6. Instead an approximation must be employed. Hence,

the main objective of this chapter is to establish a laboratory approach that aims at demonstrating the reliability of calculations and their uncertainty, which are then used in the subsequent chapters as verified and validated simulation route.

5.2 Experimental set-up

5.2.1 Description of the TUD-NG facilities and the conducted experiments

Here, the neutron generator located at the facilities of the HZDRis employed. It is a Cockroft-Walton type deuterium accelerator with a terminal deuteron energy of 320 keV and a peak current of 10 mA. The generator is able to operate in two modes, continuous and pulsed. A detailed description can be found in (Klix et al. 2011). If a tritium-titanium target is used it generates neutrons with energies of up to 14.1 MeV (Equation 5.1 Kikuchi et al. 2012). However, if a deuteron-titanium target is employed neutrons with energies of 2.45 MeV (Equation 5.2 Kikuchi et al. 2012) and protons with energies of 3.02 MeV (Equation 5.3 Kikuchi et al. 2012) are produced.

$$ {}^{2}_{1}H + {}^{3}_{1}H \longrightarrow {}^{4}_{2}He\ (3.5MeV) + {}^{1}_{0}n\ (14.1MeV), \tag{5.1} $$

$$ {}^{2}_{1}H + {}^{2}_{1}H \longrightarrow {}^{3}_{2}He\ (0.82MeV) + {}^{1}_{0}n\ (2.45MeV), \tag{5.2} $$

$$ {}^{2}_{1}H + {}^{2}_{1}H \longrightarrow {}^{3}_{1}H\ (1.01MeV) + {}^{1}_{1}H\ (3.02MeV). \tag{5.3} $$

A source able to produce neutrons close to the ones emitted by the SNF inside a POLLUX® cask (see Figure 4.2) is desired, which requires the use of a deuteron target.

The target of the neutron generator is located in the centre of a shielding room, on a platform equipped with open mesh flooring to minimize the possible backscattering radiation. Furthermore, since background radiation can also be measured by the detector, a housing consisting on bricks of polyethylene is built around the detector to enhance its reduction. The basic set-up is displayed in Figure 5.1.

To perform the experiments, the opening in the housing (empty in Figure 5.1b) is filled with different materials. Shielding plates of steel S355MC (Comité Européen de Normalisation 2013) and polyethylene are interposed between the neutron target and the detector. To determine the thickness of the shielding plates, simulations are performed with MCNP6. For this simulations, a F5 Tally (see section 3.2) is modelled in air at

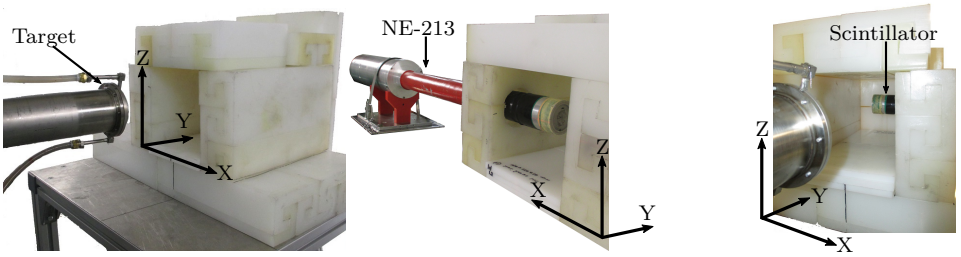

(a) Polyethylene housing at the end of the beamline

(b) Position of the NE-213 detector (before closing the backside of the housing)

(c) View from end of the beamline into the housing showing the scintillator region of the detector

FIGURE 5.1: Experimental set-up where the Y axis points in the direction of the neutron beam.

25 cm distance from a 2.5 MeV neutron point source to register the flux. If the thickness of the interposed plates is too small, no significant flux difference is observed. However, if it is too thick a small amount of particles hit the detector producing poor quality results. Hence, placing a shielding materials (polyethylene or steel) between the neutron source and the tally position should reduce the flux by about one order of magnitude. Simulations performed for different combinations of polyethylene and steel S355MC show that 10 cm polyethylene reduce the flux approximately by one order of magnitude. Applying additional 8 cm steel reduces the flux further by the same amount. When performing the experiments, the distance between the deuterium target of the neutron generator and the detector (y-direction) is set due to technical reasons to 35.5 cm instead 25 cm. Plates of polyethylene with an area of 15 cm x 15 cm and a thickness of 1 cm and plates of steel S355MC with an area of 15 cm x 15 cm and a thickness of 0.5 cm are employed to built the different shieldings. In total, four different experimental configurations have been designed: (See their corresponding MCNP6 models in Figure 5.2)

- **Detector alone:** Detector free in air without any housing (Figure 5.2a).
- **Housing:** A housing consisting of bricks of polyethylene is built around the detector. Its function is to reduce the nonspecific background. To allow target neutrons reaching directly the detector, an open window is left between the generator and the detector (Figure 5.2b).
- **Housing+PE:** The window in the housing is filled with 10 polyethylene plates to study the effect of moderation (Figure 5.2c).
- **Housing+Steel+PE+Steel:** A POLLUX® cask is composed by an internal shielding cask, a neutron moderator and a second shielding cask. To approximate it, a shielding of 8 steel S355MC plates, 10 polyethylene plates and 8 steel S355MC

plates are interposed in the polyethylene house between the neutron generator and the detector (Figure 5.2d).

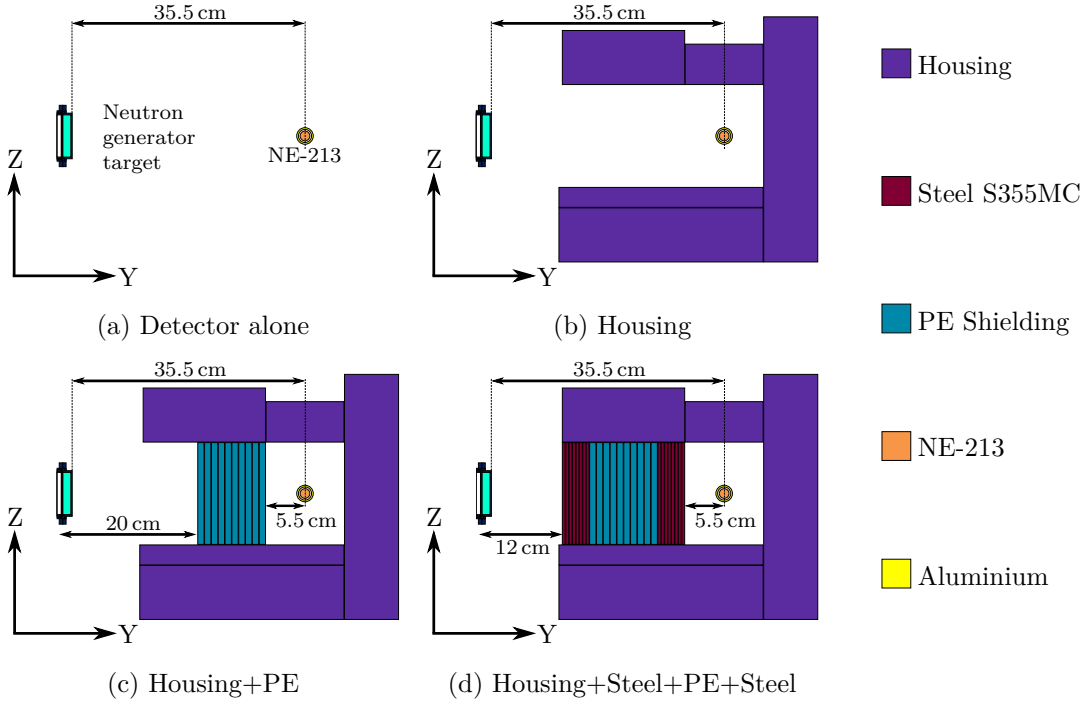

FIGURE 5.2: Side view of the MCNP6 model of the four performed experiments (for details of the neutron generator target see Figure 5.3). Axis according to Figure 5.1

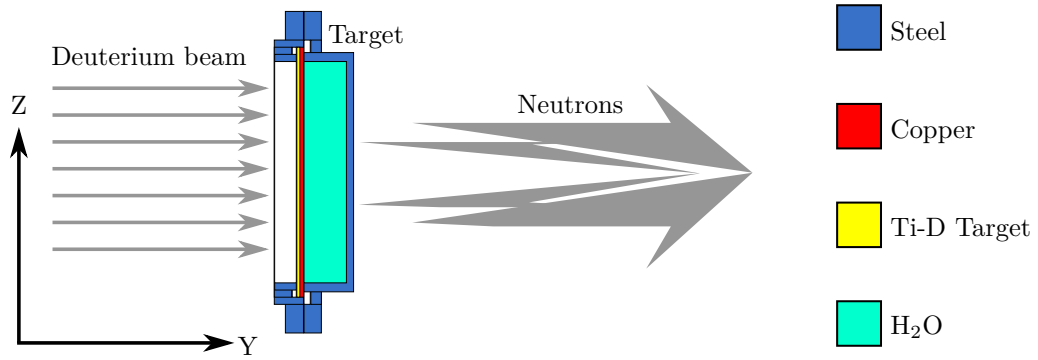

FIGURE 5.3: Cross-sectional cut of the neutron generator target at HZDR

For each experiment, a measurement time of 30 min is used. Since many interactions take place in the detector, the F5 tally cannot be taken. Instead, a *F4 Tally (see section 3.2) has been defined in the position of the detector to obtain the neutron and gamma spectra.

5.2.2 Calibration of the NE-213 detector

A NE-213 detector is used to register neutron and gamma radiation flux spectra. The detector consists of a photomultiplier tube coupled to a liquid NE-213 scintillator (Scherzinger et al. 2017; Batchelor et al. 1961). When the scintillator is exposed to gamma-rays, they interact dominantly with the atomic electrons of the scintillator atoms. The released electrons are almost minimum ionizing and produce very fast flashes of light. Neutrons interact dominantly with the hydrogen nuclei of the scintillator molecules via scattering. These both phenomena have very different decay-time constants. The pulse obtained from each reaction can be amplified and electronically analysed to identify and separate those pulses due to neutron-induced events in the detector from those due to photon-induced events. Figure 5.4 shows the neutron and gamma counts for a measurement with the NE-213 detector, where the function of the control diode (right-upper corner on Figure 5.4) is to verify that the electronic is correctly calibrated.

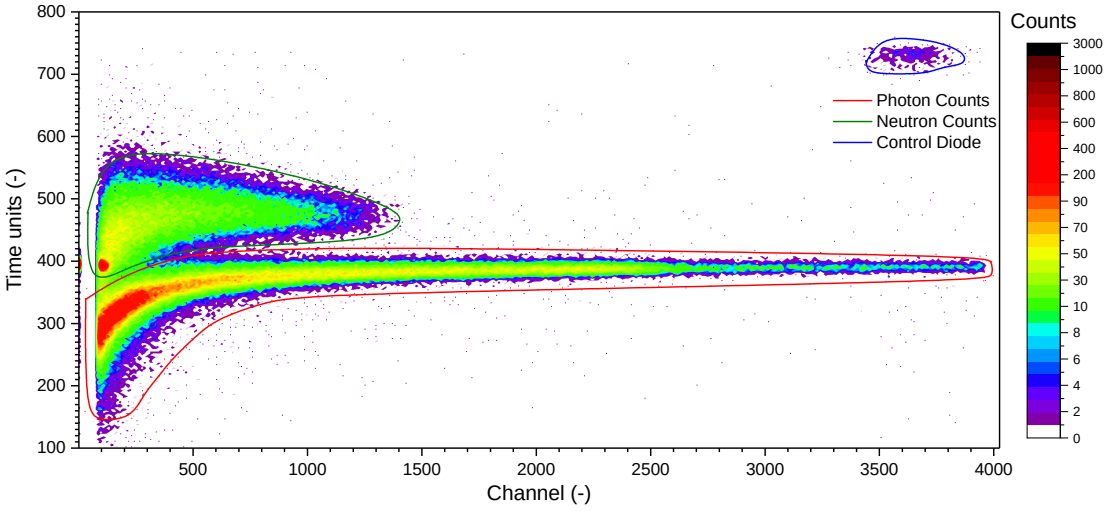

FIGURE 5.4: Neutron and gamma spectra measured with the NE-213 detector.

The NE-213 detector gives its output in form of counts per channel, while a channel corresponds to an energy level. Therefore, it is necessary to convert it to a flux to interpret the results. The NE-213 detector raw data are registered in spectra with 4096 channels but they are re-binned to 1024 channels for further processing. The calibration from the channel to the energy domain is performed with a ^{22}Na source.

Two compton edges can be shown in the raw spectrum of ^{22}Na as illustrated in Figure 5.5a. The first one has an energy of 340 keV (corresponding to the peak at 511 keV from an electron-positron annihilation) and corresponds to channel 83. The second one has an energy of 1068 keV (corresponding to the peak at 1270 keV from a gamma emission) and corresponds to channel 315. Solving the system from Equation 5.4 the values of m and b can be found according to Equation 5.5.

$$\left.\begin{array}{rcll} 340 & = & m \cdot 83 & +b \\ 1068 & = & m \cdot 315 & +b \end{array}\right\}, \tag{5.4}$$

$$Energy\ [\text{keV}] = \frac{22}{7} \cdot Channel + \frac{716}{9}. \tag{5.5}$$

Equation 5.5 allows to convert the channel numbers into keV. To perform the unfolding procedure, the program MAXED from the UMG package (Reginatto et al. 2004) is used. UMG is a package of programs for the analysis of data measured with spectrometers that uses unfolding techniques. The program MAXED, from the UMG package, applies the maximum entropy principle to the unfolding problem. A flat spectrum is provided to MAXED as "guess spectrum" to perform the unfolding procedure. Figure 5.5b shows the ^{22}Na spectrum after unfolding plus energy calibration. Experimentally validated response matrices for this detector are available for unfolding of gamma and neutron spectra (Guldbakke et al. 1994)

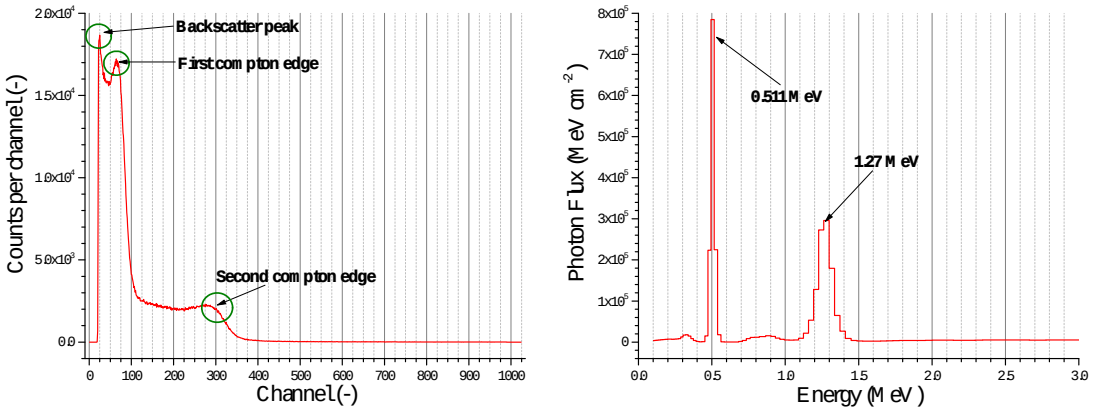

(a) Unfiltered raw data

(b) Spectrum after calibration and unfolding in energy domain

FIGURE 5.5: Measured ^{22}Na spectra obtained with the Ne-213 detector.

5.2.3 Numerical model

The neutron field produced by the neutron generator is not a pure 2.5 MeV field but shows an energy distribution and angular dependence due to the reaction kinematics in the Ti-D target as well as scattering in the target assembly. Since MCNP6 cannot directly take into account the production of neutrons by ions, an input source that includes the angular dependence of the energy distribution provided by other calculations can be employed in MCNP6 (Erhard et al. 2014).

The WHIYIE module from DROSG-2000 code (Drosg 2017) calculates angular differential thick-target neutron yields of white neutron sources that are based on two-body reactions. WHIYIE calculates at a chosen angle a white spectrum which can be used as source for MCNP6. If data for each desired angle are calculated, an angle-dependent source can be defined in MCNP6.

The neutron yield (n/s) emitted from the target is measured by a semiconductor detector (IAEA 1996) (PIPS® detector (Camberra 2016)) with an aperture diameter of 1.55 mm located 50 cm upstream the target. This detector measures the protons produced by the D+D reaction (Equation 5.3). The anisotropy for the determination of total neutron yield from the proton yield is considered by assuming the anisotropy factors published by (Ruby et al. 1963).

5.3 Evaluation of the neutron and gamma spectra

5.3.1 Experimental observation

The measured neutron spectra for the four different configurations are shown in Figure 5.6. For all the measurements, two prominent peaks are observed. The one at an energy of 2.5 MeV, which corresponds to the expected neutron energy of the D+D reaction. The other one around 1.7 MeV is attributed to the inelastic scattering of 2.5 MeV neutrons on iron and copper. Both materials are placed around the target position and are submerged to $(n, n'\gamma)$ reactions as illustrated schematically in Figure 5.7). According to the first excitation state of ^{56}Fe, a $(n, n'\gamma)$ reaction produces gammas with an energy of 0.846 MeV, while for ^{65}Cu produces gammas with an energy of 0.77 MeV. This would reduce the energy of the scattered neutrons to 1.6 MeV-1.7 MeV which is in agreement with the peak position observed in the measured spectra.

Almost no difference is recognized when comparing the configuration "Detector alone" with the configuration “Housing”. The intensity of the flux is almost the same for both spectra. However, the housing has been maintained in the other configurations on the one hand as a support for the shielding plates and on the other hand to ensure a suppression of potential backscattered neutrons and photons induced by the additional material of the shielding plates. The neutron flux is reduced by almost one order of magnitude when the opening on the target side of the housing is closed. Insertion of steel plates in the "Housing+Steel+PE+Steel” configuration reduces about another order of magnitude of the measured intensity of the 2.5 MeV peak due to the larger amount of shielding material. These reductions are in agreement with the simulations

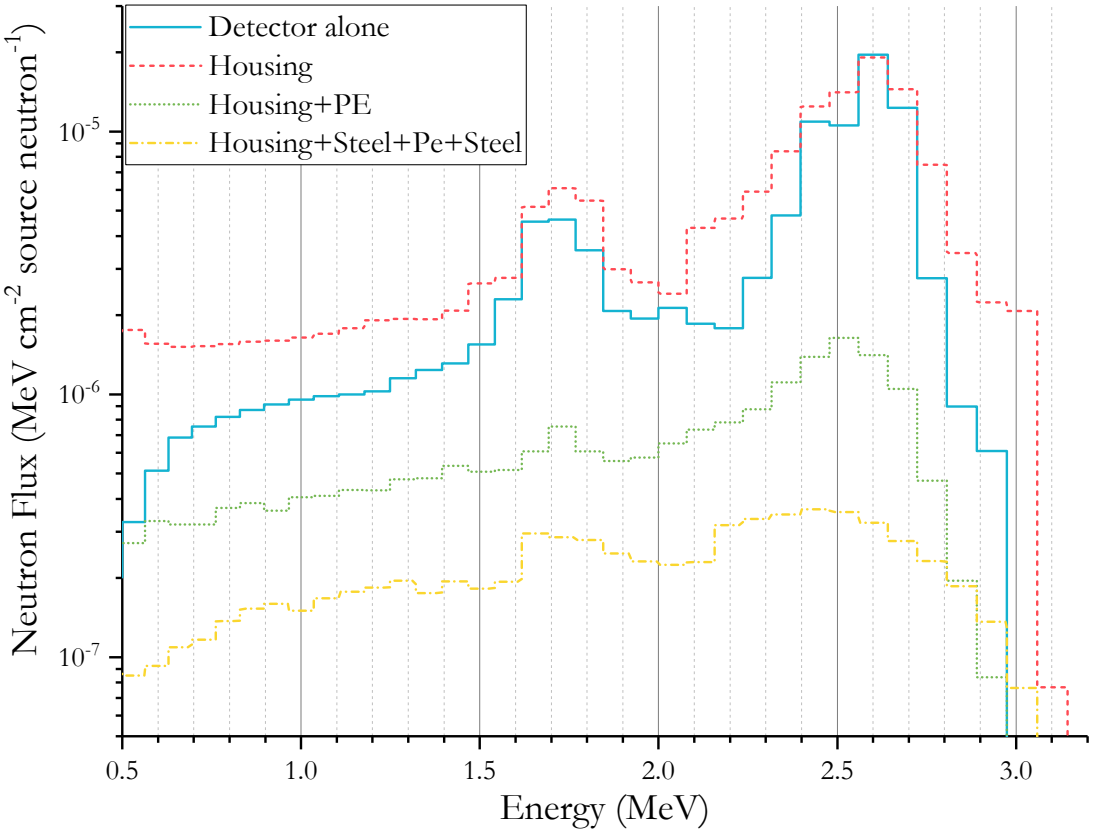

FIGURE 5.6: Measured neutron flux spectra for different configurations at the TUD-NG

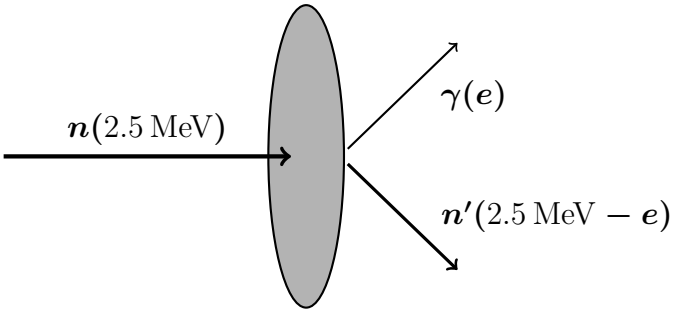

FIGURE 5.7: Schematic representation of the $(\mathrm{n}, \mathrm{n}'\gamma)$ reaction, where e is the produced γ-ray energy

performed with the monoenergetic 2.5 MeV point source to establish the thickness of the shielding plates.

The corresponding measured photon spectra for the four different configurations are shown in Figure 5.8. The NE-213 detector has a low resolution for photons and therefore, it is not able to differentiate the gamma energy lines. Instead, a curve including many of them is observed. The experimental photon spectrum "Detector alone" includes photons stemming from the target area and unspecific background from the surrounding area in the experimental cave. The main peak at 0.9 MeV is attributed to the inelastic scattering of 2.5 MeV neutrons on iron and copper. The polyethylene housing reduces

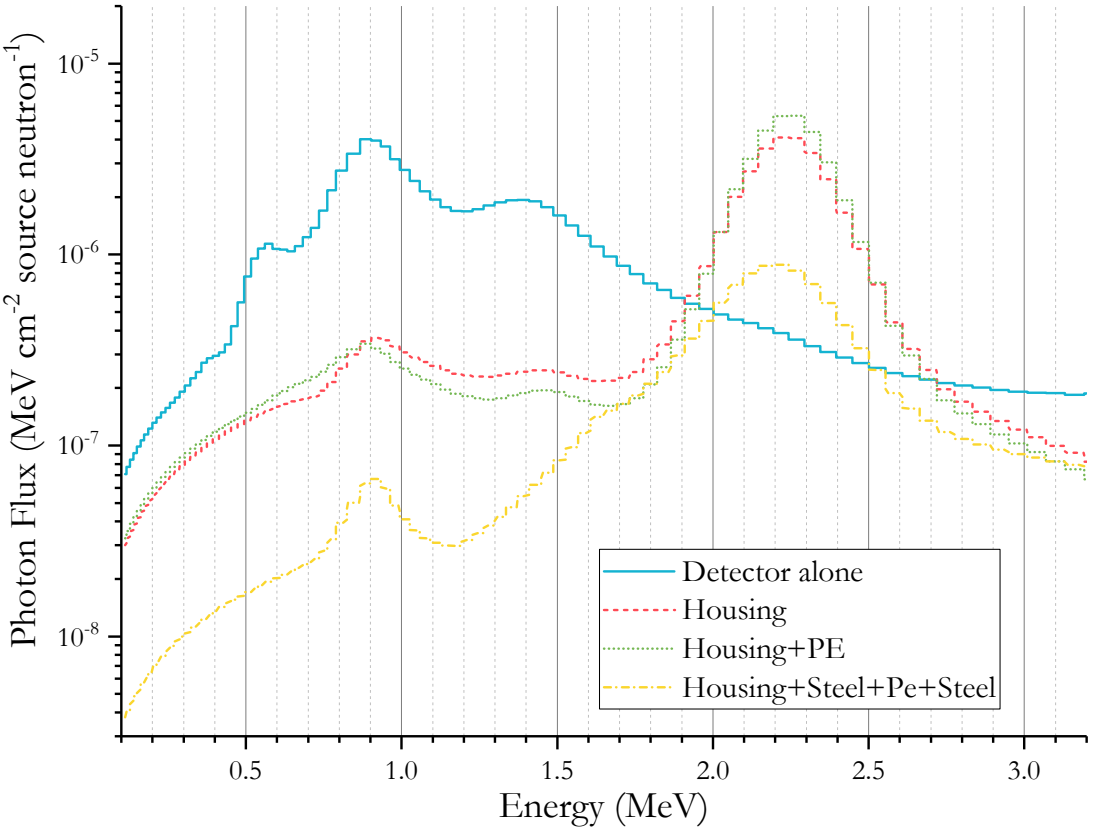

FIGURE 5.8: Photons spectra of the performed experiments with the TUD-NG

the background and the photons coming from the inelastic scattering at the target. A dominating peak arises at 2.2 MeV originated from the thermal neutron capture gammas from ^{1}H. The addition of the polyethylene shielding between the generator and the target ("Housing+PE") increases the peak at 2.2 MeV since more neutron interact with the polyethylene shielding. If a steel shielding ("Housing+Steel+PE+Steel") is included the intensity of the whole spectrum is reduced.

5.3.2 Comparison of experiments with MCNP6 simulations

Figure 5.9 shows for the different configurations the resulting MCNP6 neutron spectra compared with the experiments. Since the experimental set-up presents some uncertainties that are not reflected in the simulation model, like the omission of the complete neutron generator set-up and environment including the NE-213 mounting in the simulations, some differences are expected. Although the peaks at 1.7 MeV and 2.5 MeV from the measurements are present in all the simulations, the intensity and width of the peaks exhibit differences. Table 5.1 shows for the experiments and the MCNP6 simulations the area for peaks at 1.7 MeV and 2.5 MeV and for the full spectrum. Also in the table

is shown the difference in percentage between both, which is given by

$$Difference[\%] = \frac{A_{MCNP6} - A_{Experimental}}{A_{MCNP6}} \cdot 100, \tag{5.6}$$

where A_{MCNP6} is the area of the peak calculated with MCNP6 and $A_{Experimental}$ is the area of the peak measured in the experiments.

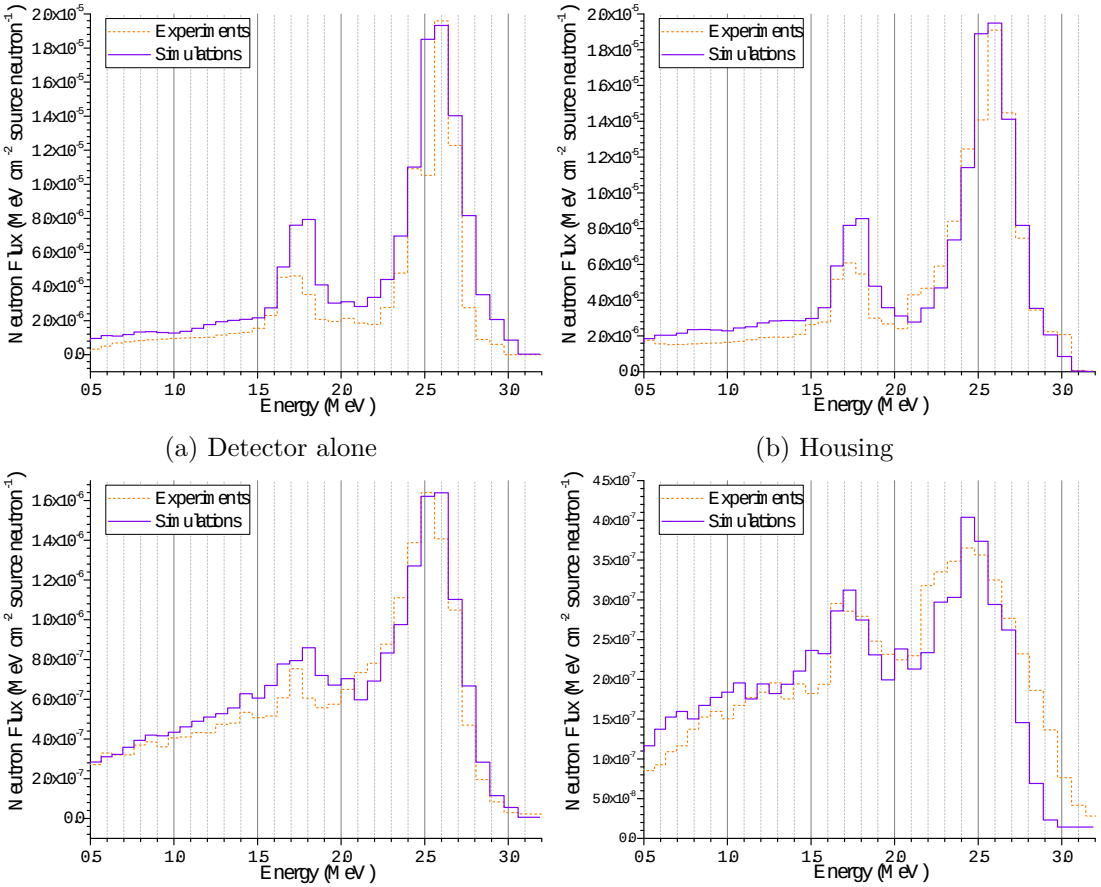

(a) Detector alone

(b) Housing

(c) Housing+PE

(d) Housing+Steel+PE+Steel

FIGURE 5.9: Comparison of the neutron spectra from experiments and MCNP6 simulations

For the "Detector alone" configuration the area of the simulation is in average 31 % larger than the measured one. This is attributed to the simplifications in the model that reduce the probability of the neutrons to interact with other materials and reach the detector. However, the addition of the polyethylene housing reduces this difference to 11 % confirming the importance of the housing to reduce boundary conditions. For the "Housing+Steel+PE+Steel", experiments show a flux 3 % higher than for simulations. This is due to the simplification when modelling the steel shielding. A better concordance between experimental and calculated data for the peak at 2.5 MeV that for the one at 1.7 MeV is observed for all the configurations, which is attributed to the lower resolution

TABLE 5.1: Calculated MCNP6 neutron flux area (in MeV cm^{-2} source^{-1} n^{-1}) and comparison with the experimental results.

	Detector alone	**Housing**	**Housing+PE**	**Housing+Steel +PE+Steel**
Peak at 1.7 MeV (area between 1.5 MeV to 2 MeV)				
Experiments	1.90×10^{-5}	2.52×10^{-5}	3.61×10^{-6}	1.34×10^{-6}
Simulations	3.06×10^{-5}	3.46×10^{-5}	4.49×10^{-6}	1.30×10^{-6}
Difference	38 %	27 %	20 %	−3 %
Peak at 2.5 MeV (area between 2.25 MeV to 3 MeV)				
Experiments	6.24×10^{-5}	8.76×10^{-5}	8.22×10^{-6}	2.56×10^{-6}
Simulations	8.36×10^{-5}	8.97×10^{-5}	8.51×10^{-6}	2.17×10^{-6}
Difference	25 %	2 %	3 %	−18 %
Total spectrum				
Experiments	1.04×10^{-4}	1.55×10^{-4}	2.04×10^{-5}	7.38×10^{-6}
Simulations	1.52×10^{-4}	1.73×10^{-4}	2.21×10^{-5}	7.18×10^{-6}
Difference	31 %	11 %	8 %	−3 %

of the NE-213 at lower energies. In general, there is an average difference of 10 % between simulations and measurements.

For the measured gamma spectra, depicted in Figure 5.8, the low resolution of the NE-213 detector does not resolve nuclide specific γ-ray transitions, instead, an "envelope curve" is observed in contrast to MCNP6 simulations where clear peaks can be observed. However, the resolution of the detector can be included in the MCNP6 inputs through the Gausian Energy Broadenig (GEB) card to simulate the "envelope curve." As described in (Goorley et al. 2013) the Full Width at Half Maximum (FWHM) of the energy broadening in a physical detector is defined by

$$\mathrm{FWHM} = a + b\sqrt{E + cE^2}, \tag{5.7}$$

where E is the energy of the particle and a, b and c are measured in MeV, MeV$^{1/2}$ and 1/MeV, respectively. The values of a, b and c can be obtained solving the system:

$$\left.\begin{aligned} \mathrm{FWHM}_1 &= a + b\sqrt{E_1 + cE_1^2} \\ \mathrm{FWHM}_2 &= a + b\sqrt{E_2 + cE_2^2} \\ \mathrm{FWHM}_3 &= a + b\sqrt{E_3 + cE_3^2} \end{aligned}\right\}, \tag{5.8}$$

where the subscripts 1, 2 and 3 indicate the different energies. As shown in Figure 5.8, for the performed experiments only two gamma peaks are well defined, the one at 0.9 MeV

and the one at 2.2 MeV. Therefore the system of Equation 5.8 cannot be solved. However, for simplification, it is assumed that the FWHM has a linear behaviour and therefore, the system of Equation 5.8 is reduced to two energies:

$$\left.\begin{array}{rcl} \mathrm{FWHM}_1 & = & a + b\sqrt{E_1} \\ \mathrm{FWHM}_2 & = & a + b\sqrt{E_2} \end{array}\right\} \quad \left.\begin{array}{rcl} 1.6 \times 10^{-1} & = & a + b\sqrt{0.9} \\ 2.65 \times 10^{-1} & = & a + b\sqrt{2.2} \end{array}\right\} , \tag{5.9}$$

where the values of FWHM are measured in the "Housing" case of Figure 5.8. Solving the system the input values for the GEB yield to:

$$\left.\begin{array}{rcl} a & = & -0.026 \\ b & = & 0.196 \\ c & = & 0 \end{array}\right\} . \tag{5.10}$$

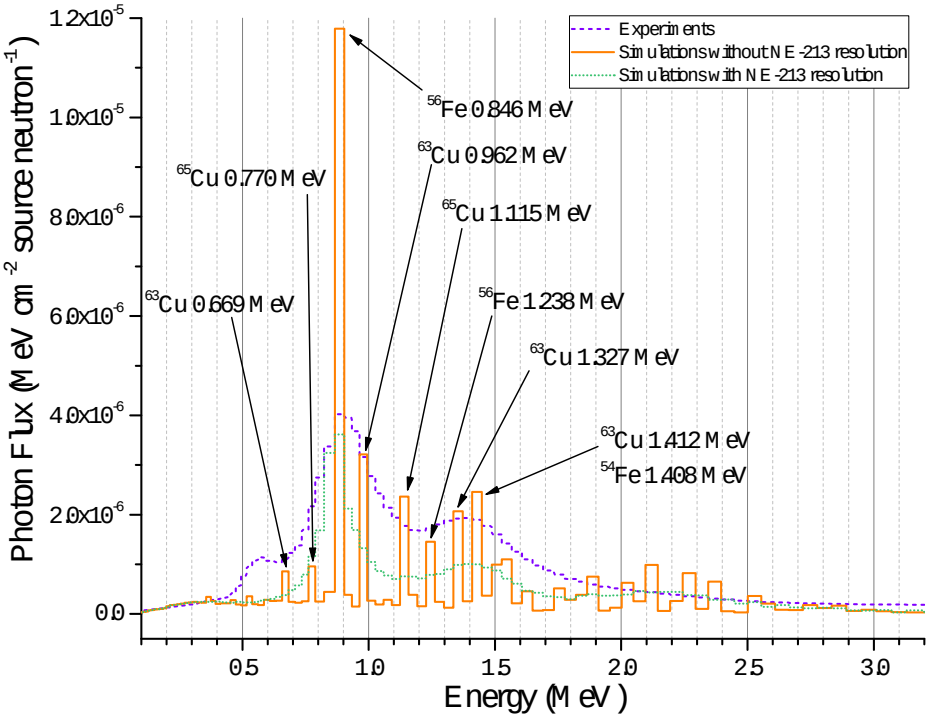

FIGURE 5.10: Resulting MCNP6 spectra for the case "Detector alone" with and without consideration of the detector resolution and comparison with the experimental spectrum

Figure 5.10 shows the MCNP6 spectra for the "Detector alone" with and without considering the NE-213 resolution with the GEB card. Figure 5.12 shows the comparison of the gamma spectra between the MCNP6 simulations with the GEB and the performed experiments for the different configurations. Table 5.2 shows for the experiments and the MCNP6 simulations the area of the enveloped curves peaks and the area of the full spectrum. Also in the table is shown the difference in percentage between simulations and measurements, which is given by Equation 5.6.

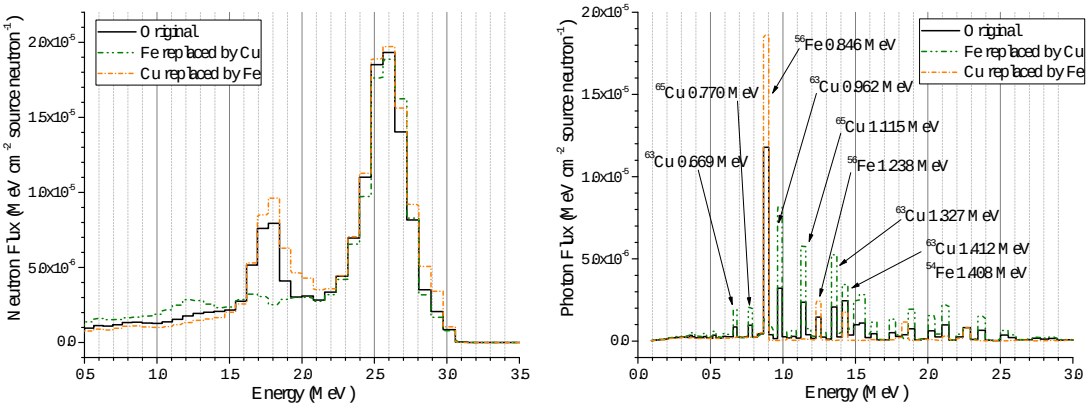

(a) Neutron spectra (b) Neutron induced photons spectra

FIGURE 5.11: Influence of materials at the target position of the neutron generator in the MCNP6 spectra

TABLE 5.2: Calculated photon flux peak area in ($\mathrm{MeV\,cm^{-2}\,source^{-1}\,n^{-1}}$) and comparison with the experimental results.

Flux	**Detector alone**	**Housing**	**Housing+PE**	**Housing+Steel +PE+Steel**
Peak between 0.7 MeV to 1.1 MeV				
Experiments	3.35×10^{-5}	3.41×10^{-6}	3.29×10^{-6}	5.23×10^{-7}
Simulations	1.89×10^{-5}	2.09×10^{-5}	1.36×10^{-5}	2.77×10^{-6}
Difference	−77 %	84 %	76 %	81 %
Peak between 1.3 MeV to 1.7 MeV				
Experiments	1.57×10^{-5}	2.34×10^{-6}	1.80×10^{-6}	8.69×10^{-7}
Simulations	7.92×10^{-6}	9.79×10^{-6}	7.36×10^{-6}	2.70×10^{-6}
Difference	−99 %	76 %	76 %	68 %
Peak between 1.9 MeV to 3 MeV				
Experiments	6.40×10^{-6}	2.99×10^{-5}	3.55×10^{-5}	8.41×10^{-6}
Simulations	5.36×10^{-6}	8.70×10^{-5}	6.99×10^{-5}	1.91×10^{-5}
Difference	−19 %	66 %	49 %	56 %
Total spectrum				
Experiments	8.75×10^{-5}	4.35×10^{-5}	4.78×10^{-5}	1.31×10^{-5}
Simulations	4.62×10^{-5}	1.44×10^{-4}	1.13×10^{-4}	3.50×10^{-5}
Difference	−89 %	70 %	58 %	63 %

The MCNP6 simulations were performed considering the target area and experimental set-up but without the unspecific background radiation due to radiation interactions on the environment. Therefore, for the "Detector alone" configuration (Figure 5.12a) the area of the gamma peaks is 90 % higher for the experiments. For the NE-213 detector, the efficiency decreases with decreasing energy. The reason is most

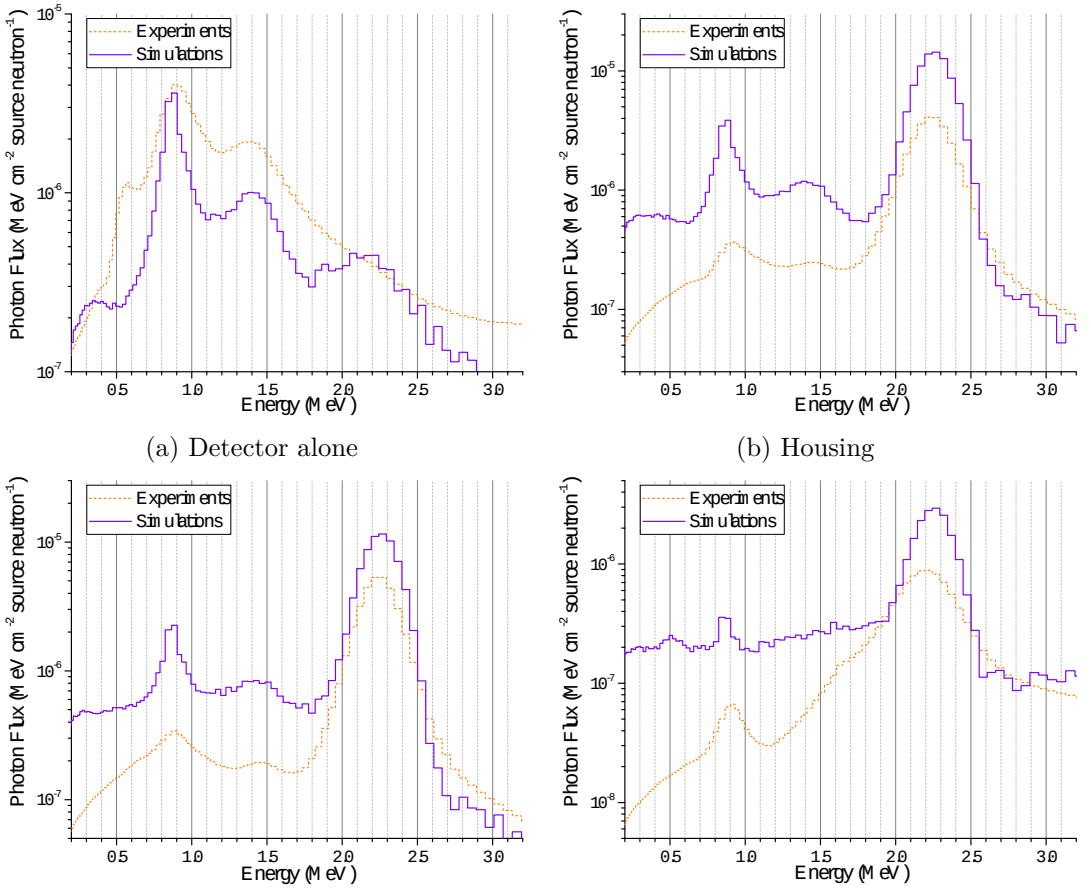

(a) Detector alone

(b) Housing

(c) Housing+PE

(d) Housing+Steel+PE+Steel

FIGURE 5.12: Comparison of the neutron induced photon spectra from experiments and MCNP6 simulations

likely the detector's gamma-ray efficiency depending strongly on the bias/electronic settings (e.g. Lurie et al. (1975)). Since this was not included in the simulations, for the other three configurations (Figure 5.12b, Figure 5.12c and Figure 5.12d), simulations show in average spectra with intensities 70 % higher than the experiments. However, in view of neglecting the influence of the detector efficiency and background radiation, the simulations yield an appropriate description of the spectra.

Simulations for the configuration "Detector alone" with modifications of the materials present at the target position of the neutron generator were performed to confirm the hypothesis presented in the previous section, i.e. the origin of the 1.7 MeV peak from scattering on iron and copper. This time the simulations were performed without folding of the detector resolution in order to reveal the nuclide specific γ-ray transitions. In the first simulation iron was replaced by copper. In the second one, copper was replaced by iron. The neutron and photon spectra for both simulations together with the previous results (Figure 5.9a and Figure 5.12a) are presented in Figure 5.11.

If no iron is present (Figure 5.11a green-dashed line), the 1.7 MeV neutron peak of ^{56}Fe disappears and the peaks corresponding to the gamma transition of ^{63}Cu (1.6 MeV) and ^{65}Cu (1.3 MeV) increase. At the same time, the gamma lines corresponding to the different Fe gamma transition disappear (Figure 5.11b) while the ones from Cu duplicate their intensity. If the copper is replaced by iron (Figure 5.11a orange-dashed line), the gamma transitions of ^{63}Cu and ^{65}Cu disappear and the gamma transitions of ^{56}Fe increases. As shown in Figure 5.11b, the gamma lines corresponding to the gamma transitions of from ^{63}Cu and ^{65}Cu disappear while the ones from ^{56}Fe are stronger than for the ones from the original simulation.

This behaviour confirms the hypothesis suggested in the previous section. An important part of the 2.5 MeV neutrons emitted by the D+D reaction undergo a $(\mathrm{n}, \mathrm{n}'\gamma)$ inelastic scattering reaction on the iron and copper around the target position.

5.4 Concluding remarks

In general, for the neutron spectra, experiments and simulations are in good agreement with an average difference of 10 % which is attributed to the simplifications in the simulated model. For the photons spectra this difference increases to 70 % but it can be attributed to the uncertainties in the detector response and the unfolding procedure and the simplifications in the simulated model. Nevertheless, the cross-section libraries might have also an important influence on the results since they are based in a combination of experimental data and physical models. Therefore, it is necessary to perform a study of these libraries to determine their impact in the results. This will be the highlight from chapter 6.

Chapter 6

Uncertainties assessment of dose calculations for a POLLUX® cask

6.1 Goals

In the previous chapter, the capability of MCNP6 models to reproduce the experimental results has been studied. For problems leading with neutrons and photons, MCNP6 can reproduce the experimental results successfully with a deviation of the order of 10 % for neutrons and 70 % for photons. The observed divergences are attributed to simplifications in the numerical model and the sensitivity of the detector used in the experiments.

Besides the simplifications in the simulations, the nuclear data are another factor that might have an important impact on the numerical results. As described in section 3.3, nuclear data are the basic input for neutronic calculations since they describe the different reactions of neutrons with the isotopes present in the model. Although nuclear data files are continuously improved they still contain some uncertainties. Therefore, a realistic estimation of these uncertainties is necessary to quantify the uncertainty threshold of the simulation results.

The work of this chapter is performed using the software package SCALE instead of MCNP6 since as explained in section 3.3 SCALE has the tool SAMPLER designed to perform analysis of uncertainties. The results of this chapter provide a confidence interval of the performed calculations. Since MCNP6 is use to perform analysis of the dose rate and absorbed dose in geological repositories, a comparison between SCALE and MCNP6 is required.

6.2 Modelling of a POLLUX® cask with SCALE

To perform simulations with SCALE, the simplifications described in section 2.4, as the homogeneous distribution of the waste within the core of the cask and the division between active and inactive zone, are applied in the geometry model. Since all the studied casks have the same geometry and similar waste inventories, only a POLLUX-10 cask in vacuum is studied in this chapter. Figure 6.1 shows a representation of the cask in SCALE.

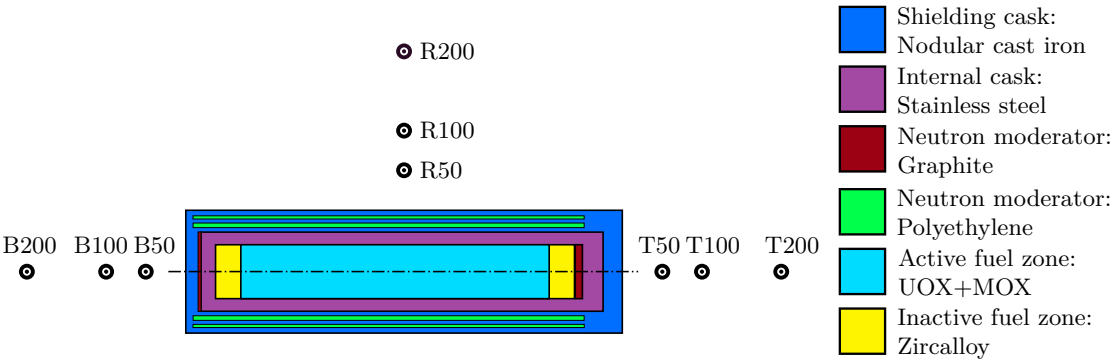

FIGURE 6.1: Schematic representation of a SCALE model for a POLLUX-10 cask and position of the dose detectors. Where the numbers indicate the distance in cm from the cask boundary.

To calculate the ambient dose equivalent rate at 10 mm ($\dot{H}^*(10)$) 9 detectors are defined around the cask (see Figure 6.1) where the Arabic numbers denote the distance to the cask surface in centimetres, and the letters correspond to the three directions of the cask: radial (R), top (T) and bottom (B). Note that in Figure 6.1 the cask is horizontally positioned. For each detector, neutrons and photons are registered. Equation 6.1 shows how to convert the SCALE results in µSv/h.

$$\dot{H}^*(10)(\mu\text{Sv/h}) = F(\#/\text{cm}^2)\cdot A(\text{n/s})\cdot\frac{H^*(10)}{\Phi}(\text{Sv}\cdot\text{cm}^2)\cdot 10^6\,(\mu\text{Sv/Sv})\cdot 3600\,(\text{s/h}) \quad (6.1)$$

where F is the obtained value with SCALE, A is the activity and $\frac{H^*(10)}{\Phi}$ are the fluence-to-ambient-dose-equivalent conversion coefficients given by (ICRP 1997).

6.3 Perturbations in the cross sections with SAMPLER

The SCALE package has in its database covariance matrices which account for uncertainties of the nuclear cross sections of several specific isotopes. These matrices are

the basis to generate data variations with SAMPLER since the probability distributions of the uncertain parameters are used to generate random variations.

When applying this method with neutron cross section uncertainties, a new nuclear data library is generated for each simulation, where all quantities with available uncertainties (inelastic and elastic scattering, capture cross sections, fission cross sections and neutrons per fission) are varied at the same time for all nuclides in the model. A total of 100 simulations with random perturbations of the neutron cross sections are performed. Additionally, SAMPLER performs an extra simulation with the unperturbed library as a comparison basis.

As described in section 3.3 the main limitation of the current version of SCALE is the impossibility for the user to see which cross sections are randomly perturbed in each simulation. It means that the provided output does not give access to the modified data of the perturbed library. Moreover, SAMPLER does not offer the possibility to control the cross sections variations, for example to restrict perturbations to only a few isotopes. These limitations, make it very complicated to determine the origin of the differences in the calculated $\dot{H}^*(10)$ values.

Figure 6.2a and Figure 6.2b show $\dot{H}^*(10)$ at 1 m of the POLLUX-10 top surface (T100 in Figure 6.1) for the 100 performed cases for neutrons and neutron induced photons, respectively. For each simulation $\dot{H}^*(10)$ is represented by a blue dot together with its error bars. These errors bars represent the error interval of the simulation and depends of the NPS reaching the detector. Also in the graphics $\dot{H}^*(10)$ is included for the unperturbed case (continuous-black line) and a 10 % interval of confidence (red-dashed lines). This 10 % interval is established as maximal deviation to consider the perturbed simulations similar to the unperturbed case. The results for the other detectors can be found in Appendix A.

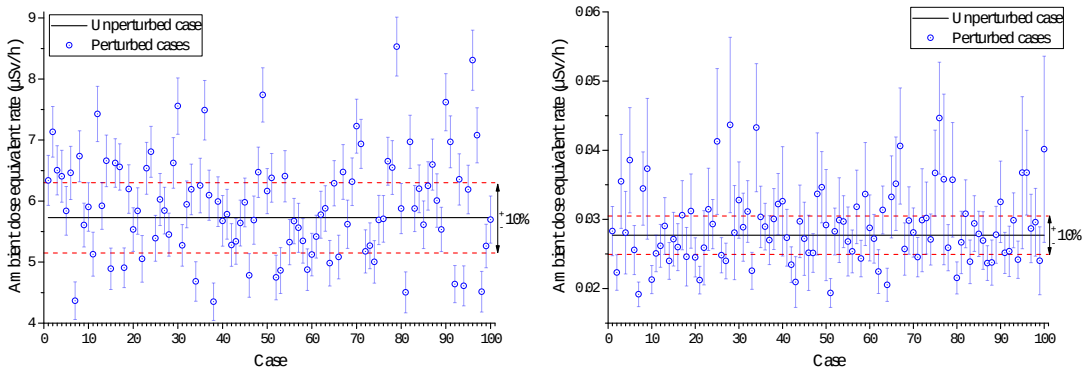

(a) Neutrons (b) Neutron induced photons

FIGURE 6.2: Calculated $\dot{H}^*(10)$ dose at position T100 for the 100 cases by SAMPLER.

100 of 100 cases for neutrons and 46 of 100 for photons are within the 10 % interval of confidence. If the error bars are considered, 76 cases for neutrons and 81 for photons are inside the confidence interval. This means that the cross sections have a measurable impact on the computed $\dot{H}^*(10)$ results of a POLLUX® cask. However, it is of minor significance since the majority of the results is within the 10 % confidence threshold.

Table 6.1 presents for each detector the minimum, maximal and average deviation of the 100 randomly perturbed cases from the unperturbed case. The deviation does not take the error bars in account. For neutrons, the average $\dot{H}^*(10)$ deviation is lower than 12 %. However, for some perturbations, this deviation can be up to 50 % of the unperturbed value. For photons the deviation with respect to the unperturbed value is in average around 16 % but it can reach up to 60 % for some cross section perturbations.

TABLE 6.1: Minimum, maximum and average deviations (absolute values) for $\dot{H}^*(10)$ at 50 cm, 100 cm and 200 cm to the POLLUX-10 surface

	Top		**Bottom**		**Radial**	
	Neutrons (%)	**Photons** (%)	**Neutrons** (%)	**Photons** (%)	**Neutrons** (%)	**Photons** (%)
			50 cm to POLLUX-10 surface			
Minimum	0.2	0.08	0.05	0.07	0.2	0.09
Maximum	51	51	24	18	46	24
Average	12	18	7	5	12	6
			100 cm to POLLUX-10 surface			
Minimum	0.4	0.2	0.01	0.1	0.06	0.03
Maximum	49	60	24	21	43	16
Average	12	16	7	5	12	3
			200 cm to POLLUX-10 surface			
Minimum	0.2	0.003	0.1	0.005	0.07	0.01
Maximum	49	64	24	19	42	10
Average	12	13	7	5	12	3

As explained above, the main limitation of the current version of SCALE is the impossibility to obtain an output with the randomly perturbed cross sections for each case, which would allow to identify the isotope contributing most to the observed deviations. For example, the maximum deviation in the top direction is given by case number 79. For the same case, the deviation at the bottom and at the radial direction is 30 % and 10 %, respectively. This could for example indicate an extreme perturbation of the cross sections of ^{12}C (main component of the graphite moderator present at the top and bottom). This perturbation would imply a deviation in the $\dot{H}^*(10)$ results for these directions, especially at the top since the amount of graphite is higher. Another possibility could be for example that the cross section perturbation in case 79 orginates

from ^{56}Fe (main component of the cask). A larger thickness in the top direction implies a higher probability of neutron interactions with ^{56}Fe. If more interactions between neutrons and ^{56}Fe take place, the probability that $\dot{H}^*(10)$ differs from the unperturbed value increases. In the radial direction, the maximum deviation takes place for case 30. For the same case, the difference for the top and radial directions are around 57 %, respectively. The origin of this deviation could be for example the perturbation on the ^{1}H cross section (main component of the polyethylene moderator).

The hypothesis above cannot be confirmed without a description of the perturbed cross sections for each simulation. Nevertheless, taking into account the restrictions named above (inability of controlling perturbed isotope cross-sections) it can be set-up that in average, the cross section perturbations do not have a high impact in the variation of $\dot{H}^*(10)$ within a 10 % confidence level.

6.4 SCALE unperturbed vs. MCNP6

The simulations performed in the previous section confirm that in average the perturbations in the cross sections result in a difference of around 12 % on $\dot{H}^*(10)$ when compared with the unperturbed case. Nevertheless, the majority of calculations are performed with MCNP6, which also uses the ENDF cross section libraries. Therefore, to translate the conclusions of this chapter to MCNP6, it is necessary to check if the results obtained with MCNP6 comply with those from SCALE.

For this purpose a POLLUX-10 is modelled in vacuum with MCNP6 with F5 tallies to measure $\dot{H}^*(10)$ at the nine positions indicated by the detectors of Figure 6.1 and the same NPS. The results from MCNP6 are compared with the unperturbed values obtained by SAMPLER.

Figure 6.3 shows the calculated $\dot{H}^*(10)$ values at the different positions obtained by SCALE and MCNP6. For neutrons (Figure 6.3a) the difference between SCALE and MCNP6 oscillates between 7 % for detector T50 to 27 % for detector T100. In average the different between both is lower than 15 %. For secondary photons (Figure 6.3b) the differences are even smaller with an average lower than 10 % and a minimum and maximum of 1 % and 18 %, respectively. For the same number of simulated particles, MCNP6 results show a statistical error being smaller by 50 % as compared to the results obtained by SCALE. Nevertheless, both errors are lower than 10 %, which is the maximum error accepted to ensure results confidence.

The differences have two possible origins. First, the detector tallies. As explained in section 3.2, the variance reduction technique of the next event estimator assumes that

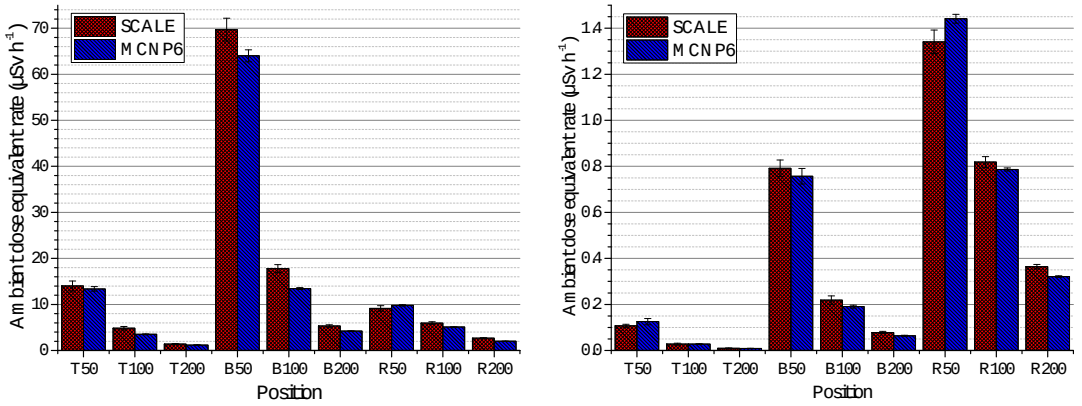

(a) Neutrons (b) Neutron induced photons

FIGURE 6.3: Comparison of the calculated $\dot{H}^*(10)$ values of SCALE and MCNP6 at different distances from the POLLUX® cask.

calculations are being performed in a uniform medium. Even if vacuum is a uniform medium, the presence of the cask perturbs the results. A way to solve this is the use of surface or cell detectors. These detectors do not use variance reduction techniques and therefore, possible errors due to the medium will are reduced. However, such an approach is extremely time consuming and since the agreements between SCALE and MCNP6 results are satisfactory for this study, no further effort has been undertaken.

The second source of differences are the cross section libraries employed in SCALE and MCNP6. The SAMPLER module can only work with multi-group libraries. Although MCNP6 has multi-group libraries, many important isotopes required to model the POLLUX® cask are not available. Therefore, for the MCNP6 simulations continuous energy libraries are selected. A solution is to repeat the calculations by SCALE using continues energy libraries. But since the agreements between SCALE and MCNP6 are satisfactory this aspect may be subject of future investigation.

To conclude, the differences of both SCALE and MCNP6 are small enough to affirm consistency for the calculated problem. Therefore, it can be assumed that perturbations on the ENDF cross section libraries of MCNP6 yield a similar behaviour as obtained for SCALE.

6.5 Concluding remarks

In a high-level waste repository a mixed neutron-gamma radiation field emerges from the SNF contained in the shielding casks. Therefore, dosimeters able to measure both radiations are required. However, as described by Zhang (2011) mixed neutron-gamma fields still present a challenge to determinate the neutron dose due to the complex

interactions of neutrons with matter making the majority of dosimeters not able to measure neutrons with the same accuracy as photons.

The results exposed here show that randomly perturbed cross sections have an influence on $\dot{H}^*(10)$ dose calculations. Nevertheless, the computational uncertainty and error margin are small compared to the error of measurements of personal and ambient dose performed with neutron-gamma dosimeters. This means, that for the dose study in a geological repository performed in the following chapter, the main source of differences between measurements and simulations are rather the uncertainties in the cross sections than the error obtained by the measurements.

Chapter 7

Dose rate and absorbed dose in geological repositories

7.1 Scope and goals of the analysis

In chapter 5, the reliability of MCNP6 to simulate sources with neutrons and photons has been verified and validated through the experiments performed with the TUD-NG. There, MNCP6 has demonstrated to reproduce properly neutron and gamma spectra with an accuracy of 10 %. In chapter 6 the interval of confidence for the ENDF libraries has been studied. Although some differences are observed in the results when performing perturbations in the cross section libraries, they are of marginal quantity. Hence, the interval of confidence from MCNP6 and experiments is considered as reliable. This proof is the pre-requisite to analyse the dose rate and absorbed dose in geological repositories.

In this chapter, an operational approach to estimate occupational radiation exposure during the disposal of high level nuclear waste is performed. The ambient dose and the personal dose are analysed for the different waste inventories (POLLUX-10, POLLUX-3M and POLLUX-3U) and host rock formations (salt rock and claystone). To study the influence of different parameters (disposed waste, host rock, etc.) on the radiation field, the $\dot{H}^*(10)$ is used as indicator. To investigate the influence of the worker position on the absorbed dose, a phantom is modelled representing a human worker inside the drift. Detectors are integrated in the phantom to calculate the personal dose equivalent rate at 10 mm ($\dot{H}_p(10)$) and simulations for the RSD with different angles between phantom and POLLUX® cask are studied. Finally, the methodology is applied to an anticipated operational disposal scenario in rock salt and claystone. For both host rock formations, a comparison of the personal dose is conducted and discussed.

7.2 Modelling a POLLUX® cask in a realistic repository configuration

7.2.1 Geometric specifications of the POLLUX® MCNP6 model

To study the dose rate and absorbed dose in the selected geological repositories, a POLLUX® cask is modelled. To perform the MCNP6 simulations, the simplifications described in section 2.4, as the homogeneous distribution of the waste and division between active and inactive zone, are applied to the MCNP6 POLLUX® cask. Figure 7.1 shows the MCNP6 model of the POLLUX® cask.

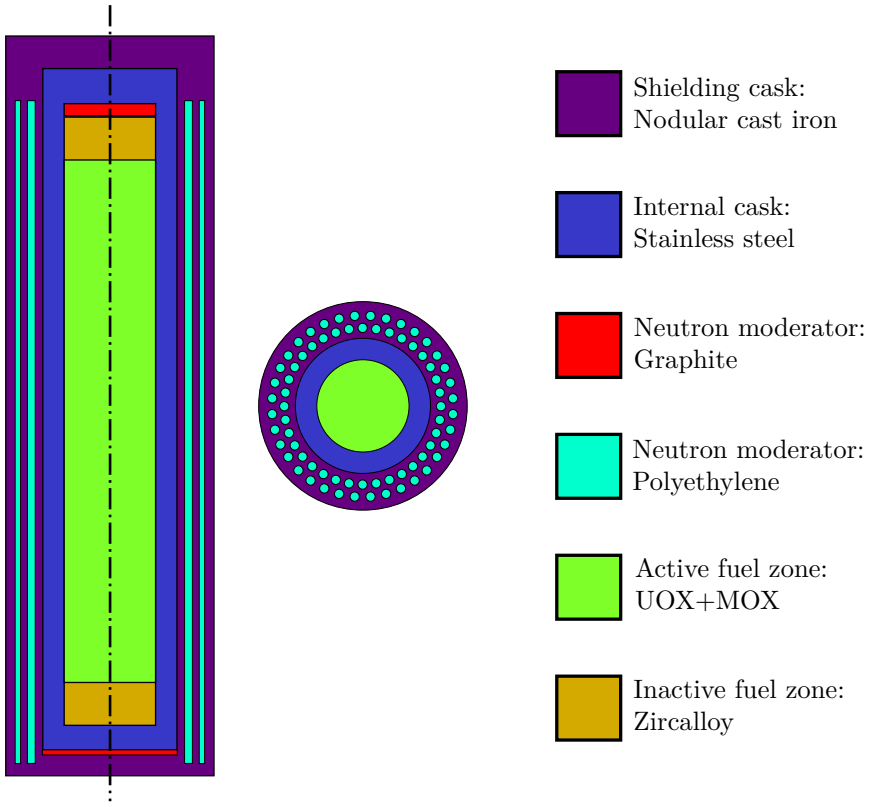

FIGURE 7.1: Schematics of the MCNP6 model of a POLLUX® cask with dimensions as in Figure 2.4 and assigned material composition.

For the disposal in the RSD, a POLLUX-10 (9 UOX FAs and 1 MOX FA) is considered as a reference container. For the CLD host formation, due to temperature restrictions the maximum amount of FAs per cask is set to 3. Therefore, one POLLUX-3M (3 UOX FAs and 1 MOX FA) and two POLLUX-3U (3 UOX FAs) are considered to simulate the emplacement in CLD.

7.2.2 Modelling of a horizontal emplacement drift with MCNP6

As described in section 2.3, an emplacement drift is usually hundreds of meters underground and surrounded by a host rock layer or several decimetres of concrete lining in the case of a claystone or crystalline drift. To simplify the calculations the thickness of the drift walls, i.e. rock salt for POLLUX-10 and concrete lining for POLLUX-3M and POLLUX-3U, is set to 1 m in the MCNP6 model, which is sufficient to account for possible interactions of the radiation with the drift wall materials. Figure 7.2 illustrates the MCNP6 modelling and dimensions of the deep geological disposal facility for a POLLUX® cask. As a simplification, only one POLLUX® cask is placed on the ground of the drift with its bottom surface at 2.63 m distance to the drift end side. Detailed geometrical information of the drift can be found in (Leon Vargas et al. 2017). The composition of the rock salt and concrete lining can be found in (Bernnat et al. 1995) and (Albert et al. 2010), respectively. An average density of 2.4 g cm^{-3} for rock salt and 2.16 g cm^{-3} for the concrete lining in the CLD are assumed. The air inside the drift is modelled as dry air at near see level. To study the impact of the radiation scattered by the drift layers, a third drift is modelled. This one has the same geometry as the ones described above but the surrounding layers are replaced by air, representing a POLLUX® Free In Air (FIA). In **??** a more detailed description of the MCNP6 input can be found.

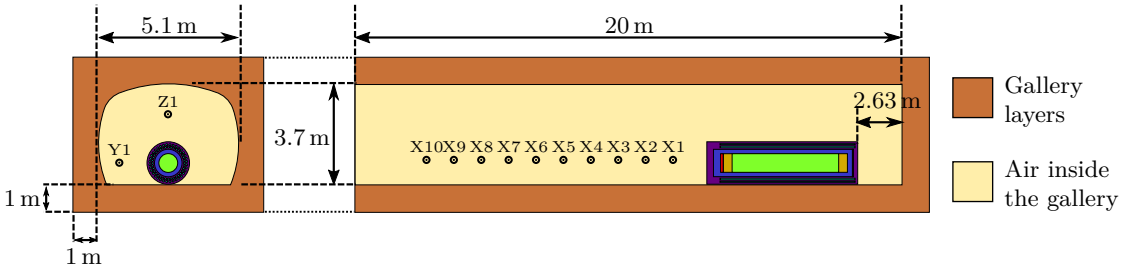

FIGURE 7.2: MCNP6 model and dimensions of the emplacement drift with a POLLUX® cask loaded with SNF.

7.2.2.1 Calculation of $\dot{H}^*(10)$

Since air is a low density material only a few interactions take place in it. Hence, the F5 tally can be employed to obtain the $\dot{H}^*(10)$ and the spectra in the drift. Twelve F5 tallies are employed to calculate $\dot{H}^*(10)$ and spectra at different positions inside the drift, indicated as black dots in Figure 7.2 where the letters denote. the axis direction and the numbers the distance in meters to the POLLUX® surface. Tallies X1, Y1 and Z1 are defined to compare $\dot{H}^*(10)$ at 1 m distance to the POLLUX® cask surface in the respective direction. To study the evolution of $\dot{H}^*(10)$ as a function of the distance to

the POLLUX® cask, the tallies X1 to X10 are employed. Equation 6.1 is used to convert the F5 tally in µSv/h.

$$\dot{H}^*(10)(\mu\mathrm{Sv/h}) = F5\,(\#/\mathrm{cm^2 n}) \cdot \frac{H^*(10)}{\Phi}(\mathrm{Sv \cdot cm^2}) \cdot A(\mathrm{n/s}) \cdot 10^6\,(\mu\mathrm{Sv/Sv}) \cdot 3600\,(\mathrm{s/h}), \tag{7.1}$$

where $\frac{H^*(10)}{\Phi}$ are the fluence-to-ambient-dose-equivalent conversion coefficients given by (ICRP 1997) and A is the activity for each cask (see section 4.2). For the spectra, the F5 tally is multiplied by the activity to obtain the flux in $\mathrm{cm^{-2}\,s^{-1}}$.

7.2.3 Modelling of a human phantom with MCNP6

As recommended by (ICRP 2007) the personal dose equivalent rate ($\dot{H}_p(d)$) at a depth $d = 10\,\mathrm{mm}$ gives a conservative assessment of the effective dose under most irradiation conditions. However, this requires the personal dosimeter to be worn at a position on the body which is representative with respect to the exposure. The ICRP recommends to wear a dosimeter in front of the chest, where $\dot{\mathrm{H}}_\mathrm{p}(10)$ is supposed to give a conservative estimation of the effective dose even in cases of lateral or isotropic radiation incidence on the body. However, the question arises if a dosimeter worn at the front still appropriately assesses the effective dose in cases of exposure from the back. In order to study the influence of the backscattered radiation on $\dot{H}_p(d)$, a worker inside the drift is modelled in this study by a simplified anthropomorphic phantom, which is a virtual representation of the BOttle MAnnikin ABsorber (BOMAB) phantom (U.S. Department of Energy 2015). Figure 7.3 shows the MCNP6 model of the phantom and Table 7.1 provides a detailed description of its components. The original phantom is composed of polyethylene but in the simulations it is replaced by human tissue (Reed 2007).

TABLE 7.1: Detailed dimensions and shape composition of the BOMAB phantom

Body parts	**Cross section shape**	**Cross section dimensions (cm)**	**Height (cm)**
Head	ellipsoid	19 × 14	20
Neck	circular	13	10
Chest	ellipsoid	30 × 20	40
Pelvis	ellipsoid	36 × 20	20
Arms	circular	10	60
Thighs	circular	15	40
Calves	circular	12	40

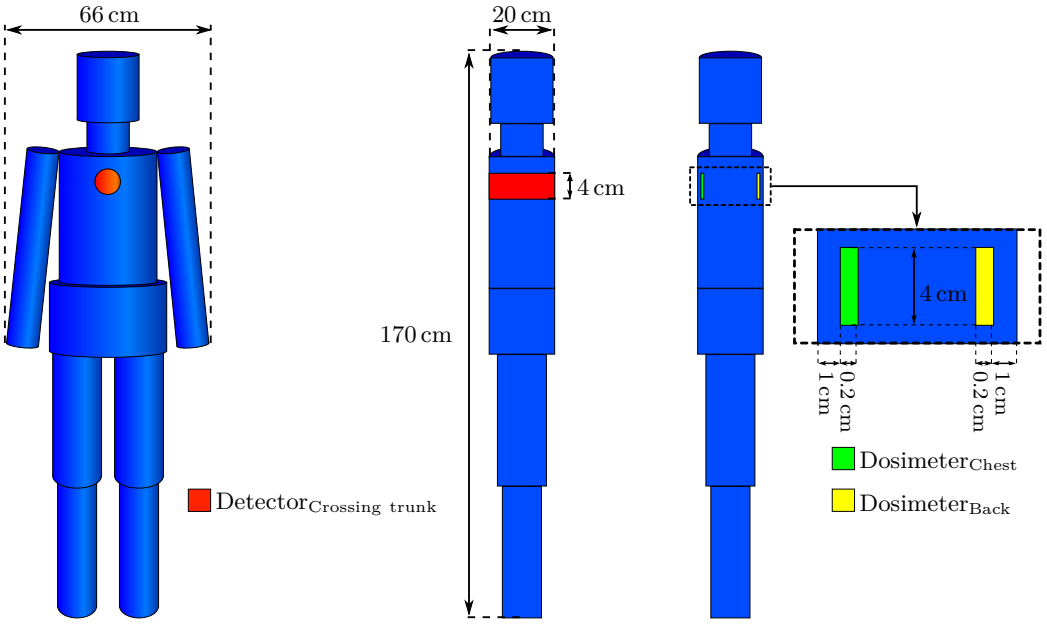

(a) Frontal view with the detector at the chest (b) Side view with the detector crossing the trunk (c) Detailed view of the frontal and back detector

FIGURE 7.3: Shape and dimensions of the modelled BOMAB phantom in MCNP6

Some studies like (Vana et al. 2003) denote that for complex sources, $\dot{H}_p(10)$ might underestimate the radiation exposure since the maximal dose rate can reach deeper than 10 mm into the body. To study the evolution of the dose within the body, a 4 cm radius cylindrical detector is modelled in the centre of the chest, as illustrated in Figure 7.3a. The detector crosses the chest and measures the dose every 1 mm of the 20 cm thick chest (Figure 7.3b). This allows to study the $\dot{H}_p(d)$ at different depths and also to evaluate the influence of the surrounding layers in the absorbed dose.

7.2.3.1 Calculation of $\dot{H}_p(d)$

The MCNP6 energy deposition tally F6 is used to estimate the absorbed dose (D) (ICRP 2007), which can be converted in $\dot{H}_p(d)$ according to Equation 7.2:

$$H_p(d) = H_{p_n}(d) + \dot{H}_{p_\gamma}(d) = \int_{E_{min}}^{E_{max}} \left(D_n(E)Q_n(E) + D_\gamma(E)Q_\gamma(E)\right) dE, \tag{7.2}$$

where Q is the quality neutron factor, which it is equal to 1 for photons (γ) while for neutrons (n) it is dependent on the energy (E) and the linear energy transfer (L) according to:

$$Q_n(E_n) = 1/D \int_{L_{min}}^{L_{max}} Q(L)D(L, E_n)dL. \tag{7.3}$$

Tabulated values for $Q_n(E_n)$ are taken from (Siebert et al. 1995).

7.3 Factors impacting the dose rate in a repository

7.3.1 Contribution of the different radiation types

To study the contribution of each radiation type to the total $\dot{H}^*(10)$ simulations are performed for each POLLUX® cask in vacuum. F5 tallies are stablish for the three directions of the cask, i.e. lateral, top and bottom of the cask. To obtain the evolution of $\dot{H}^*(10)$ in vacuum the tallies are located at 0.5 m, 1 m, 2 m, 4 m, 7 m and 9 m. To pass the MCNP6 statistical checks the NPS required for the neutron, gamma and beta source are 1×10^7, 1×10^8 and 1×10^9 NPS, respectively.

Figure 7.4 presents $\dot{H}^*(10)$ as a function of the distance at the top of POLLUX-10. Since this is the direction from which the workers are receiving the majority of the dose (according to the disposal position of the cask in the drift from Figure 7.2), only this case is analysed in this context in more detail. The results for POLLUX-3M and POLLUX-3U, as well as the results in the other two directions can be found in Appendix A.

For the studied waste inventory, neutrons are responsible for more than 99 % from the total $\dot{H}^*(10)$ while photons induced by interactions of neutrons with the materials of the cask contribute less than 1 % to the total dose. The contribution from primary photons and photons produced by beta interactions is almost 0. Therefore, only the contribution of neutrons will be taken into account to study the impacting factors in $\dot{H}^*(10)$.

7.3.2 Influence of the waste inventory composition

To study the influence of the waste inventory, $\dot{H}^*(10)$ has been calculated at 1 m distance from the POLLUX® surface in each direction, i.e. at the top, bottom and lateral of the cask. Simulations are performed in vacuum and F5 tallies are employed to calculate $\dot{H}^*(10)$. To pass the MCNP6 statistical checks, 1×10^7 NPS are required for each simulation.

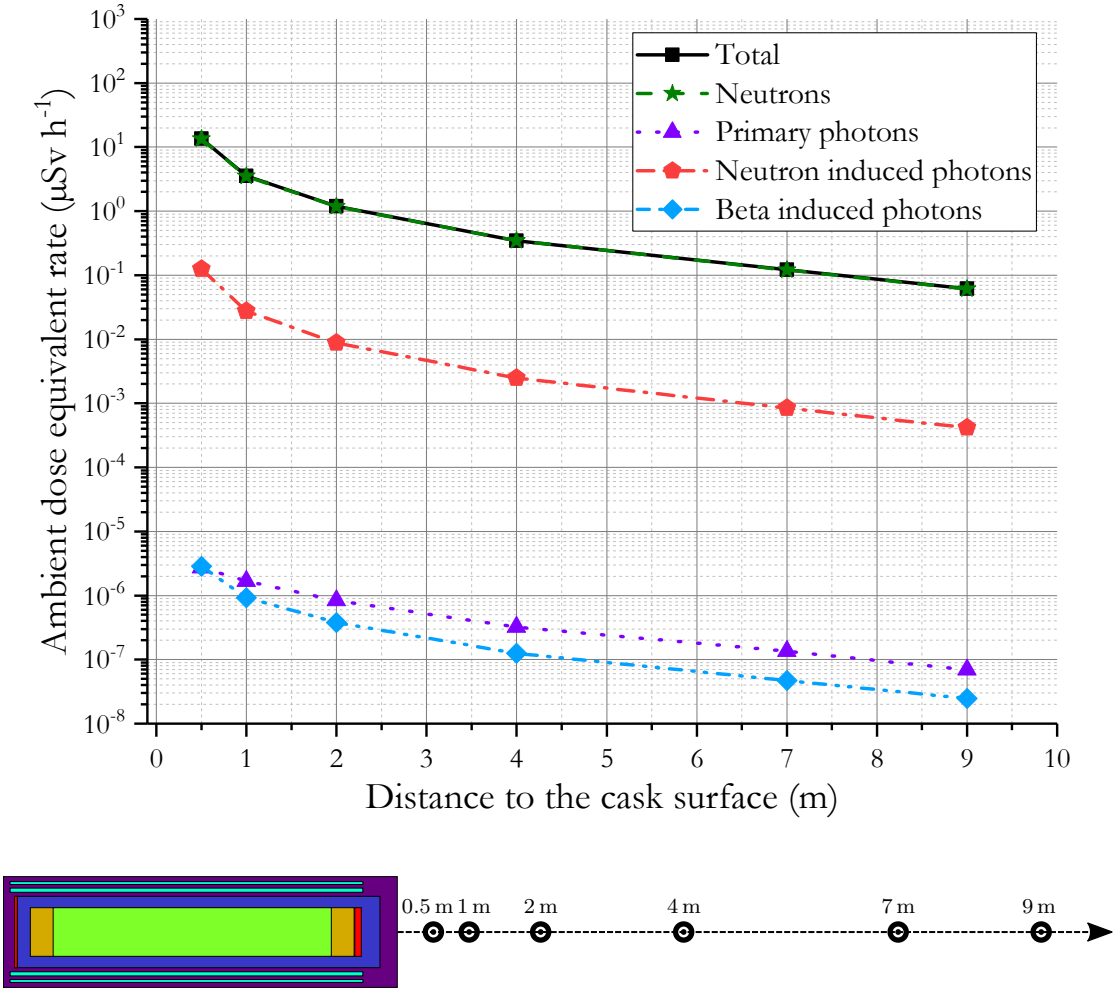

FIGURE 7.4: Calculate contribution of different radiation types to $\dot{H}^*(10)$ for POLLUX-10 in vacuum.

Figure 7.5 shows for the different casks the $\dot{H}^*(10)$ dose at 1 m distance in each direction. Since the POLLUX® shielding is thickest at the top, $\dot{H}^*(10)$ outside the cask in this direction is the lowest followed by the lateral and the bottom direction. When comparing the different cask types, the lateral dose of the POLLUX-10 is 10 % lower than the one of the POLLUX-3M lateral and 75 % higher than for the POLLUX-3U lateral, while in the top and bottom $\dot{H}^*(10)$ outside the POLLUX-10 cask is 50 % lower than the one from POLLUX-3M and only 55 % higher than that from POLLUX-3U. This difference can be explained due to the simplifications performed when modelling the FAs and the SNF inside the cask.

The neutron spectra before and after the zircaloy layer of the inactive zone for POLLUX-3M and POLLUX-10 are shown in Figure 7.6. Before the inactive zone the

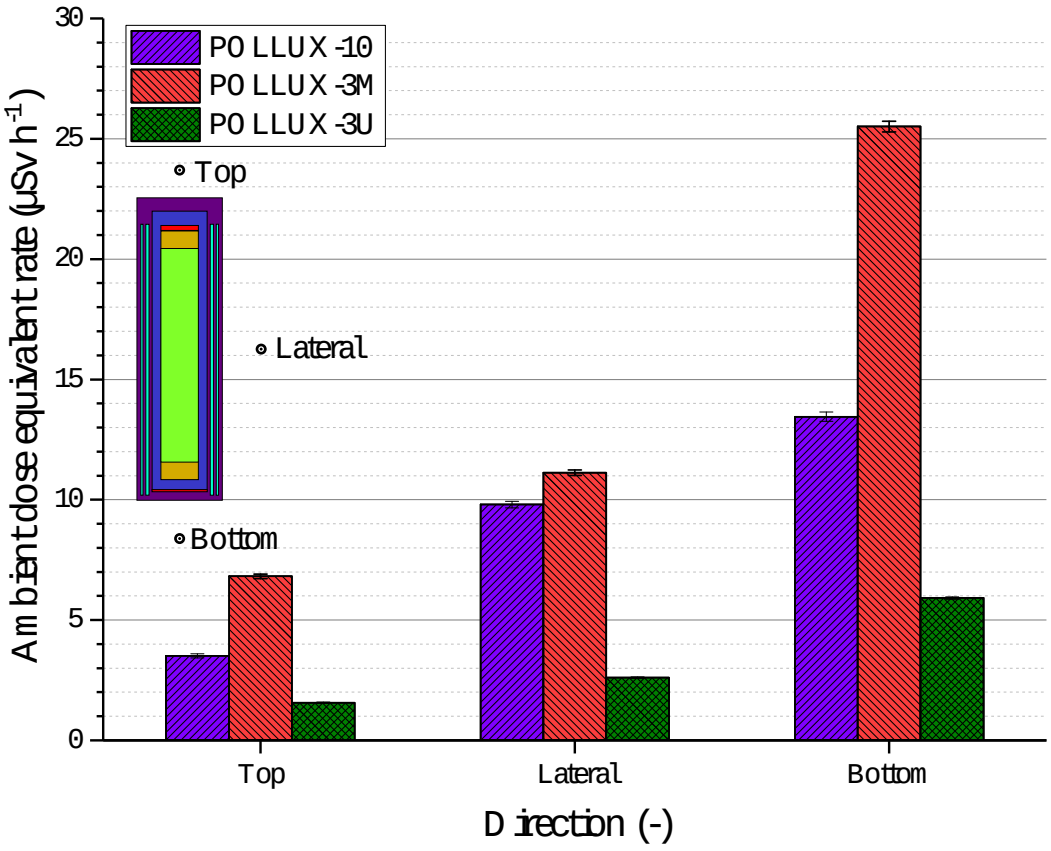

FIGURE 7.5: Calculated $\dot{H}^*(10)$ at 1 m distance from the POLLUX surface for each cask

total neutron fluence rate is higher for POLLUX-10 (3536 $cm^{-2}\,s^{-1}$) than for POLLUX-3M (2662 $cm^{-2}\,s^{-1}$). According to the simplifications in the waste model (see Equation 2.1 from page 20), the density of the SNF in POLLUX-10 (active and inactive zone) is 3 times larger than for POLLUX-3M. Hence, neutrons emitted in this direction are stronger shielded by the zircaloy layer in POLLUX-10 (total neutron fluence after the inactive zone 1692 $cm^{-2}\,s^{-1}$) than in POLLUX-3M (total neutron fluence after the inactive zone 1873 $cm^{-2}\,s^{-1}$).

The same amount of MOX is stored in POLLUX-10 and POLLUX-3M. However, due to the lower density of the inactive fuel zone for POLLUX-3M, $\dot{H}^*(10)$ is much higher at the top and bottom in comparison with POLLUX-10 . To reduce the received dose inside the drift, the top of the cask must be orientated in the working direction (see Figure 7.2) since $\dot{H}^*(10)$ is lower than at the bottom.

7.3.3 Dependence of host rock conditions on $\dot{H}^*(10)$

To study the influence of the drift layers materials on $\dot{H}^*(10)$ doses, simulations of the three POLLUX® casks are performed for RSD, CLD and FIA configurations. As

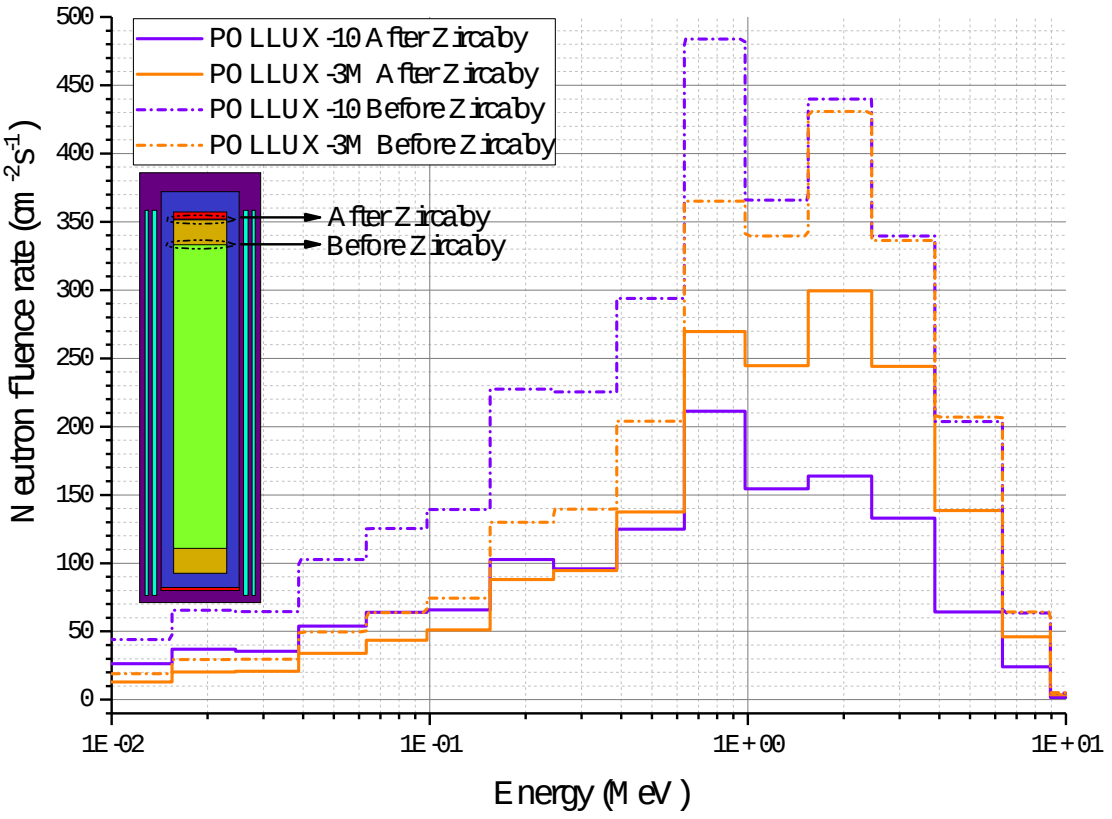

FIGURE 7.6: Calculated spectral neutron fluence rate for the SNF with MCNP6 for 2 cask types.

explained in subsection 7.2.1, the heat emission of a POLLUX-10 is too high to be allocated in a claystone drift. Nevertheless, to compare the influence of the host rock for each cask, simulations of the POLLUX-10 in the CLD are performed. Previously it has been found that the gamma dose coming from the POLLUX® cask (primary photons, neutron induced photons and beta induced photons) is negligibly small. However, neutron interaction with the drift walls materials must be also studied to consider if the neutron induced gamma reactions from the host materials are negligible. Therefore, the induced photons in the drift are also simulated. Since the obtained conclusions are applicable to the three casks, only the results obtained for the POLLUX-10 are shown and discussed. Results for POLLUX-3M and POLLUX-3U can be found in Appendix A.

The evolution of $\dot{H}^*(10)$ with the distance to the POLLUX-10 surface for each host rock is shown in Figure 7.7. For neutrons (Figure 7.7a) the highest $\dot{H}^*(10)$ is observed in RSD. For CLD, $\dot{H}^*(10)$ is between 12 % (at the cask surface) to 41 % (at 10 m distance) lower than that for the casks in RSD. When comparing the $\dot{H}^*(10)$ FIA, it is between 30 % to 88 % lower than $\dot{H}^*(10)$ in RSD and between 20 % to 80 % lower than $\dot{H}^*(10)$ in CLD. These results reveal the important role of the backscattering of the radiation caused by boundaries in a geological disposal facility. As shown in Figure 7.7b, for

gammas the $\dot{H}^*(10)$ dose in CLD is higher than in RSD which is consistent with the results shown for the neutrons since the lower neutron dose in CLD implies a higher neutron interaction with the drift materials and therefore, a higher gamma emission. Nevertheless, the contribution of the induced photons to $\dot{H}^*(10)$ dose is less than 5 %. Even though it is significantly higher than the contribution from the photons coming directly from the POLLUX® cask, it can be neglected and hence is not be further studied.

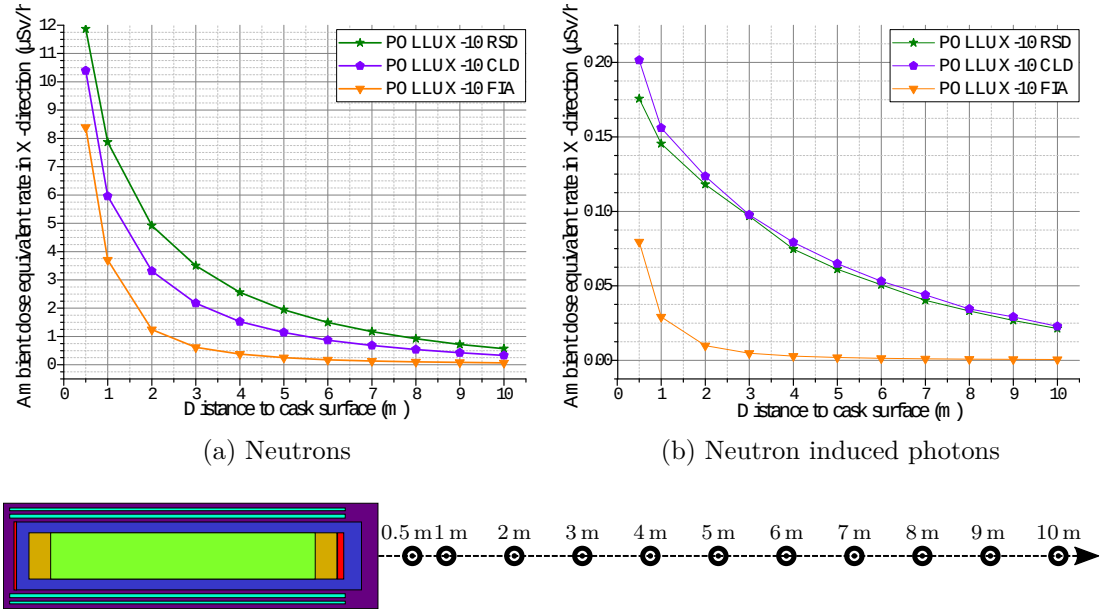

(a) Neutrons

(b) Neutron induced photons

FIGURE 7.7: Calculated distance dependence of $\dot{H}^*(10)$ dose for three different drift layers in the X-direction.

To understand better the dependence of $\dot{H}^*(10)$ on the host rock, Figure 7.8 shows the spectral fluence rate calculated with MCNP6 at 1 m distance from the POLLUX-10 surface in X direction for RSD and CLD as well as for FIA. The relative error of the fluence rates in each energy bin is less than 4 %, except for some bins with fluence rates lower than $0.005\,\mathrm{cm^{-2}\,s^{-1}}$. All the spectra exhibit a peak between 2×10^{-2} MeV to 3×10^{-2} MeV, which is caused by a dip in the neutron elastic cross section of ^{56}Fe at 2.4×10^{-2} MeV, the most abundant isotope of the main shielding material. Neutrons within this energy level have a higher probability to escape from the shielding cask. Therefore, it leads to a peak in the neutron spectra. The effect of the backscattered radiation can be observed for the RSD with the local minimum of the spectral fluence rate between 2×10^{-3} MeV to 3×10^{-3} MeV, which is caused by elastic neutron scattering in ^{23}Na (one of the main isotopes of the surrounding rock salt), which has a peak in the cross section at 2.8×10^{-3} MeV. In the CLD, the maximum between 1×10^{-8} MeV to 1×10^{-6} MeV shows the presence of moderated neutrons mainly due to interactions of neutrons with the ^{16}O content of the concrete layers ($CaO, SiO_2, Al_2O_3, H_2O, \ldots$).

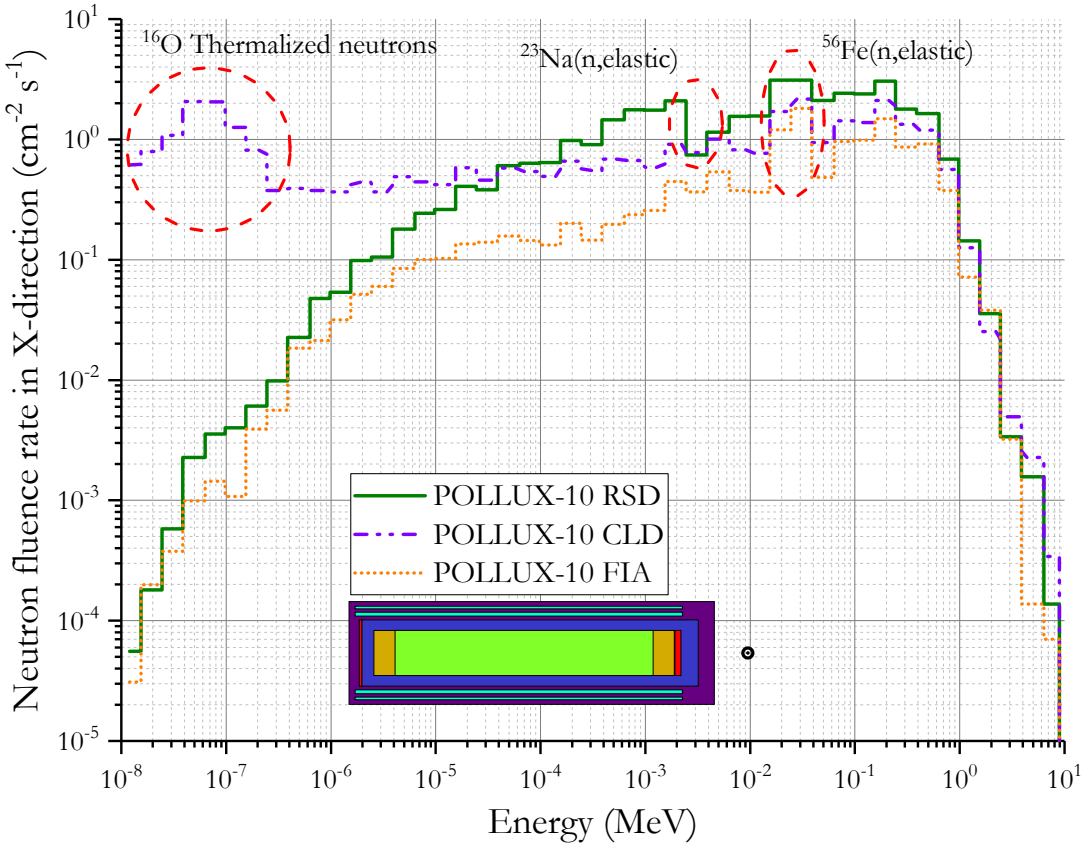

FIGURE 7.8: Calculated spectral neutron fluence rate at 1 m distance from cask surface for different host rocks.

The total neutron fluence rate for POLLUX-10, in RSD, CLD and FIA is 38.12 $\mathrm{cm^{-2}\,s^{-1}}$, 35.40 $\mathrm{cm^{-2}\,s^{-1}}$ and 13.51 $\mathrm{cm^{-2}\,s^{-1}}$, respectively. This explains the higher $\dot{H}^*(10)$ observed in RSD. For POLLUX-3M and POLLUX-3U the same behaviour is observed. Results can be found in Appendix A

To finalize the study of the dependence of host rock conditions on $\dot{H}^*(10)$, the different disposal scenarios, i.e. disposal of POLLUX-10 on RSD and of POLLUX-3M and POLLUX-3U on CLD, are compared.

Figure 7.9 shows that up to 2 m distance, the $\dot{H}^*(10)$ dose is higher (up to 50 %) for POLLUX-3M in CLD than for POLLUX-10 in RSD. For larger distances, the more efficient neutron moderation by the concrete layers and the higher neutron reflection of the salt layers lead to a higher $\dot{H}^*(10)$ dose in the RSD with a POLLUX-10 (between 5 % to 25 %). Since only spent UOX is loaded in a POLLUX-3U cask, the corresponding $\dot{H}^*(10)$ dose for POLLUX-3U is in general 75 % lower than that for POLLUX-3M.

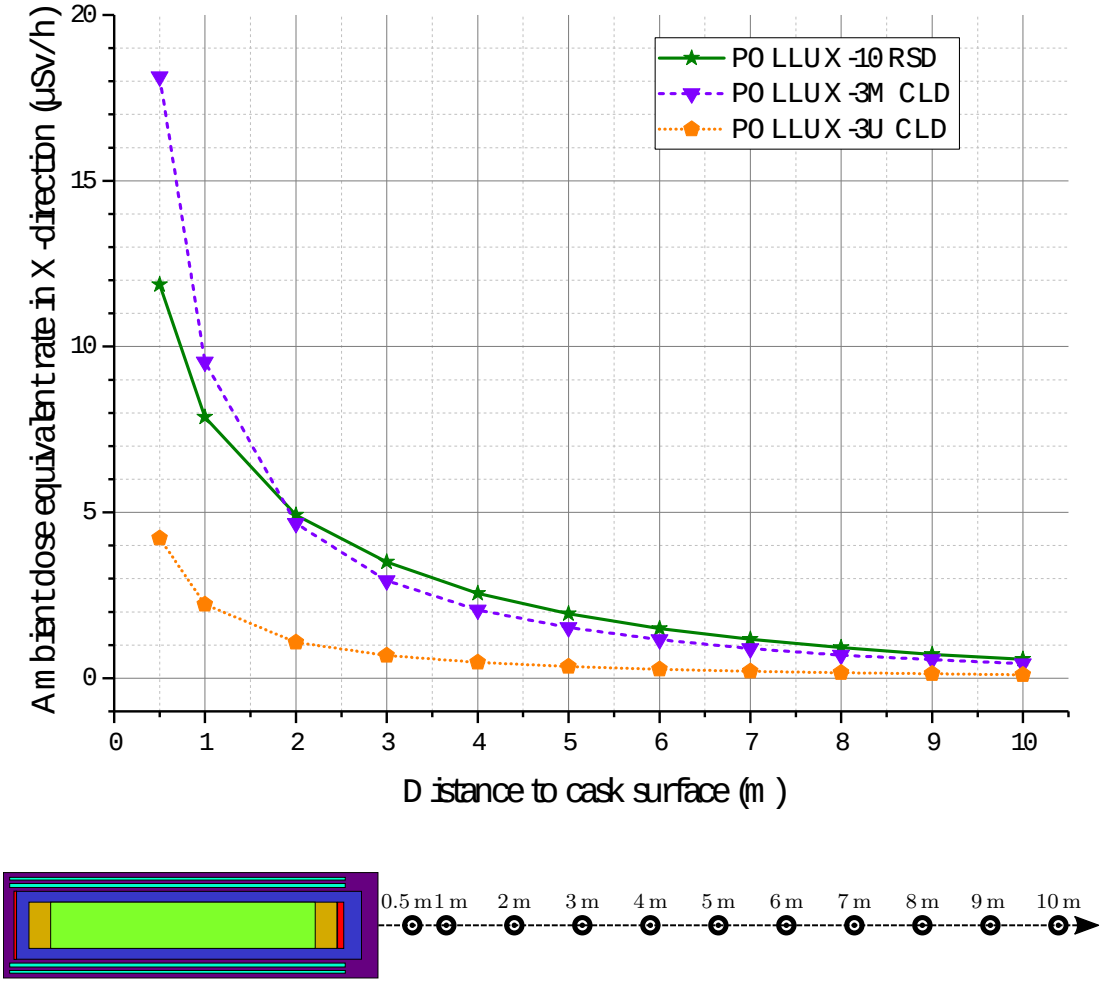

FIGURE 7.9: Calculated distance dependence of the $\dot{H}^*(10)$ dose in the X-direction for different cask types and host formations.

7.4 Assessment of the absorbed dose

The simulations performed in the previous section reveal that neutron emissions dominate the radiation field. Moreover, the backscattered radiation plays an important role in the evolution of the $\dot{H}^*(10)$ dose. However, the radiation field only gives information about the dose distribution in the drift. A proper estimate of the exposure of the workers in a geological repository, requires to employ the $\dot{H}_p(d)$ dose since it is the dose equivalent in soft tissue.

7.4.1 Spatial dependence of absorbed dose from the source

To study the evolution of $\dot{H}_p(d)$ through the body with the distance to the POLLUX® cask, depth-dose curves are calculated for the phantom facing the POLLUX® cask (0°)

at 1 m, 5 m and 10 m distance from the POLLUX-10 in RSD, CLD and FIA. Since the depth-dose curve register $\dot{H}_p(d)$ every mm, they allow to study the variation of $\dot{H}_p(d)$ with the tissue depth. Here, only simulations with the neutron source are performed. However, since neutrons can interact with the body and produce photons, the detectors are modelled to register both neutrons and induced photons in the phantom.

Figure 7.10 shows the depth-dose curve at 5 m distance from the cask for the phantom in RSD, CLD and FIA. The depth-dose curves for 1 m and 10 m can be found in Appendix A. The results exhibit, that $\dot{H}_p(d)$ decreases monotonically with the phantom depth. But, at the last cm an increase for RSD and CLD is observed. Since the increase observed in the simulations FIA is almost negligible, the increase can be only caused by the backscattered radiation from the rock salt and concrete layers. As observed in subsection 7.3.3, a higher amount of neutrons are reflected by the walls. Therefore, for RSD the effect is higher than for CLD.

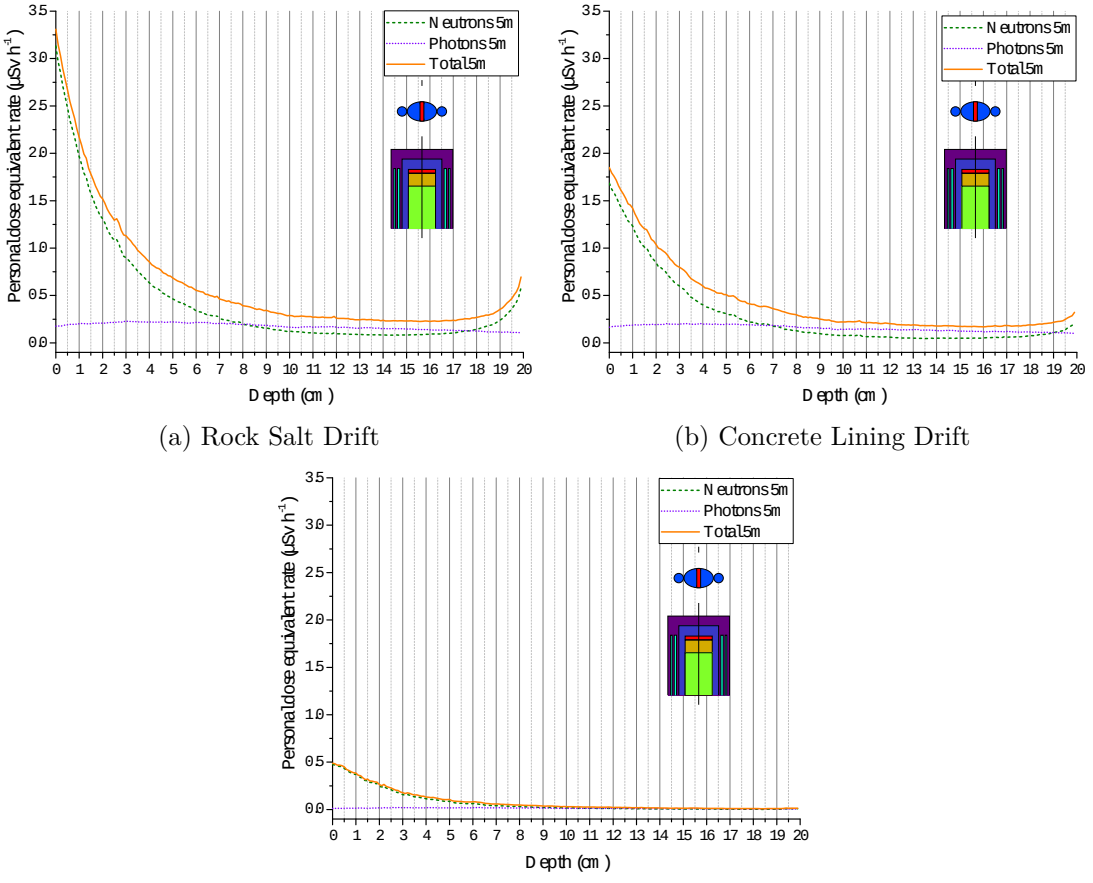

(a) Rock Salt Drift

(b) Concrete Lining Drift

(c) Free In Air

FIGURE 7.10: Calculated evolution of $\dot{H}_p(d)$ dose with depth for a phantom facing the POLLUX-10 at 5 m to its surface.

To determine if neutron induced photons contribute relevant to the $\dot{H}_p(d)$ dose, Table 7.2 presents the contribution interval of photons to the total $\dot{H}_p(d)$ in percentage.

Unlike the neutron induced photons from the drift walls, those produced in the body have a significant contribution to the total $\dot{H}_p(d)$ dose. Since neutrons are absorbed in the phantom, their contribution decreases with the depth. However, the contribution of the induced photons is roughly constant resulting up to certain depth in a higher contribution to the total $\dot{H}_p(d)$ dose. Figure 7.10 and Table 7.2 show the depth range where the contribution of the induced photons to the total $\dot{H}_p(d)$ is higher than the neutron contribution. For both RSD and CLD, $\dot{\mathrm{H}}_{\mathrm{p}_\gamma}(\mathrm{d})$ is very similar. However, the lower $\mathrm{H}_{\mathrm{p_n}}(\mathrm{d})$ in CLD due to the higher absorption of the concrete layers yields a higher percentage of $\dot{\mathrm{H}}_{\mathrm{p}_\gamma}(\mathrm{d})$ contribution in a CLD formation.

TABLE 7.2: Photons contribution to $\dot{H}_p(d)$ and depths where $\dot{\mathrm{H}}_{\mathrm{p}_\gamma}(\mathrm{d})$ is the main contributor

Distance	**Contribution $\dot{\mathbf{H}}_{\mathbf{p}_\gamma}(\mathbf{d})$**		**$\mathbf{d} \rightarrow \dot{\mathbf{H}}_{\mathbf{p}_\gamma}(\mathbf{d}) > 50\,\% \dot{\mathbf{H}}_{\mathbf{p}}(\mathbf{d})$**	
	RSD	**CLD**	**RSD**	**CLD**
1 m	4 - 64 %	5 - 70 %	9.1 - 17.1 cm	8.6 - 18.6 cm
5 m	5 - 65 %	9 - 75 %	8.1 - 17.7 cm	6.9 - 19.1 cm
10 m	6 - 73 %	11 - 82 %	7.6 - 18.7 cm	6.9 - 19.8 cm

Workers are not always facing the cask surface, but moving. Therefore, the angle between worker and cask is not always 0°. To study the influence of the position on $\dot{H}_p(d)$, simulations are performed for the 5 m position with the phantom at angles of 45°, and 90° with respect to the POLLUX® symmetry axis. Different angles between phantom and cask are shown in Figure 7.11.

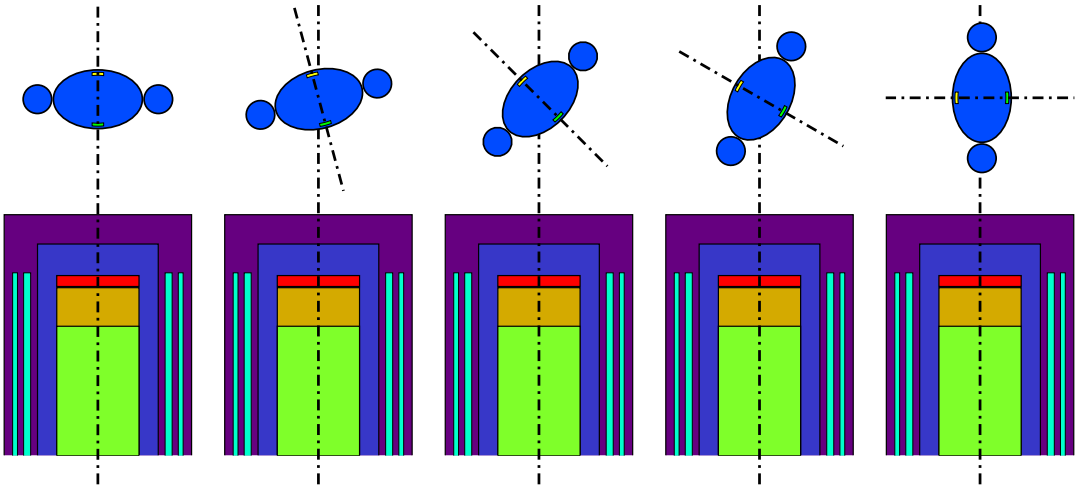

(a) 0° (b) 15° (c) 45° (d) 60° (e) 90°

FIGURE 7.11: Different angles of the phantom with respect to POLLUX®

Figure 7.12 shows the depth-dose curves at 45° and 90° for RSD which can be compared with the phantom facing the surface (0°) from Figure 7.10a. The depth-dose curves for CLD and FIA can be found in Appendix A. When rotating the phantom, the

depth-dose curve changes significantly, $\dot{H}_p(d)$ at the front of the phantom decreases with increasing angles, while $\dot{H}_p(d)$ at the back increases. The backscattered radiation plays a more significant role in $\dot{H}_p(10)$ when the angle increases. This effect can be explained by the decrease of the relative distance of the detector to the salt rock layer.

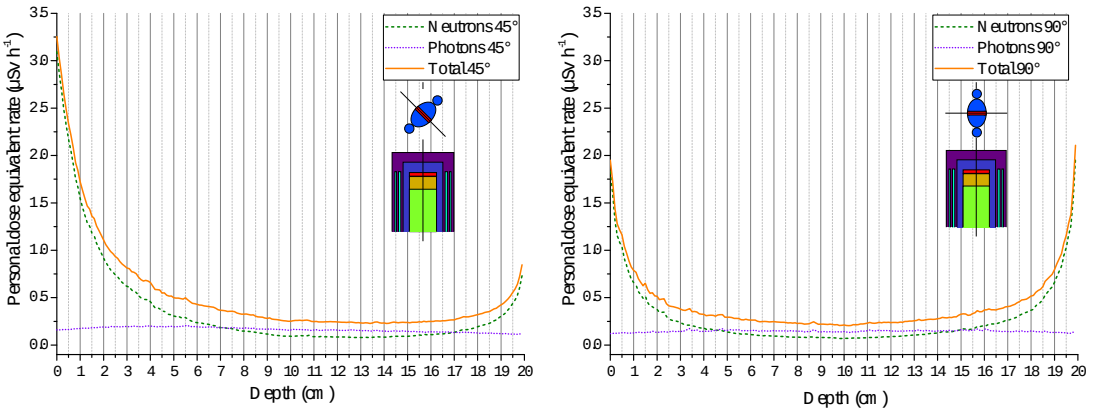

(a) Rock Salt Drift 45° (b) Rock Salt Drift 90°

FIGURE 7.12: Calculated evolution of $\dot{H}_p(d)$ for the body depth at 5 m to POLLUX-10 surface

Table 7.3 presents the contribution interval of the induced photons and the depth range where photon contribution exceeds the neutron contributions. The angle between phantom and cask has a very small influence in the contribution of $\dot{\mathrm{H}}_{\mathrm{p}_\gamma}(\mathrm{d})$. However, since the back side of the phantom receives a higher amount of neutrons and the induced photon production is constant it is reflected in Table 7.3 with a decrease of the maximum depth where $\dot{\mathrm{H}}_{\mathrm{p}_\gamma}(\mathrm{d})$ is the main contributor to the $\dot{H}_p(d)$ dose.

TABLE 7.3: Calculated photon contribution to $\dot{H}_p(d)$ and depths, where $\dot{\mathrm{H}}_{\mathrm{p}_\gamma}(\mathrm{d})$ is the main contributor.

Angle	**Contribution $\dot{\mathbf{H}}_{\mathbf{p}_\gamma}(\mathbf{d})$**		**$\mathbf{d \rightarrow \dot{H}_{p_\gamma}(d) > 50\,\% \dot{H}_p(d)}$**	
	RSD	**CLD**	**RSD**	**CLD**
0°	5 - 65 %	9 - 75 %	8.5 - 17.5 cm	6.9 - 19.1 cm
45°	5 - 66 %	10 - 72 %	7.4 - 16.9 cm	6.1 - 18.5 cm
90°	6 - 67 %	13 - 73 %	4.6 - 14.9 cm	3.3 - 15.9 cm

7.4.2 Options for a reliable personal dose prediction

As explained before, $\dot{H}_p(10)$ is supposed to provide a conservative estimate of the effective dose. However, as shown in the previous section, the presence of the drift increases the dose at the peripheral edges of the body. In order to study the influence of the backscattered radiation on the $\dot{H}_p(10)$ dose, two cylindrical detectors at a 10 mm depth (2 cm radius and 0.2 cm length) are modelled in the phantom (see Figure 7.3c):

one on the front side (representing a dosimeter worn in front of the chest) and another one on the back side (representing a dosimeter worn at the back side).

Five simulations with the phantom at angles of 0°, 15°, 45°, 60° and 90° with respect to POLLUX-10 symmetrical axis (see Figure 7.11) and at 5 m to its surface are performed in RSD to study the effect the orientation of the worker with respect to the shielding cask on $\dot{H}_p(10)$. For each simulation the sum of $\dot{H}_p(10)$ obtained with the front and back dosimeter is compared with the $\dot{H}_p(10)$ dose obtained with the front and back dosimeter, respectively, to check if the use of only one dosimeter may underestimate the total received dose. To reduce the calculation time, a geometry splitting (see section 3.2) is applied to the drift as shown in Figure 7.13. A total of 1×10^8 NPS are required to pass the MCNP6 statistical checks ensuring conformity.

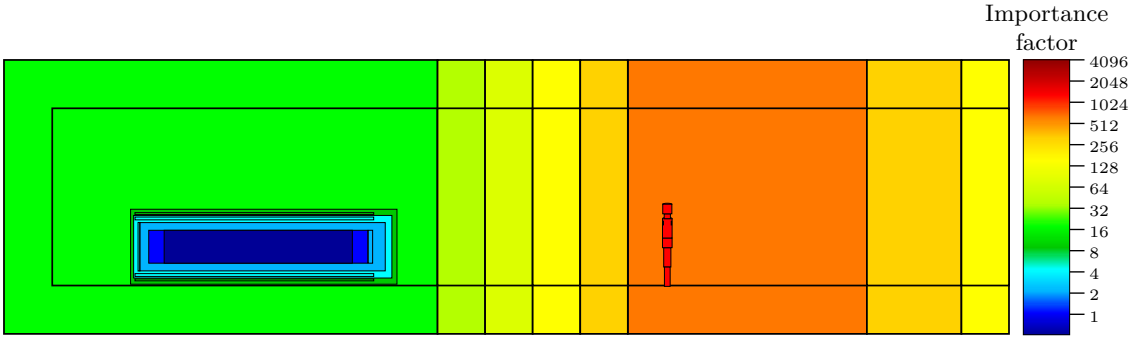

FIGURE 7.13: Phantom and cask inside the drift. The colours represent the increasing importance

Table 7.4 shows $\dot{H}_p(10)$ obtained with the detector at the chest ($\dot{\mathrm{H}}_\mathrm{p}(10)_\mathrm{Chest}$) and at the back ($\dot{\mathrm{H}}_\mathrm{p}(10)_\mathrm{Back}$) of the phantom (see Figure 7.3c). The sum of both detectors $\dot{\mathrm{H}}_\mathrm{p}(10)_\mathrm{Total}$ and the contribution of each detector to $\dot{\mathrm{H}}_\mathrm{p}(10)_\mathrm{Total}$ is also included in the table. At an angle of 0°, the frontal body part is facing the cask. Therefore, the main contribution to $\dot{\mathrm{H}}_\mathrm{p}(10)_\mathrm{Total}$ comes from the detector at the chest. However, as the angle between phantom and cask increases, the contribution of the detector at the back increases. When the phantom has a 90° angle with the cask this phenomenon reaches a maximum and the dose collected by each detector represents approximately 50 % of $\dot{\mathrm{H}}_\mathrm{p}(10)_\mathrm{Total}$.

If the worker wears only one dosimeter, only half of the dose will be registered when his orientation is at an angle of 90° in relation to the cask. But if the worker tuns for example to an angle of 180° only 14 % of the dose is recorded with one dosimeter at the chest. Hence, the combination of $\dot{\mathrm{H}}_\mathrm{p}(10)_\mathrm{Chest}$ and $\dot{\mathrm{H}}_\mathrm{p}(10)_\mathrm{Back}$ is a simple way to account for angular dependence and two dosimeters should be worn by the workers.

TABLE 7.4: Total $\dot{H}_p(10)$ and contribution of chest and back detectors for the different angles between phantom and POLLUX-10.

Angle	$\dot{\mathbf{H}}_\mathbf{p}(10)_{\mathbf{Total}}$ **µSv/h**	$\dot{\mathbf{H}}_\mathbf{p}(10)_{\mathbf{Chest}}$ **µSv/h**	$\%_{\dot{\mathbf{H}}_\mathbf{p}(10)_{\mathbf{Chest}}}$ **%**	$\dot{\mathbf{H}}_\mathbf{p}(10)_{\mathbf{Back}}$ **µSv/h**	$\%_{\dot{\mathbf{H}}_\mathbf{p}(10)_{\mathbf{Back}}}$ **%**
0°	1.4	1.2	86	0.19	14
15°	1.5	1.3	87	0.20	13
45°	1.2	0.97	82	0.22	18
60°	1.0	0.75	75	0.26	25
90°	0.89	0.45	50	0.44	50

7.5 Radiation exposure of employees during operation in disposal facilities

The above developed methodology, i.e. the simulation of two dosimeter in the body of a phantom to account for angular dependence, can be employed to estimate and assess the dose that workers receive in more complex scenarios, which correspond more realistically to an operational scenario in a disposal drift.

7.5.1 Description of the scenario

To apply the methodology, the disposal of a POLLUX® cask in the emplacement drift, which is based on the proposal of DBE-TECHNOLOGY GmbH (Filbert, Engelmann et al. 1995) has been selected as scenario. The MCNP6 models of four main working steps in the disposal procedure are shown in Figure 7.14. The geometrical description of the main components (Figure 7.14e) can be found in (Bollingerfehr, Filbert, Lerch et al. 2011). The disposal procedure is as follows: first the cask is transported on a carriage through the drift with an electric locomotive with a driver sitting inside the cabin (Figure 7.14a). Once it arrives to the disposal position, as shown in Figure 7.14b, the cask is slowly positioned under a storage equipment which elevates the cask from the carriage to allow locomotive and carriage to drive back. Once the locomotive and carriage are driven back, the storage equipment places the cask on the ground (Figure 7.14c). Finally, as shown in Figure 7.14d, the locomotive moves the storage equipment to the next disposal position where the steps will be carried on again until the drift is full.

The above described steps are simulated for the disposal of POLLUX-10, POLLUX-3M and POLLUX-3U cask since they have the same geometry. To compare the radiation exposure, the same or a similar amount of SNF are disposed in both emplacement drifts, i.e one POLLUX-10 cask in RSD (5.45 t HM) and three casks in CLD (one POLLUX-3M

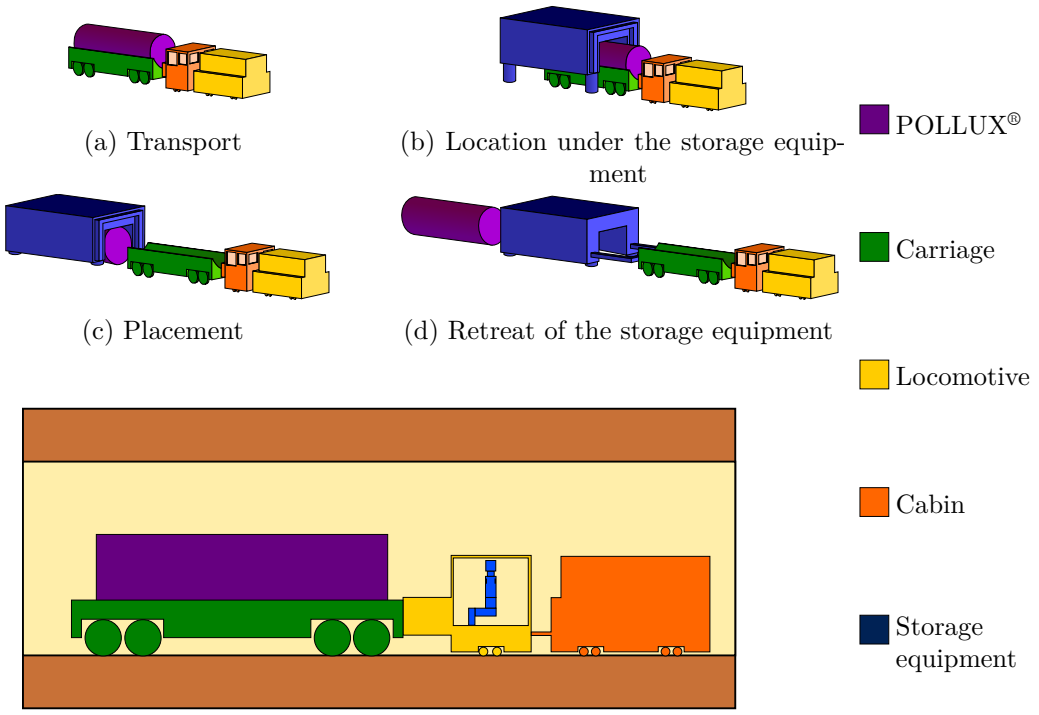

(a) Transport

(b) Location under the storage equipment

(c) Placement

(d) Retreat of the storage equipment

(e) Components of the locomotive system

FIGURE 7.14: MCNP6 model of four steps for a POLLUX® disposal scenario.

and two POLLUX-3U, in total 4.92 t HM). As relevant parameter the $\dot{H}_p(10)$ dose in µSv/h is employed to compare the radiation exposure in the different working steps, which are considered to be the same for the disposal of POLLUX-10, POLLUX-3M and POLLUX-3U.

The driver sitting inside the cabin, represented by the BOMAB phantom, stays the entire time inside the cabin and faces the shielding cask. Therefore, the angle between phantom and cask is always 0°. However, the amount of backscattered radiation may be further increased due to the reflection at the cabin walls. To perform the MCNP6 simulations, geometry splitting is used in the drift and inside the locomotive cabin to reduce the number of transported particles (see Figure 7.15). To pass the MCNP6 statistical checks, 4×10^8 NPS are required for transport and location under the storage equipment simulations. For placement and retreat of the storage equipment 1.5×10^9 NPS are required, since the distance between cask and phantom is larger.

7.5.2 Comparison of the personal dose rate in the rock salt and clay drifts during a typical working scenario

Table 7.5 shows for the different working steps of the disposal scenario shown in Figure 7.14 the calculated dose at the front of the chest, at the back and the sum of

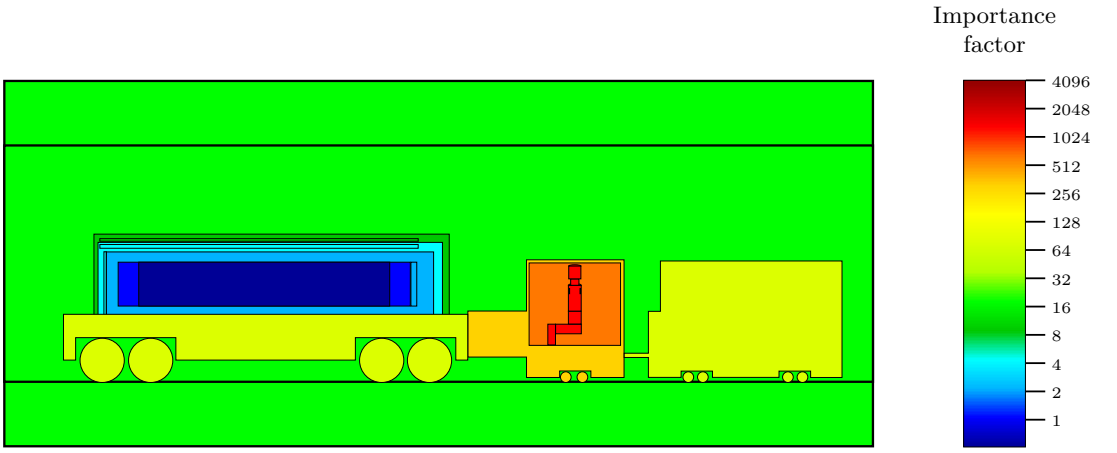

FIGURE 7.15: MCNP6 model of the different components of the transport train and geometrical splitting example.

both, while $\%_{\text{Chest}}$ and $\%_{\text{Back}}$ are the chest and back percentage contribution to total $\dot{\text{H}}_{\text{p}}(10)$, respectively. In the table, POLLUX-10 refers to the calculated $\dot{H}_p(10)$ for each working step of the disposal in a RSD, while POLLUX-3 refers to the sum of the calculated $\dot{H}_p(10)$ for two POLLUX-3U and one POLLUX-3M .

Since the angle between phantom and source is always 0°, the main contribution to $\dot{\text{H}}_{\text{p}}(10)$ originates from the chest detector. However, comparing with the results at 0° given in Table 7.4, the contribution of the back dosimeter to $\dot{\text{H}}_{\text{p}}(10)$ for the worker inside the cabin is higher than that for the worker standing in the drift. This effect is attributed to additional backscattered radiation due to the cabin walls and locomotive elements made of steel.

For an easier interpretation of the results Figure 7.16 shows a graphic comparison of $\dot{\text{H}}_{\text{p}}(10)$ for POLLUX-10, POLLUX-3M and POLLUX-3U, as well as for the total in the clay scenario (POLLUX-3). The calculated dose for each step is similar for POLLUX-3M and for POLLUX-10, while that for POLLUX-3U is 70 % lower that for POLLUX-3M, since no spent MOX fuel is stored in POLLUX-3U. However, to dispose the same amount of waste as in a POLLUX-10, one POLLUX-3M and two POLLUX-3U have to be employed. Therefore, $\dot{\text{H}}_{\text{p}}(10)_{\text{Total}}$ is 35 % higher for the disposal in CLD that in RSD. This confirms that the selection of the host rock plays an important role in the radiation exposure of workers in such facilities since it restricts the amount of SNF disposed in each cask which determinates the personal dose rate.

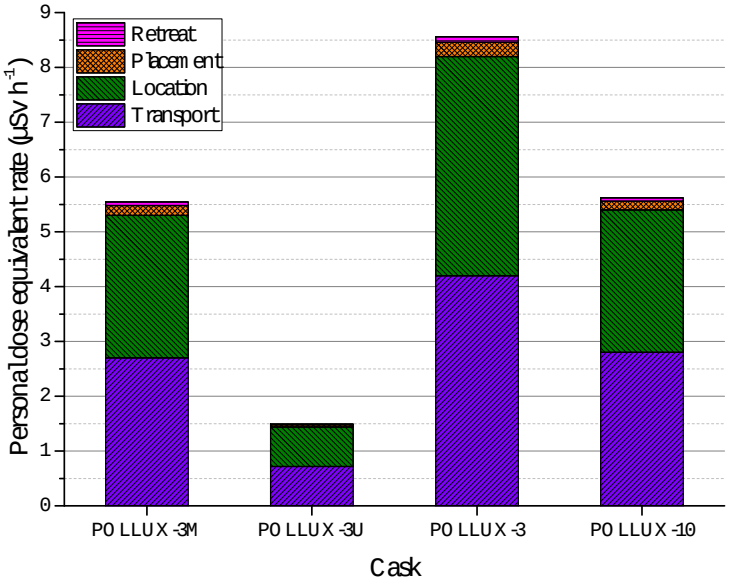

FIGURE 7.16: Calculated total $\dot{H}_p(10)$ dose for the different casks

TABLE 7.5: Total $\dot{H}_p(10)$ and the contribution of the chest and back detectors for the different disposal steps in RSD and CLD.

Step	Cask	Total µSv/h	Chest µSv/h	$\%_{Chest}$ %	Back µSv/h	$\%_{Back}$ %
Transport	**POLLUX-3M**	2.7	2.4	87	0.35	13
	POLLUX-3U	0.72	0.63	88	0.086	12
	POLLUX-3	4.2	3.7	88	0.52	12
	POLLUX-10	2.8	2.3	83	0.49	17
Location	**POLLUX-3M**	2.6	2.2	85	0.38	15
	POLLUX-3U	0.72	0.63	87	0.092	13
	POLLUX-3	4.0	3.5	86	0.57	14
	POLLUX-10	2.6	2.1	80	0.50	20
Placement	**POLLUX-3M**	0.18	0.15	86	0.025	14
	POLLUX-3U	0.038	0.032	85	0.0059	15
	POLLUX-3	0.26	0.22	86	0.037	14
	POLLUX-10	0.19	0.16	82	0.034	18
Retreat	**POLLUX-3M**	0.068	0.050	73	0.018	27
	POLLUX-3U	0.017	0.015	85	0.0026	15
	POLLUX-3	0.10	0.080	77	0.023	23
	POLLUX-10	0.062	0.054	88	0.0073	12

7.6 Concluding remarks for operation in a waste disposal facility

The developed methodology can be applied to assess the exposure during the different steps of nuclear waste disposal. In this work the same geometrical parameter are considered for both emplacement drifts. However, due to the lower loading capacity of the cask in CLD, a larger disposal space is required, resulting in a larger repository compared to a repository in RSD (e.g. DBE-Tec (2016)). This leads to a longer transport distance and also longer exposure durations. Since the transport of the cask is one of the steps with the highest personal dose rate, it is plausible to assume that the total personal exposure for disposal in a drift with a concrete lining (claystone or crystalline) is higher than for a disposal in a drift in rock salt.

Since a precise description of the duration of each working step is still unknown only a dose rate comparison is possible. The following example tries to demonstrate the importance of this description. Let's assume that 5 h are required to dispose a POLLUX-10, where 4 h are headed for transport (to simplify, only transport in a drift is considered) and the last hour is equally divided amongst the other three steps (20 min /step). For the disposal in CLD the transport of each cask takes longer since the needed space within the drift is larger (let's assume 7 h). This leads to a dose of about 12 µSv and 27 µSv for RSD and CLD, respectively. However as more and more casks are disposed in the drift, the transport time is reduced. Assuming that only 1 h is required for the transport when the drift is almost full and that the contribution of the disposed casks is negligible du to the distance. Since the time for the other three steps is the same, it leads to a dose of about 4 µSv and 6 µSv for RSD and CLD, respectively.

As illustrated in the example above, the duration of the working steps (especially the transport) plays a decisive role in the personal dose and the total collective dose in the disposal facility. Therefore, a precise description of the different steps is necessary to perform a proper comparison between the different disposal options and to provide recommendations for minimizing the occupational radiation exposure.

Chapter 8

Summary and Outlook

8.1 Summary

In this work, a methodology to assess and compare the received person dose during the disposal of high-level nuclear waste by means of the Monte-Carlo method is developed. As a representative example, the mixed neutron-gamma radiation field of a POLLUX® cask with spent UOX / MOX fuel in a deep geological repository has been selected. Two different host rocks, rock salt (RSD) and claystone with a concrete lining (CLD) are chosen to compare the radiation field and the personal dose in the disposal drift. To compare similar amounts of SNF, a POLLUX-10 is placed in RSD, while for CLD a POLLUX-3M and two POLLUX-3U are disposed. In addition, casks free in air FIA are complementary investigated.

To study the radiation field, the quantity $\dot{H}^*(10)$is used as relevant indicator. Results show that for the selected waste inventory, neutrons are the main contributors to the radiation dose field. The backscattered radiation of the host rock layers or the concrete lining increases $\dot{H}^*(10)$ in the disposal drift in comparison with a cask FIA. If the same cask is disposed in RSD and CLD a higher $\dot{H}^*(10)$ is observed in RSD. This difference is caused by the neutron reflection of the rock salt layers which returns neutrons back to the gallery, while in the claystone drift the presence of oxygen in the concrete lining moderates the neutrons resulting in a lower increase of $\dot{H}^*(10)$.

To study the absorbed dose, the quantity $\dot{H}_p(10)$ is selected since it is supposed to provide a conservative estimate of the effective dose. A mathematical phantom with two detectors, one at the front side of the chest and another one at the back side representing two dosimeters, has been modelled. Calculations with different angles between the phantom and the cask show that there is an angular dependence of the registered dose

rate values. This effect is enhanced if the dose rate is obtained with only one dosimeter. Therefore, a realistic personal dose rate in such an environment requires the use of two dosimeters.

The above described methodology is applied to the working scenario for the disposal of a POLLUX® cask in an emplacement drift (operational application). The results of the investigated scenario, where the worker is sitting inside the locomotive cabin and always facing the cask, show that the main contribution to $\dot{H}_p(10)$ is registered from the front detector. However, due to the additional neutron scatterings at the cabin, the contribution of the back detector to $\dot{H}_p(10)$ is higher than with the worker just standing alone in the drift. The calculated personal dose rate for each working step is similar for POLLUX-3M and for POLLUX-10 while for POLLUX-3U it is much lower since no MOX is disposed in the cask. However, to dispose the same amount of waste as in the RSD, three casks have to be placed in the CLD. Therefore, each disposal step has to be carried out three times (one POLLUX-3M and two POLLUX-3U), which finally leads to a higher $\dot{H}_p(10)$ dose for the workers in the CLD disposal case.

To verify the developed methodology, a laboratory and a numerical approach are conducted to elaborate the accuracy threshold of the results obtained with the simulations. In the laboratory approach, experiments are performed at the TUD-NG. The D+D fusion reaction is used to generate 2.5 MeV neutrons since this energy is close to the average energy range of neutrons in shielding casks loaded with SNF. To measure the spectra, a NE-213 detector is taken since it is able to measure both fast neutrons and gamma rays. Different configurations of layers of steel and polyethylene between the target of the generator and the detector are analysed to mimic the typical structure of a shielding cask. Corresponding simulations with MCNP6 have been conducted.

The measurement results show that an important part of the 2.5 MeV emitted neutrons undergo an inelastic scattering with the iron and copper present around the neutron target, which implies the appearance of a second peak in the neutron spectra around 1.7 MeV corresponding to the energy of the scattered neutrons. The experimental and simulated neutron spectra are in good agreement within the measurement accuracy window. MCNP6 is able to reproduce both neutron peaks with a difference lower than 10 %, which is attributed to the uncertainties in the detector response and unfolding procedure. The measured gamma ray spectra are in concordance with the gamma ray lines expected according to the main excitation states of iron and copper stemming from $(\mathrm{n}, \mathrm{n}'\gamma)$ reactions. The low energy resolution of the NE-213 detector for gamma rays does not allow to observe clear peaks for the different gamma rays. Instead, a curve including many of them has been observed with an average difference of 60 % with the measurements. However, taking in account these limitations, results show that the use

of a neutron generator is suitable to assess simulation scenarios with shielding casks containing spent nuclear fuel.

To analyse the impact of the nuclear cross section uncertainties, the software package SCALE is used. Simulations with random perturbations on the ENDF nuclear cross section libraries are performed for a POLLUX® cask in vacuum with respect to the $\dot{H}^*(10)$ dose. Although the current version of SCALE provides not much information about how the cross sections are perturbed, the results show that the perturbations have a measurable influence on $\dot{H}^*(10)$ dose. Nevertheless, the influence is marginal compared to the other effects to be neglected in further computation dose.

A comparison between $\dot{H}^*(10)$ dose obtained with SCALE and MCNP6 for a POLLUX® cask in vacuum exhibits minor differences which are attributed to the physics of the employed tally and the different cross section libraries. Nevertheless, the differences are small enough to affirm that both codes give similar results for the calculated problem. Hence, MCNP6 is preferred since it offers some advantages like lower calculation time, a more intuitive input and a higher diversity of tallies that make it better to perform complicate Monte-Carlo problems.

The experimental and numerical approach confirmed that the interval of confidence of the employed code is small enough to consider the results obtained in this study as validated in an engineering sense. Therefore, the developed methodology exhibits very promising prospects to perform dose predictions for operational procedures in nuclear waste disposal facilities as they may be required by licensing authorities.

8.2 Outlook

Based on the methods and tools presented in this work, further calculations and measurements could be performed in the future. Although this work already verifies and engineering validates that the developed methodology is consistent and can be applied to the dose assessment in disposal facilities, some aspects still require improvements.

First, the sensitivity analysis performed with SCALE shows that the perturbations on the cross sections have an influence on the calculated dose. Even if it has been found that the influence is small enough to be neglected, the current version of SCALE does no allow to study which cross section perturbations have a higher influence in these results. A new version of SCALE is expected to be released in 2018. According to the developers, this version will allow to select cross sections of isotopes to perform specific perturbations. The calculations performed with SCALE in this work could be repeated once the new version is available to complete the sensitivity study. This study will allow

to explain why in some isolated cases the difference with the unperturbed values are higher than 50 %.

Second, the precision of the MCNP6 code to simulate neutron induced photons in the experiments with the TUD-NG is only partially demonstrated since the employed NE-213 detector has not enough energy resolution to observe clear gamma ray peaks. A possible approach to enhance this comparison is the use of a Germanium detector to measure the gamma rays since it has a much higher gamma ray resolution. Although this results do not affect directly the present work, since the radiation field is dominated by neutrons, it will be decisive for the study of other scenarios where the contribution of the gamma energies play a more important role.

Finally, the results of this work shown that the position and orientation of the worker relative to the radiation source play an important role in the calculated/measured dose. Therefore, a study of the effective dose under this irradiation conditions should be performed to verify if the $\dot{H}_p(d)$ is still a conservative assessment. In the affirmative case the question arises if $\dot{H}_p(10)$ is the adequate assessment. According to the newest ICRP recommendation, the eye lens dose ($H_p(3)$) limit is now at the same level than the one from $H_p(10)$ at 20 mSv/yr. In this work $\dot{H}_p(10)$ has been employed in view of the old $H_p(3)$ limit of 20 mSv/yr. However, simulations with a modification on the phantom to measure $\dot{H}_p(3)$ should be repeated to check if the obtained values are under the dose limits. The final goal must be however, to simulate the 3-D dose distribution in the entire body.

For the characterization of the radiation field and the absorbed dose, only neutrons coming from the SNF and neutron induced photons in the worker body are considered. Although this is true for the selected nuclear waste inventory, for inventories with other cooling times or compositions this may be different. Since the disposed waste is expected to stay several hundreds to thousands of years, a study for other time periods must be performed to determine if the conclusions obtained in this work may be extrapolated to longer time scales, which is of interest to perform occupational radiation exposure simulations for workers involved in retrieval scenarios. However, the employed methodology, i.e. the use of two dosimeters one at the chest and one at the back, is supposed to be similar as described here.

In this work only the deep geological disposal in rock salt and claystone are compared assuming that the working steps are similar. However, to perform a proper comparison between different disposal options, a precise description of the boundary conditions, i.e. exact geometry of the disposal drift, duration of the different working steps, etc. which is still not available but is necessary to provide recommendations for minimizing the occupational radiation exposure.

This work focused on the deep geological disposal of nuclear waste. However, there are other scenarios like the long-term above-ground storage or nuclear power plants where workers are also exposed to neutron-gamma radiation fields. In these scenarios it is also of interest to apply Monte-Carlo methods to a reliable and predictive in advance planning phase to estimate the personal dose of occupational exposure. However, since these scenarios do not have the same boundary conditions as the ones described in this work, the steps followed in the developed methodology, i.e. definition of the source terms, study of boundary factors impacting on the dose rate and study of the radiologically weighted absorbed dose, have to be repeated to verify if the recommendations of this work, i.e. considering only the main emission source and backscattering and employing two dosimeters to assess the dose, can be applied.

Appendix A

Extra calculations performed with MCNP6 and SCALE

A.1 Calculations with SAMPLER for POLLUX-10

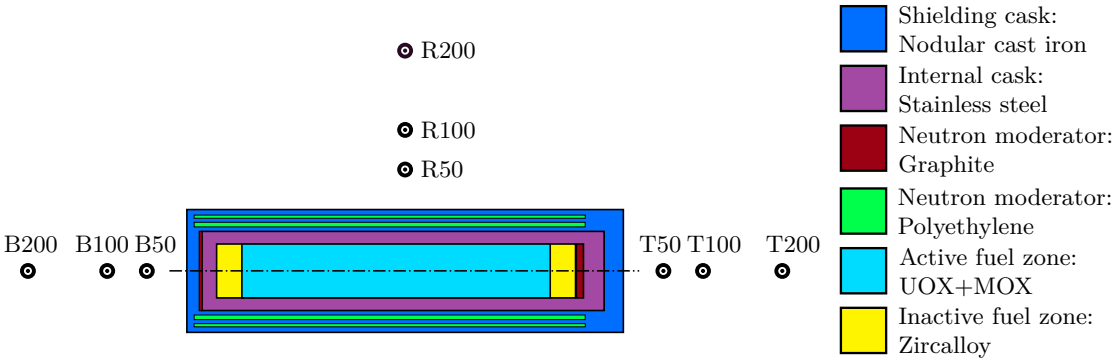

FIGURE A.1: SCALE model of a POLLUX-10 cask and position of the dose detectors.

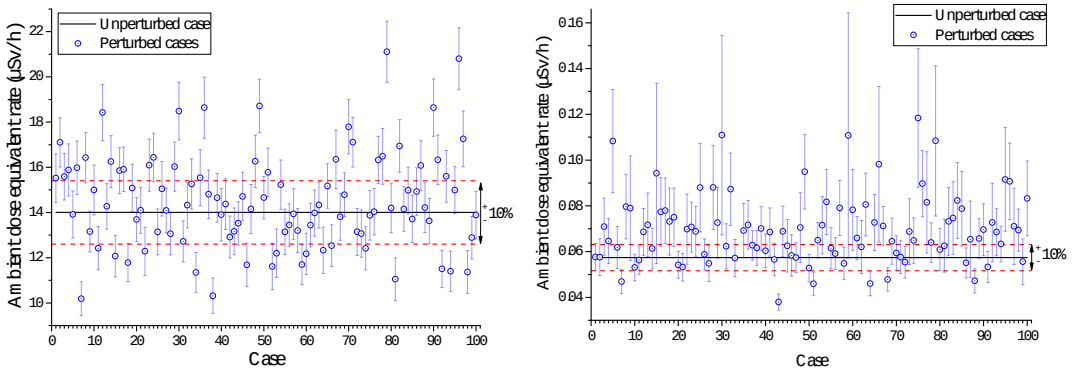

(a) Neutrons

(b) Neutron induced photons

FIGURE A.2: Calculated $\dot{H}^*(10)$ dose at position T50 for the 100 cases by SAMPLER.

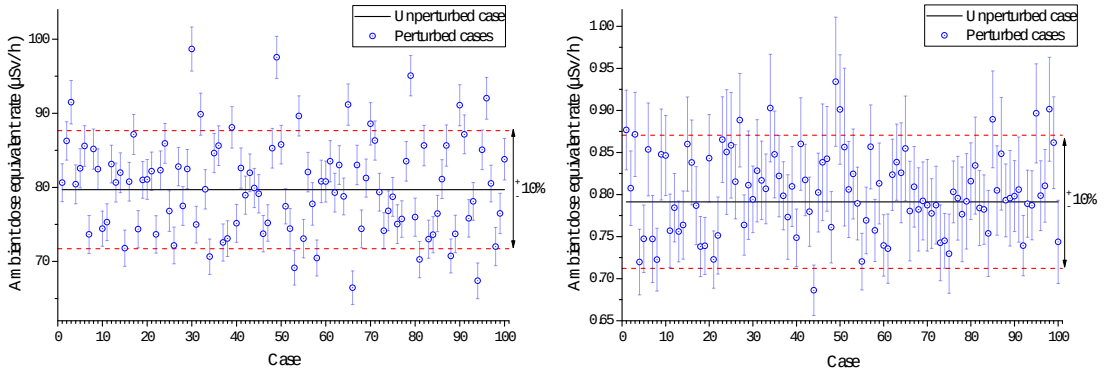

(a) Neutrons (b) Neutron induced photons

FIGURE A.3: Calculated $\dot{H}^*(10)$ dose at position B50 for the 100 cases by SAMPLER.

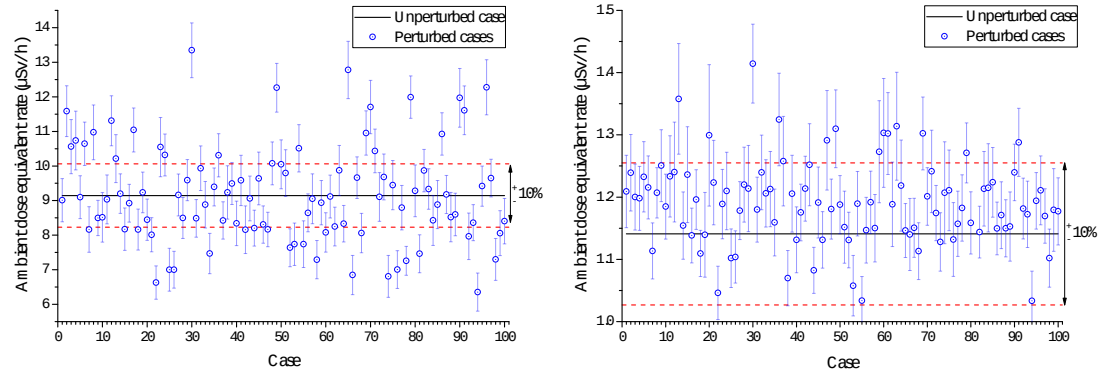

(a) Neutrons (b) Neutron induced photons

FIGURE A.4: Calculated $\dot{H}^*(10)$ dose at position R50 for the 100 cases by SAMPLER.

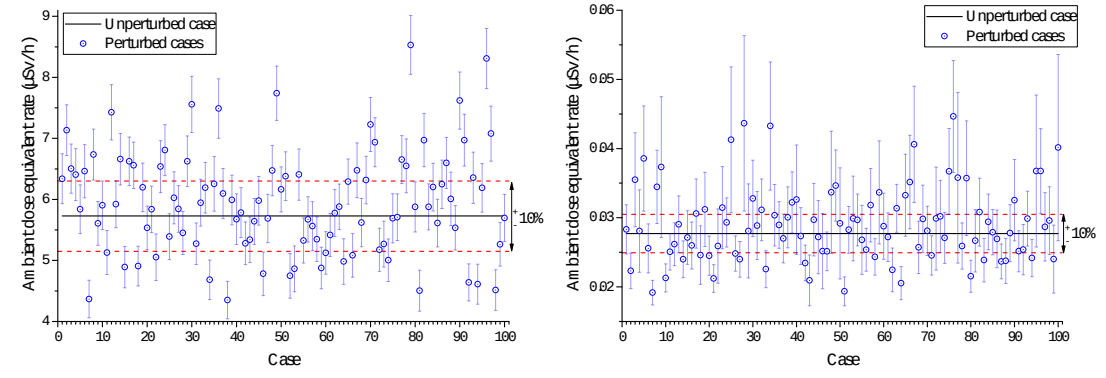

(a) Neutrons (b) Neutron induced photons

FIGURE A.5: Calculated $\dot{H}^*(10)$ dose at position T100 for the 100 cases by SAMPLER.

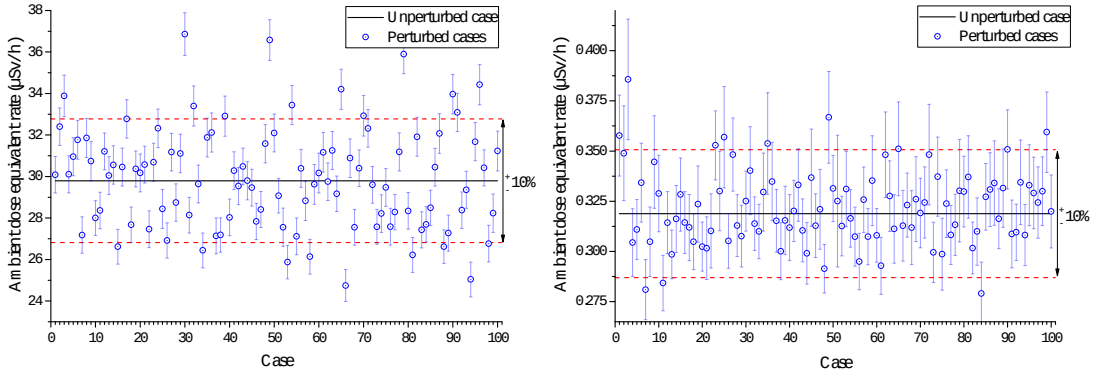

(a) Neutrons (b) Neutron induced photons

FIGURE A.6: Calculated $\dot{H}^*(10)$ dose at position B100 for the 100 cases by SAMPLER.

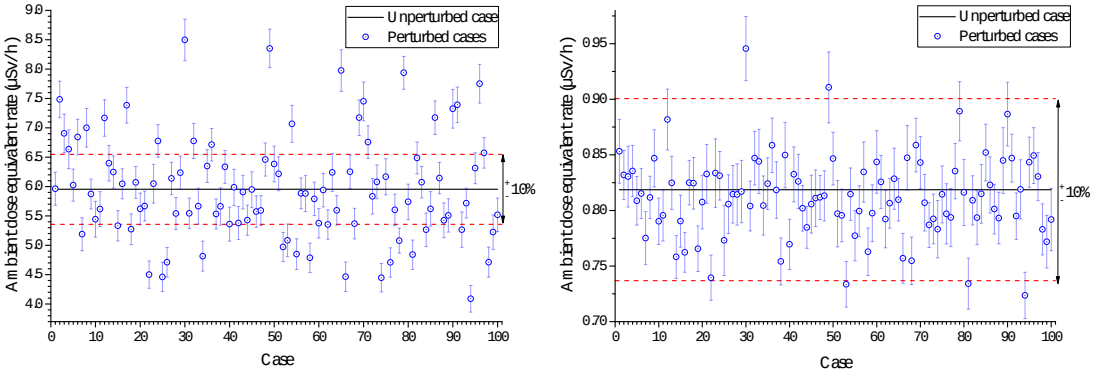

(a) Neutrons (b) Neutron induced photons

FIGURE A.7: Calculated $\dot{H}^*(10)$ dose at position R100 for the 100 cases by SAMPLER.

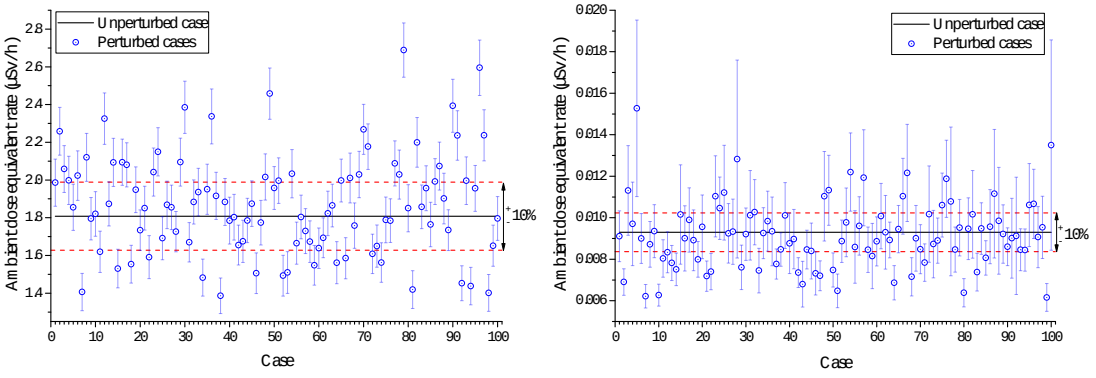

(a) Neutrons (b) Neutron induced photons

FIGURE A.8: Calculated $\dot{H}^*(10)$ dose at position T200 for the 100 cases by SAMPLER.

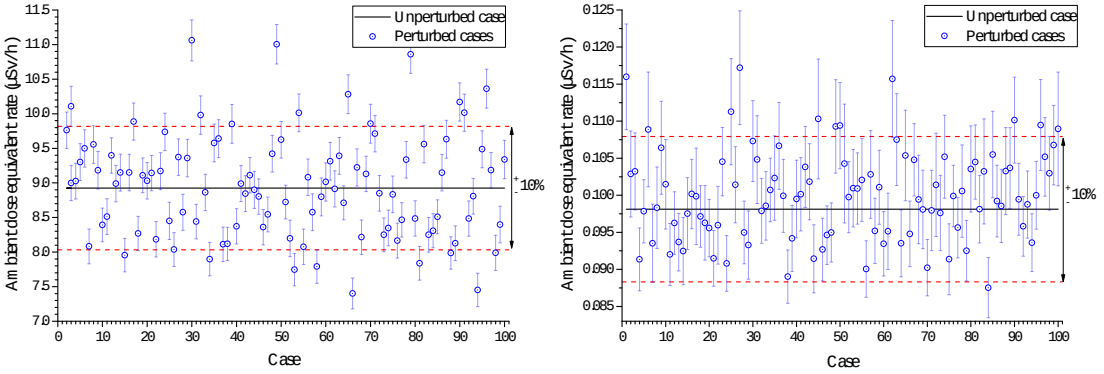

(a) Neutrons (b) Neutron induced photons

FIGURE A.9: Calculated $\dot{H}^*(10)$ dose at position B200 for the 100 cases by SAMPLER.

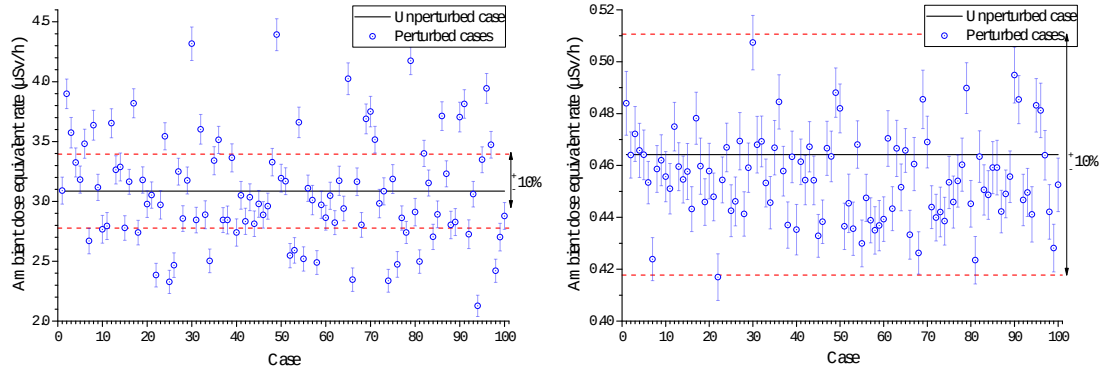

(a) Neutrons (b) Neutron induced photons

FIGURE A.10: Calculated $\dot{H}^*(10)$ dose at position R200 for the 100 cases by SAMPLER.

A.2 Contribution of the different radiation types to the POLLUX® emission

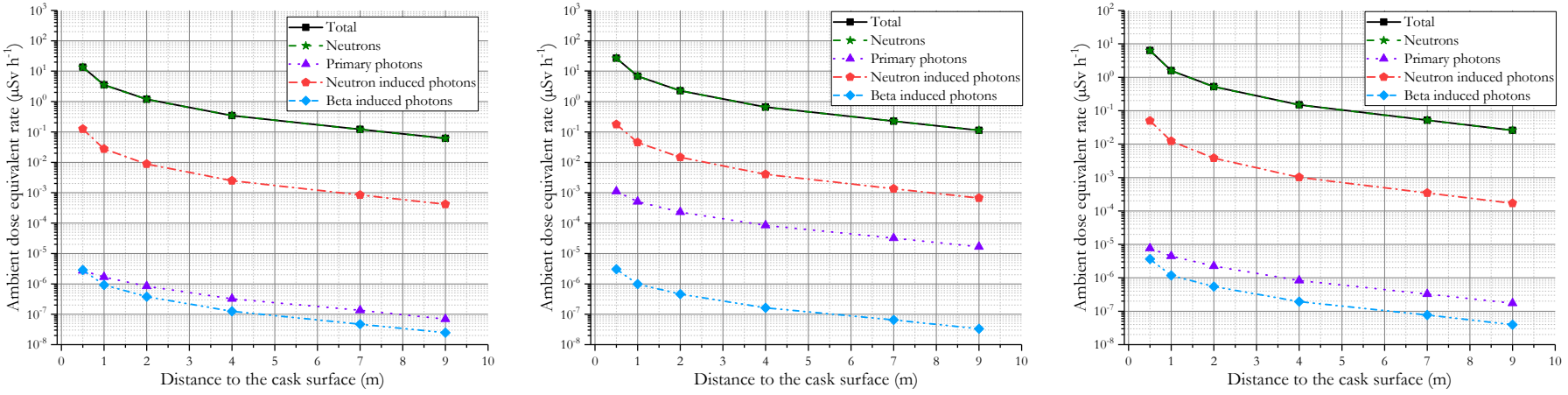

(a) POLLUX-10 (b) POLLUX-3M (c) POLLUX-3U

FIGURE A.11: Calculated contribution of different radiation to $\dot{H}^*(10)$ dose at the top of the POLLUX® in vacuum.

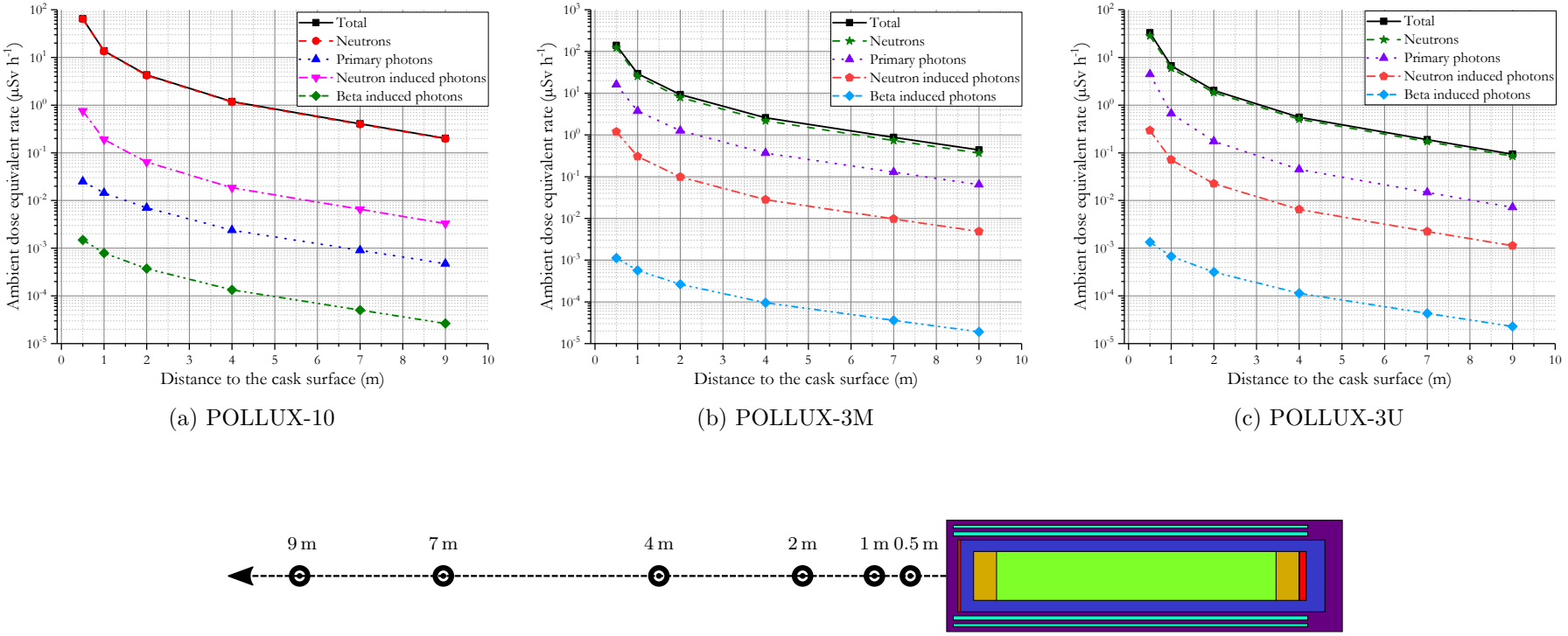

(a) POLLUX-10 (b) POLLUX-3M (c) POLLUX-3U

FIGURE A.12: Calculated contribution of different radiation to $\dot{H}^*(10)$ dose at the bottom of the POLLUX® in vacuum.

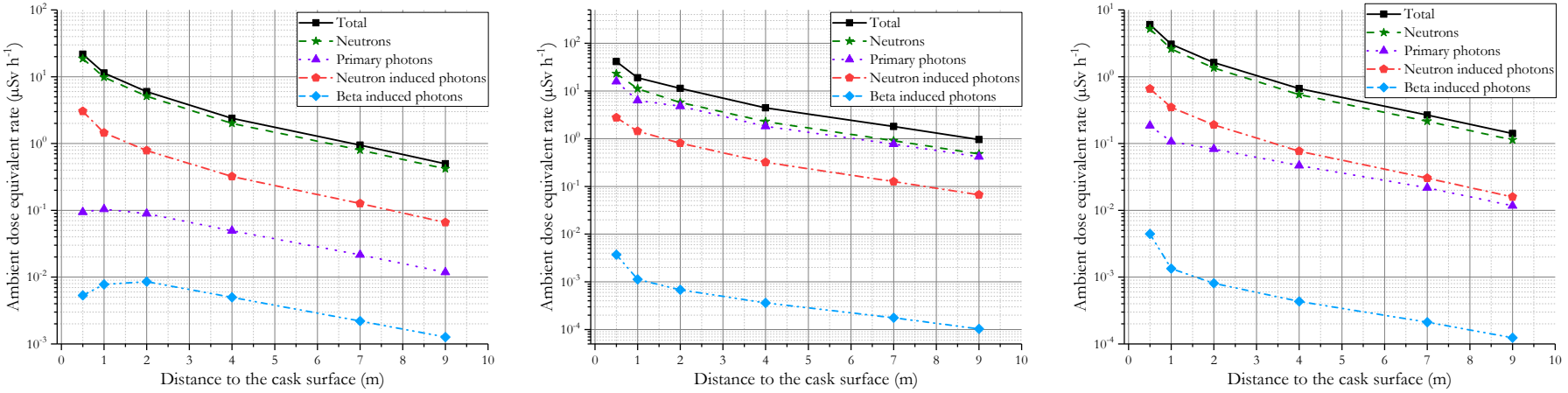

(a) POLLUX-10 (b) POLLUX-3M (c) POLLUX-3U

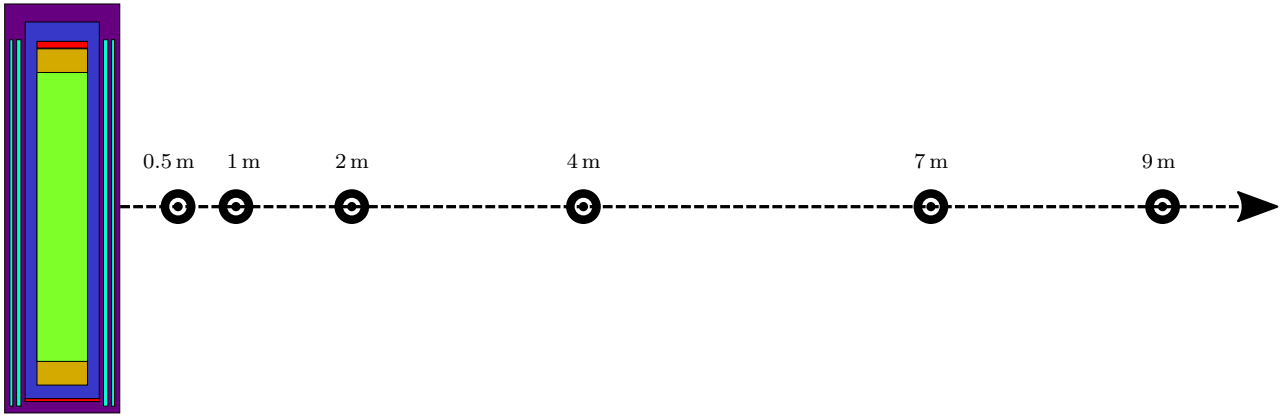

FIGURE A.13: Calculated contribution of different radiation to $\dot{H}^*(10)$ dose at the lateral of the POLLUX® in vacuum.

A.3 Dependence of host rock conditions on $\dot{H}^*(10)$

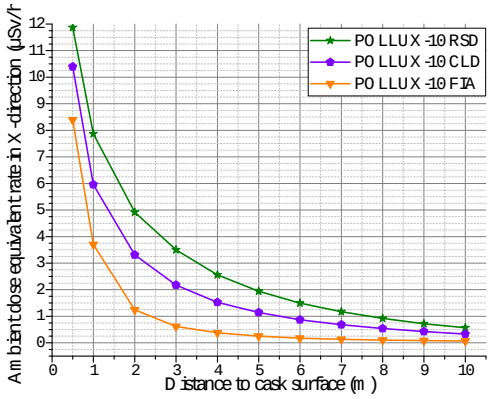

(a) Neutrons POLLUX-10

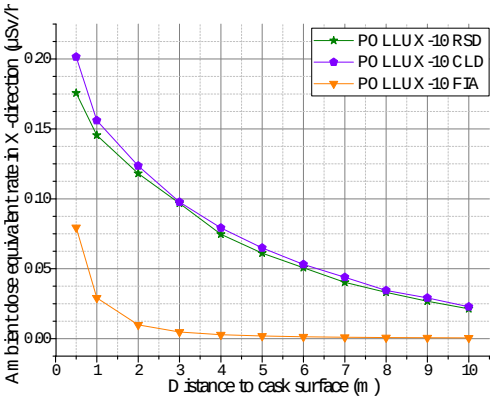

(b) Neutron induced photons POLLUX-10

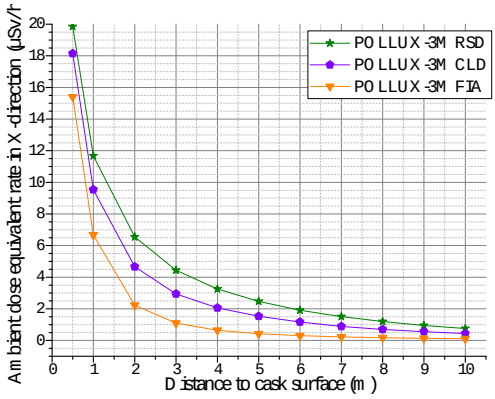

(c) Neutrons POLLUX-3M

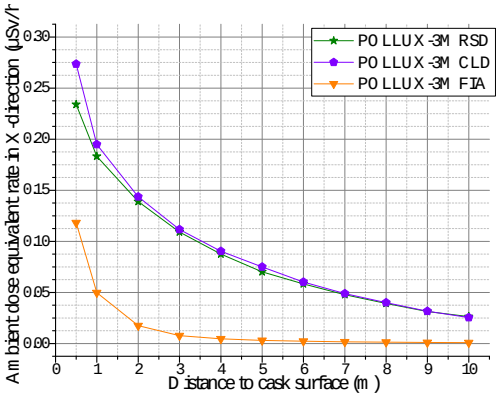

(d) Neutron induced photons POLLUX-3M

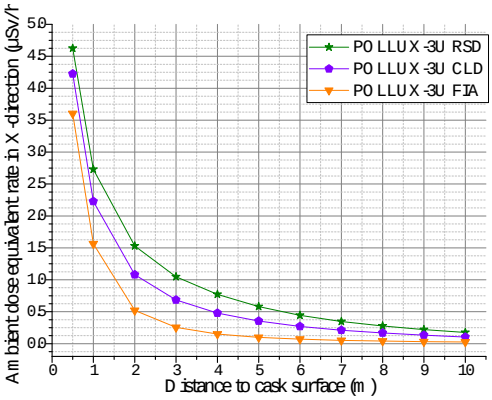

(e) Neutrons POLLUX-3U

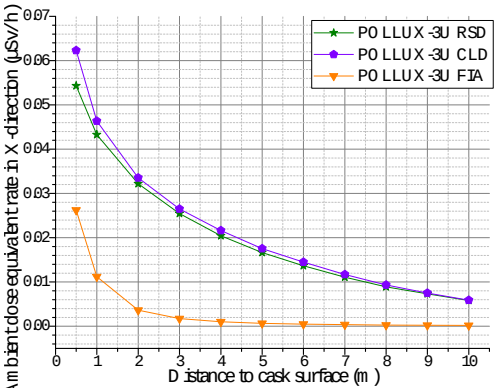

(f) Neutron induced photons POLLUX-3U

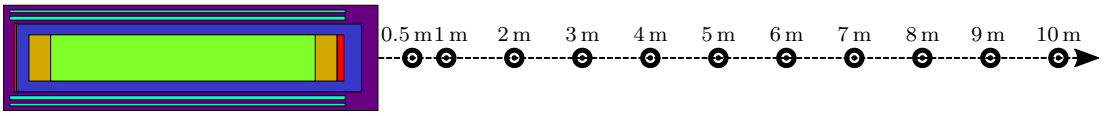

FIGURE A.14: Calculated distance dependence of $\dot{H}^*(10)$ dose for three different drift layers in the X-direction.

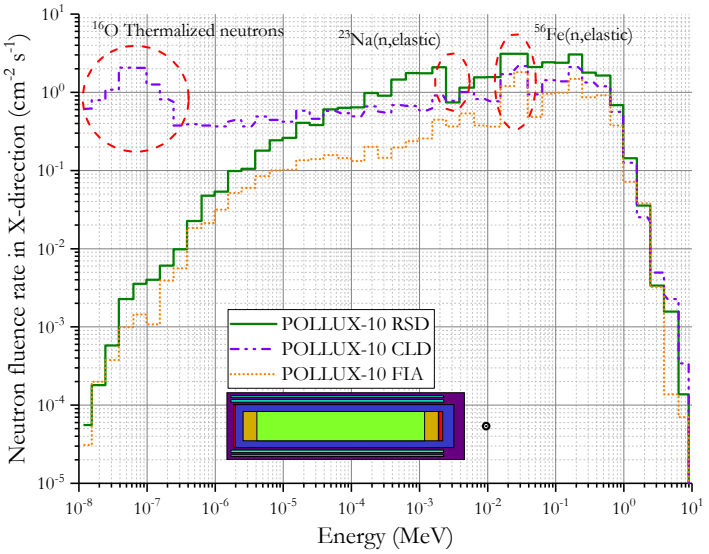

(a) POLLUX-10

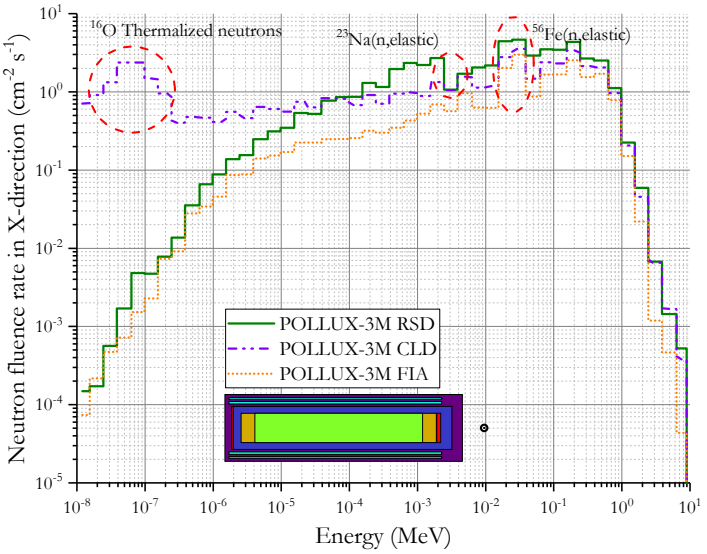

(b) POLLUX-3M

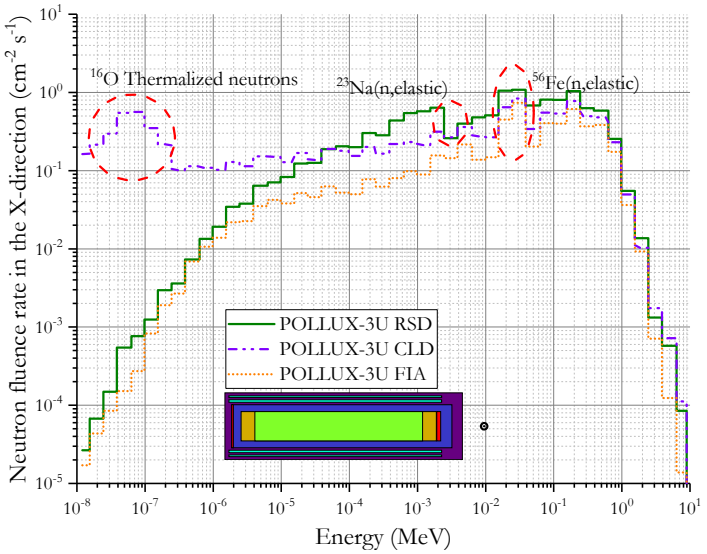

(c) POLLUX-3U

FIGURE A.15: Calculated spectral neutron fluence rate at 1 m distance from cask surface for different host rocks.

A.4 Spatial dependence of absorbed dose from the source

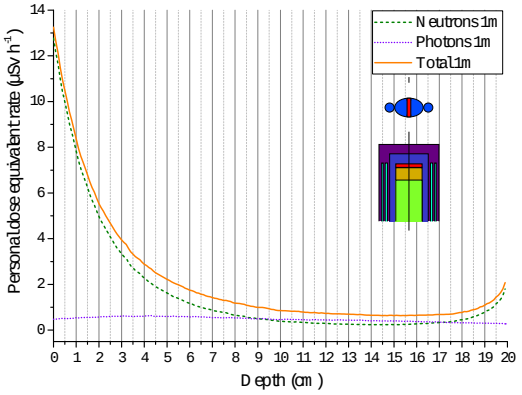

(a) Rock Salt Drift 1 m to cask surface

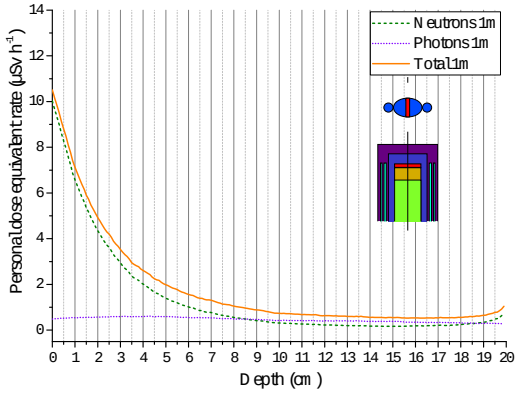

(b) Concrete Lining Drift 1 m to cask surface

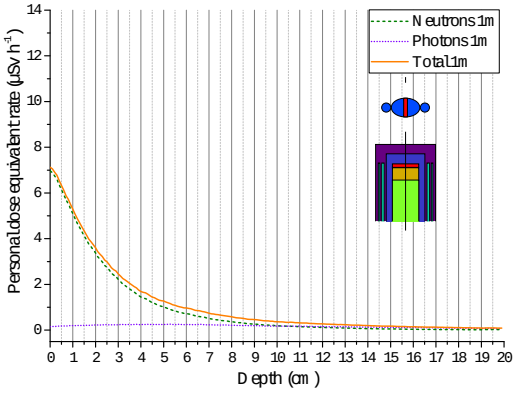

(c) Free In Air 1 m to cask surface

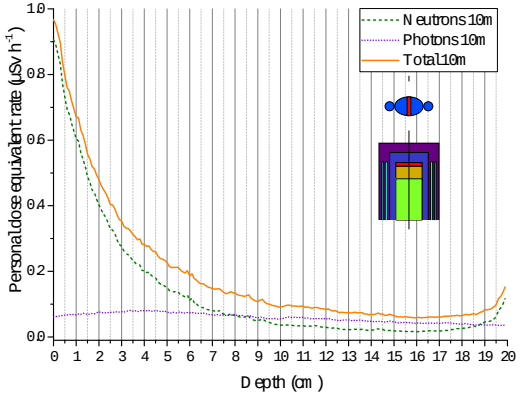

(d) Rock Salt Drift 10 m to cask surface

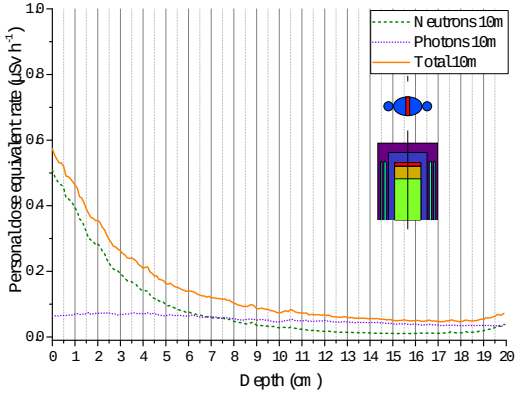

(e) Concrete Lining Drift 10 m to cask surface

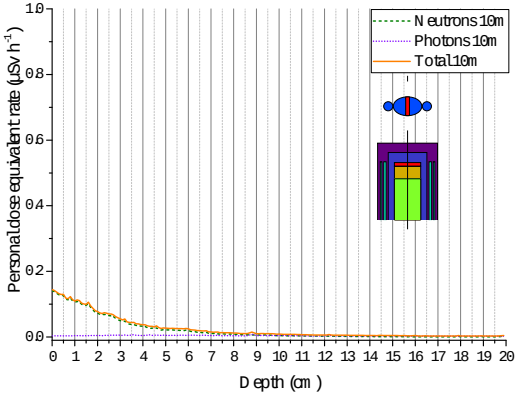

(f) Free In Air 10 m to cask surface

FIGURE A.16: Calculated evolution of $\dot{H}_p(d)$ dose with depth for a phantom facing the POLLUX-10 to its surface.

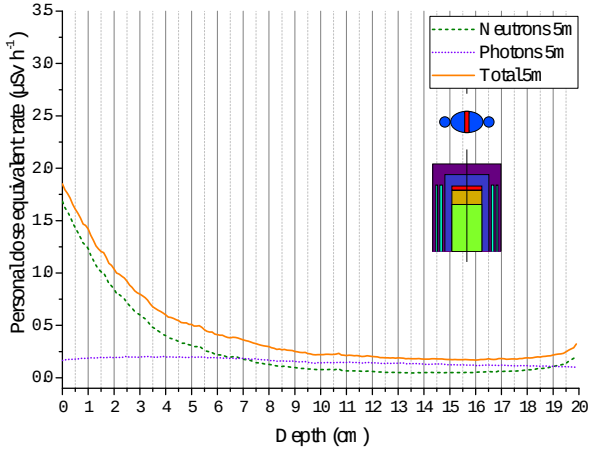

(a) Concrete Lining Drift 0°

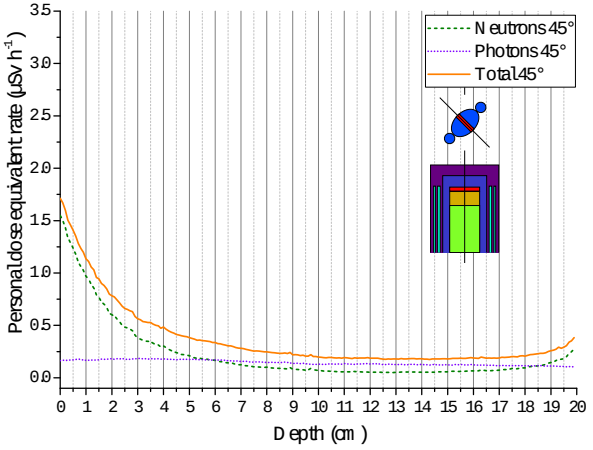

(b) Concrete Lining Drift 45°

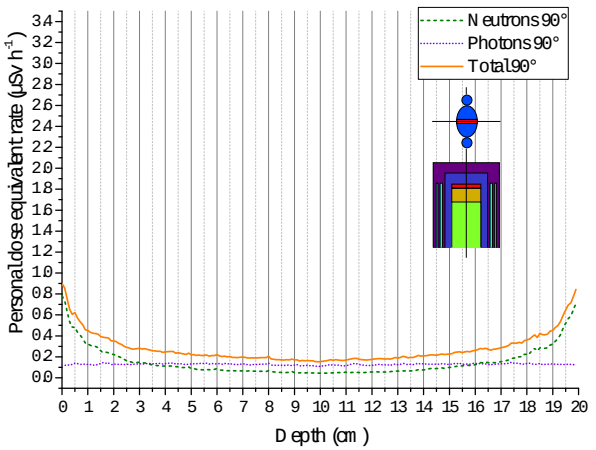

(c) Concrete Lining Drift 90°

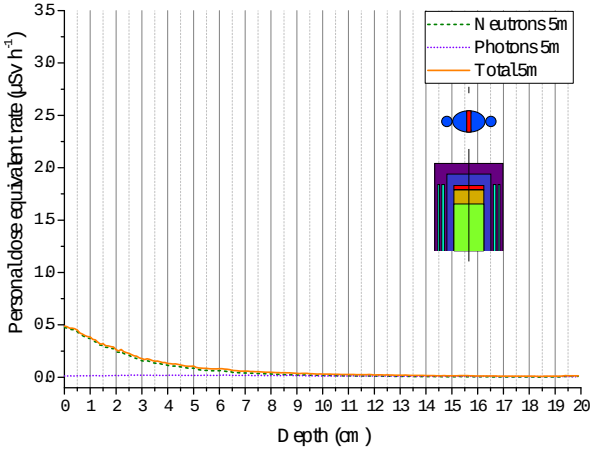

(d) Free In Air 0°

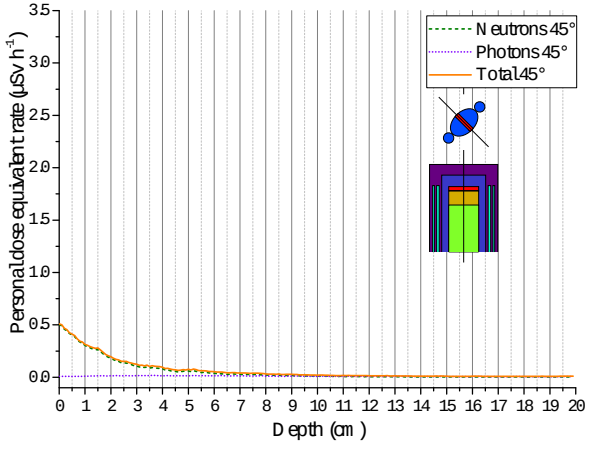

(e) Free In Air 45°

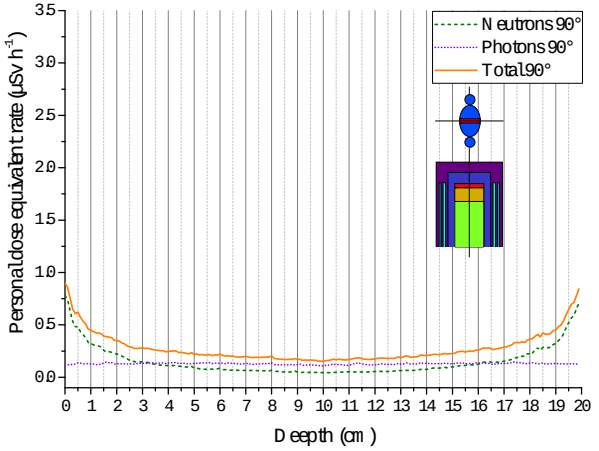

(f) Free In Air 90°

FIGURE A.17: Calculated evolution of $\dot{H}_p(d)$ dose for the body depth at 5 m to POLLUX-10 surface.

Appendix B

Nuclear waste inventory for the POLLUX® casks

B.1 Source composition

The following table presents the isotopic composition of the simulated Spent Nuclear Fuel (SNF) for each cask in MCNP6 and SCALE. Nuclide with an abundance lower than 1.0×10^{-4} % are not simulated since their impact on the overall behaviour of the emitted particles moving through the SNF can be neglected.

TABLE B.1: Percentage composition of the SNF disposed in each POLLUX® cask.

Material	POLLUX-10	POLLUX-3M	POLLUX-3U
	Spent Nuclear Fuel		
^{14}N	3.32×10^{-1}	6.46×10^{-1}	6.46×10^{-1}
^{16}O	1.42×10^{-1}	1.90×10^{-1}	1.89×10^{-1}
^{94}Zr	2.52×10^{-2}	7.57×10^{-3}	7.57×10^{-3}
^{96}Zr	4.06×10^{-3}	1.22×10^{-3}	1.22×10^{-3}
^{100}Mo	6.04×10^{-4}	1.82×10^{-4}	1.82×10^{-4}
^{102}Ru	0.00×10^{0}	0.00×10^{0}	1.60×10^{-4}
^{132}Xe	7.56×10^{-4}	2.28×10^{-4}	2.27×10^{-4}
^{134}Xe	9.82×10^{-4}	2.93×10^{-4}	2.96×10^{-4}
^{136}Xe	1.49×10^{-3}	4.27×10^{-4}	4.55×10^{-4}
^{133}Cs	6.82×10^{-4}	2.06×10^{-4}	2.04×10^{-4}
^{137}Ba	5.73×10^{-4}	1.72×10^{-4}	1.72×10^{-4}
^{138}Ba	8.34×10^{-4}	2.47×10^{-4}	2.52×10^{-4}

TABLE B.1: Percentage composition of the SNF disposed in each POLLUX® cask.

Material	POLLUX-10	POLLUX-3M	POLLUX-3U
^{139}La	7.76×10^{-4}	2.30×10^{-4}	2.35×10^{-4}
^{140}Ce	7.83×10^{-4}	2.30×10^{-4}	2.36×10^{-4}
^{142}Ce	7.17×10^{-4}	2.09×10^{-4}	2.17×10^{-4}
^{141}Pr	7.05×10^{-4}	2.09×10^{-4}	2.13×10^{-4}
^{144}Nd	8.69×10^{-4}	2.40×10^{-4}	2.70×10^{-4}
^{235}U	2.42×10^{-3}	6.34×10^{-4}	7.66×10^{-4}
^{236}U	2.02×10^{-3}	4.72×10^{-4}	6.64×10^{-4}
^{238}U	3.56×10^{-1}	1.06×10^{-1}	1.07×10^{-1}
^{239}Pu	3.06×10^{-3}	1.38×10^{-3}	7.24×10^{-4}
^{240}Pu	1.82×10^{-3}	1.02×10^{-3}	3.47×10^{-4}
^{242}Pu	6.32×10^{-4}	3.60×10^{-4}	0.00×10^{0}
^{241}Am	9.90×10^{-4}	5.39×10^{-4}	1.96×10^{-4}
Structural material			
^{90}Zr	7.47×10^{-2}	2.24×10^{-2}	2.24×10^{-2}
^{91}Zr	1.63×10^{-2}	4.89×10^{-3}	4.89×10^{-3}
^{92}Zr	2.49×10^{-2}	7.47×10^{-3}	7.47×10^{-3}

B.2 Radioactive emission probability

Tables with the emission probability for neutrons and gammas are listed below. Energy intervals are used for each neutron energy probability since neutrons have a continuous spectrum (Table B.2), while for photons, a discrete spectrum is simulated (Table B.3)

TABLE B.2: Calculated neutron emission probability for the SNF disposed in each POLLUX® cask type.

Energy range (MeV)		POLLUX-10	POLLUX-3M	POLLUX-3U
$<1.00 \times 10^{-6}$		0.00×10^{0}	0.00×10^{0}	0.00×10^{0}
1.0×10^{-6}	**2.0×10^{-5}**	4.89×10^{-8}	4.79×10^{-8}	4.81×10^{-8}
2.0×10^{-5}	**4.0×10^{-5}**	6.78×10^{-8}	6.72×10^{-8}	6.60×10^{-8}
4.0×10^{-5}	**6.0×10^{-5}**	1.15×10^{-7}	1.14×10^{-7}	1.13×10^{-7}
6.0×10^{-5}	**8.0×10^{-5}**	5.27×10^{-8}	5.23×10^{-8}	5.21×10^{-8}

TABLE B.2: Calculated neutron emission probability for the SNF disposed in each POLLUX® cask type.

Energy range (MeV)		**POLLUX-10**	**POLLUX-3M**	**POLLUX-3U**
$\mathbf{8.0 \times 10^{-5}}$	$\mathbf{1.0 \times 10^{-4}}$	1.49×10^{-7}	1.47×10^{-7}	1.46×10^{-7}
$\mathbf{1.0 \times 10^{-4}}$	$\mathbf{2.0 \times 10^{-4}}$	6.44×10^{-7}	6.36×10^{-7}	6.32×10^{-7}
$\mathbf{2.0 \times 10^{-4}}$	$\mathbf{4.0 \times 10^{-4}}$	1.94×10^{-6}	1.92×10^{-6}	1.91×10^{-6}
$\mathbf{4.0 \times 10^{-4}}$	$\mathbf{6.0 \times 10^{-4}}$	2.60×10^{-6}	2.57×10^{-6}	2.55×10^{-6}
$\mathbf{6.0 \times 10^{-4}}$	$\mathbf{8.0 \times 10^{-4}}$	3.03×10^{-6}	2.99×10^{-6}	2.97×10^{-6}
$\mathbf{8.0 \times 10^{-4}}$	$\mathbf{1.0 \times 10^{-3}}$	3.42×10^{-6}	3.38×10^{-6}	3.36×10^{-6}
$\mathbf{1.0 \times 10^{-3}}$	$\mathbf{2.0 \times 10^{-3}}$	2.19×10^{-5}	2.16×10^{-5}	2.15×10^{-5}
$\mathbf{2.0 \times 10^{-3}}$	$\mathbf{4.0 \times 10^{-3}}$	6.20×10^{-5}	6.12×10^{-5}	6.09×10^{-5}
$\mathbf{4.0 \times 10^{-3}}$	$\mathbf{6.0 \times 10^{-3}}$	8.04×10^{-5}	7.94×10^{-5}	7.89×10^{-5}
$\mathbf{6.0 \times 10^{-3}}$	$\mathbf{8.0 \times 10^{-3}}$	9.51×10^{-5}	9.39×10^{-5}	9.34×10^{-5}
$\mathbf{8.0 \times 10^{-3}}$	$\mathbf{1.0 \times 10^{-2}}$	1.08×10^{-4}	1.06×10^{-4}	1.06×10^{-4}
$\mathbf{1.0 \times 10^{-2}}$	$\mathbf{2.0 \times 10^{-2}}$	6.90×10^{-4}	6.82×10^{-4}	6.78×10^{-4}
$\mathbf{2.0 \times 10^{-2}}$	$\mathbf{4.0 \times 10^{-2}}$	1.94×10^{-3}	1.92×10^{-3}	1.91×10^{-3}
$\mathbf{4.0 \times 10^{-2}}$	$\mathbf{6.0 \times 10^{-2}}$	2.48×10^{-3}	2.46×10^{-3}	2.44×10^{-3}
$\mathbf{6.0 \times 10^{-2}}$	$\mathbf{8.0 \times 10^{-2}}$	2.91×10^{-3}	2.88×10^{-3}	2.86×10^{-3}
$\mathbf{8.0 \times 10^{-2}}$	$\mathbf{1.0 \times 10^{-1}}$	3.27×10^{-3}	3.23×10^{-3}	3.21×10^{-3}
$\mathbf{1.0 \times 10^{-1}}$	$\mathbf{2.0 \times 10^{-1}}$	2.04×10^{-2}	2.01×10^{-2}	2.00×10^{-2}
$\mathbf{2.0 \times 10^{-1}}$	$\mathbf{4.0 \times 10^{-1}}$	5.32×10^{-2}	5.25×10^{-2}	5.22×10^{-2}
$\mathbf{4.0 \times 10^{-1}}$	$\mathbf{6.0 \times 10^{-1}}$	6.19×10^{-2}	6.11×10^{-2}	6.07×10^{-2}
$\mathbf{6.0 \times 10^{-1}}$	$\mathbf{8.0 \times 10^{-1}}$	6.55×10^{-2}	6.46×10^{-2}	6.42×10^{-2}
$\mathbf{8.0 \times 10^{-1}}$	$\mathbf{1.0 \times 10^{0}}$	6.61×10^{-2}	6.52×10^{-2}	6.48×10^{-2}
$\mathbf{1.0 \times 10^{0}}$	$\mathbf{1.2 \times 10^{0}}$	6.48×10^{-2}	6.40×10^{-2}	6.37×10^{-2}
$\mathbf{1.2 \times 10^{0}}$	$\mathbf{1.4 \times 10^{0}}$	6.23×10^{-2}	6.16×10^{-2}	6.14×10^{-2}
$\mathbf{1.4 \times 10^{0}}$	$\mathbf{1.6 \times 10^{0}}$	5.89×10^{-2}	5.86×10^{-2}	5.84×10^{-2}
$\mathbf{1.6 \times 10^{0}}$	$\mathbf{1.8 \times 10^{0}}$	5.51×10^{-2}	5.50×10^{-2}	5.50×10^{-2}
$\mathbf{1.8 \times 10^{0}}$	$\mathbf{2.0 \times 10^{0}}$	5.11×10^{-2}	5.13×10^{-2}	5.15×10^{-2}
$\mathbf{2.0 \times 10^{0}}$	$\mathbf{2.2 \times 10^{0}}$	4.69×10^{-2}	4.75×10^{-2}	4.78×10^{-2}
$\mathbf{2.2 \times 10^{0}}$	$\mathbf{2.4 \times 10^{0}}$	4.29×10^{-2}	4.37×10^{-2}	4.42×10^{-2}
$\mathbf{2.4 \times 10^{0}}$	$\mathbf{2.6 \times 10^{0}}$	3.89×10^{-2}	3.99×10^{-2}	4.05×10^{-2}
$\mathbf{2.6 \times 10^{0}}$	$\mathbf{2.8 \times 10^{0}}$	3.51×10^{-2}	3.62×10^{-2}	3.68×10^{-2}
$\mathbf{2.8 \times 10^{0}}$	$\mathbf{3.0 \times 10^{0}}$	3.16×10^{-2}	3.26×10^{-2}	3.31×10^{-2}
$\mathbf{3.0 \times 10^{0}}$	$\mathbf{3.2 \times 10^{0}}$	2.83×10^{-2}	2.91×10^{-2}	2.96×10^{-2}
$\mathbf{3.2 \times 10^{0}}$	$\mathbf{3.4 \times 10^{0}}$	2.52×10^{-2}	2.59×10^{-2}	2.63×10^{-2}

TABLE B.2: Calculated neutron emission probability for the SNF disposed in each POLLUX® cask type.

Energy range (MeV)		**POLLUX-10**	**POLLUX-3M**	**POLLUX-3U**
$\mathbf{3.4 \times 10^0}$	$\mathbf{3.6 \times 10^0}$	2.24×10^{-2}	2.29×10^{-2}	2.32×10^{-2}
$\mathbf{3.6 \times 10^0}$	$\mathbf{3.8 \times 10^0}$	1.99×10^{-2}	2.02×10^{-2}	2.03×10^{-2}
$\mathbf{3.8 \times 10^0}$	$\mathbf{4.0 \times 10^0}$	1.76×10^{-2}	1.78×10^{-2}	1.78×10^{-2}
$\mathbf{4.0 \times 10^0}$	$\mathbf{4.2 \times 10^0}$	1.55×10^{-2}	1.55×10^{-2}	1.55×10^{-2}
$\mathbf{4.2 \times 10^0}$	$\mathbf{4.4 \times 10^0}$	1.37×10^{-2}	1.36×10^{-2}	1.35×10^{-2}
$\mathbf{4.4 \times 10^0}$	$\mathbf{4.6 \times 10^0}$	1.20×10^{-2}	1.18×10^{-2}	1.17×10^{-2}
$\mathbf{4.6 \times 10^0}$	$\mathbf{4.8 \times 10^0}$	1.05×10^{-2}	1.03×10^{-2}	1.02×10^{-2}
$\mathbf{4.8 \times 10^0}$	$\mathbf{5.0 \times 10^0}$	9.19×10^{-3}	9.03×10^{-3}	8.93×10^{-3}
$\mathbf{5.0 \times 10^0}$	$\mathbf{5.2 \times 10^0}$	8.02×10^{-3}	7.88×10^{-3}	7.79×10^{-3}
$\mathbf{5.2 \times 10^0}$	$\mathbf{5.4 \times 10^0}$	6.99×10^{-3}	6.87×10^{-3}	6.79×10^{-3}
$\mathbf{5.4 \times 10^0}$	$\mathbf{5.6 \times 10^0}$	6.08×10^{-3}	5.97×10^{-3}	5.90×10^{-3}
$\mathbf{5.6 \times 10^0}$	$\mathbf{5.8 \times 10^0}$	5.28×10^{-3}	5.19×10^{-3}	5.13×10^{-3}
$\mathbf{5.8 \times 10^0}$	$\mathbf{6.0 \times 10^0}$	4.59×10^{-3}	4.50×10^{-3}	4.44×10^{-3}
$\mathbf{6.0 \times 10^0}$	$\mathbf{6.2 \times 10^0}$	3.97×10^{-3}	3.90×10^{-3}	3.85×10^{-3}
$\mathbf{6.2 \times 10^0}$	$\mathbf{6.4 \times 10^0}$	3.44×10^{-3}	3.37×10^{-3}	3.33×10^{-3}
$\mathbf{6.4 \times 10^0}$	$\mathbf{6.6 \times 10^0}$	2.97×10^{-3}	2.92×10^{-3}	2.88×10^{-3}
$\mathbf{6.6 \times 10^0}$	$\mathbf{6.8 \times 10^0}$	2.57×10^{-3}	2.52×10^{-3}	2.48×10^{-3}
$\mathbf{6.8 \times 10^0}$	$\mathbf{7.0 \times 10^0}$	2.21×10^{-3}	2.17×10^{-3}	2.14×10^{-3}
$\mathbf{7.0 \times 10^0}$	$\mathbf{7.2 \times 10^0}$	1.91×10^{-3}	1.87×10^{-3}	1.85×10^{-3}
$\mathbf{7.2 \times 10^0}$	$\mathbf{7.4 \times 10^0}$	1.64×10^{-3}	1.61×10^{-3}	1.59×10^{-3}
$\mathbf{7.4 \times 10^0}$	$\mathbf{7.6 \times 10^0}$	1.41×10^{-3}	1.38×10^{-3}	1.37×10^{-3}
$\mathbf{7.6 \times 10^0}$	$\mathbf{7.8 \times 10^0}$	1.21×10^{-3}	1.19×10^{-3}	1.17×10^{-3}
$\mathbf{7.8 \times 10^0}$	$\mathbf{8.0 \times 10^0}$	1.04×10^{-3}	1.02×10^{-3}	1.01×10^{-3}
$\mathbf{8.0 \times 10^0}$	$\mathbf{8.2 \times 10^0}$	8.91×10^{-4}	8.75×10^{-4}	8.63×10^{-4}
$\mathbf{8.2 \times 10^0}$	$\mathbf{8.4 \times 10^0}$	7.64×10^{-4}	7.49×10^{-4}	7.39×10^{-4}
$\mathbf{8.4 \times 10^0}$	$\mathbf{8.6 \times 10^0}$	6.54×10^{-4}	6.42×10^{-4}	6.33×10^{-4}
$\mathbf{8.6 \times 10^0}$	$\mathbf{8.8 \times 10^0}$	5.59×10^{-4}	5.49×10^{-4}	5.41×10^{-4}
$\mathbf{8.8 \times 10^0}$	$\mathbf{9.0 \times 10^0}$	4.78×10^{-4}	4.69×10^{-4}	4.63×10^{-4}
$\mathbf{9.0 \times 10^0}$	$\mathbf{9.2 \times 10^0}$	4.08×10^{-4}	4.01×10^{-4}	3.95×10^{-4}
$\mathbf{9.2 \times 10^0}$	$\mathbf{9.4 \times 10^0}$	3.48×10^{-4}	3.42×10^{-4}	3.37×10^{-4}
$\mathbf{9.4 \times 10^0}$	$\mathbf{9.6 \times 10^0}$	2.97×10^{-4}	2.92×10^{-4}	2.88×10^{-4}
$\mathbf{9.6 \times 10^0}$	$\mathbf{9.8 \times 10^0}$	2.53×10^{-4}	2.49×10^{-4}	2.45×10^{-4}
$\mathbf{9.8 \times 10^0}$	$\mathbf{1.0 \times 10^{+1}}$	2.16×10^{-4}	2.12×10^{-4}	2.09×10^{-4}

TABLE B.2: Calculated neutron emission probability for the SNF disposed in each POLLUX® cask type.

Energy range (MeV)	**POLLUX-10**	**POLLUX-3M**	**POLLUX-3U**
$>1.00 \times 10^{1}$	0.00×10^{0}	0.00×10^{0}	0.00×10^{0}

TABLE B.3: Calculated gamma emission probability for the SNF disposed in each POLLUX® cask type.

Energy (MeV)	**POLLUX-10**	**POLLUX-3M**	**POLLUX-3U**
2.634×10^{-2}	4.18×10^{-3}	8.79×10^{-5}	2.84×10^{-3}
2.704×10^{-2}	1.08×10^{-3}	2.26×10^{-5}	7.31×10^{-4}
3.320×10^{-2}	2.09×10^{-4}	4.40×10^{-6}	1.42×10^{-4}
5.954×10^{-2}	6.20×10^{-2}	1.30×10^{-3}	4.20×10^{-2}
1.231×10^{-1}	1.74×10^{-3}	8.73×10^{-2}	1.63×10^{-3}
1.883×10^{-1}	1.00×10^{-5}	5.04×10^{-4}	9.40×10^{-6}
2.479×10^{-1}	2.98×10^{-4}	1.50×10^{-2}	2.79×10^{-4}
4.013×10^{-1}	8.32×10^{-6}	4.18×10^{-4}	7.79×10^{-6}
4.444×10^{-1}	2.43×10^{-5}	1.22×10^{-3}	2.27×10^{-5}
4.783×10^{-1}	9.63×10^{-6}	4.84×10^{-4}	9.01×10^{-6}
5.576×10^{-1}	1.15×10^{-5}	5.77×10^{-4}	1.08×10^{-5}
5.819×10^{-1}	3.81×10^{-5}	1.92×10^{-3}	3.57×10^{-5}
5.918×10^{-1}	2.14×10^{-4}	1.08×10^{-2}	2.00×10^{-4}
6.252×10^{-1}	1.37×10^{-5}	6.87×10^{-4}	1.28×10^{-5}
6.617×10^{-1}	9.26×10^{-1}	6.44×10^{-1}	9.48×10^{-1}
6.766×10^{-1}	6.33×10^{-6}	3.18×10^{-4}	5.93×10^{-6}
6.925×10^{-1}	7.71×10^{-5}	3.87×10^{-3}	7.21×10^{-5}
7.158×10^{-1}	7.84×10^{-6}	3.94×10^{-4}	7.34×10^{-6}
7.234×10^{-1}	8.67×10^{-4}	4.35×10^{-2}	8.11×10^{-4}
7.569×10^{-1}	1.95×10^{-4}	9.77×10^{-3}	1.82×10^{-4}
8.155×10^{-1}	2.20×10^{-5}	1.11×10^{-3}	2.06×10^{-5}
8.454×10^{-1}	2.53×10^{-5}	1.27×10^{-3}	2.37×10^{-5}
8.506×10^{-1}	1.03×10^{-5}	5.18×10^{-4}	9.66×10^{-6}
8.732×10^{-1}	5.23×10^{-4}	2.63×10^{-2}	4.89×10^{-4}
8.927×10^{-1}	2.20×10^{-5}	1.11×10^{-3}	2.06×10^{-5}
9.041×10^{-1}	3.83×10^{-5}	1.92×10^{-3}	3.58×10^{-5}

TABLE B.3: Calculated gamma emission probability for the SNF disposed in each POLLUX® cask type.

Energy (MeV)	**POLLUX-10**	**POLLUX-3M**	**POLLUX-3U**
$\mathbf{9.960 \times 10^{-1}}$	4.48×10^{-4}	2.25×10^{-2}	4.19×10^{-4}
$\mathbf{1.005 \times 10^{0}}$	7.71×10^{-4}	3.87×10^{-2}	7.21×10^{-4}
$\mathbf{1.118 \times 10^{0}}$	4.52×10^{-6}	2.27×10^{-4}	4.23×10^{-6}
$\mathbf{1.129 \times 10^{0}}$	1.34×10^{-5}	6.74×10^{-4}	1.26×10^{-5}
$\mathbf{1.141 \times 10^{0}}$	1.01×10^{-5}	5.07×10^{-4}	9.45×10^{-6}
$\mathbf{1.241 \times 10^{0}}$	5.73×10^{-6}	2.88×10^{-4}	5.36×10^{-6}
$\mathbf{1.246 \times 10^{0}}$	3.71×10^{-5}	1.86×10^{-3}	3.47×10^{-5}
$\mathbf{1.275 \times 10^{0}}$	1.51×10^{-3}	7.57×10^{-2}	1.41×10^{-3}
$\mathbf{1.494 \times 10^{0}}$	3.01×10^{-5}	1.51×10^{-3}	2.82×10^{-5}
$\mathbf{1.597 \times 10^{0}}$	7.72×10^{-5}	3.88×10^{-3}	7.22×10^{-5}

Appendix C

Curriculum Vitae

Professional experience

Oct. 2017 – present Project leader at Studsvik GmbH & Co. KG, Mannheim, Germany.

Mar. 2014 – Aug. 2017 Research assistant and doctoral student at the Institute for Nuclear Waste Disposal, headed by Prof. Dr. Horst Geckeis. Karlsruhe Institute of technology, Eggenstein-Leopoldshafen (Germany).

Academic background

Mar. 2014 – Feb. 2018 PhD Degree at the faculty of Mechanical Engineering, doctoral adviser Prof. Dr. Robert Stieglitz. Karlsruhe Institute of technology, Karlsruhe (Germany).
Thesis title: "Individual dosimetry in disposal facilities for high-level nuclear waste".

Sept. 2006 – Jun. 2013 Masters degree in mechanical engineering from the Polytechnic University of Valencia. Emphasis on energy and nuclear technologies.

Oct. 2012 – May 2013 Master thesis at the Institute for Neutron Physics and Reactor Technology, headed by Prof. Dr. Robert Stieglitz. Karlsruhe Institute of technology, Eggenstein-Leopldshafen (Germany).
Thesis title: "Analysis of the Oskarshamn-2 Boiling Water Reactor Instabilities with the Couple Code TRACE/-PARCS".

Appendix D

List of publications during the PhD thesis

Journal articles

Pang, B., Becker, F. and Saurí Suárez, H. (2016). "Monte Carlo based investigation of a universal two-component albedo neutron dosimeter in a deep geological disposal system for high-level nuclear waste". In: *Annals of Nuclear Energy* 98, pp. 81–90.

Pang, B., Saurí Suárez, H and Becker, F. (2016). "Individual Dosimetry in Disposal Repository of Heat-Generating Nuclear Waste". In: *Radiation Protection Dosimetry* 170 (1-4), pp. 387–392.

Pang, B., Saurí Suárez, H. and Becker, F. (2017). "Reference level of the occupational radiation exposure in a deep geological disposal facility for high-level nuclear waste: A Monte Carlo study". In: *Annals of Nuclear Energy* 110, pp. 258–264.

Saurí Suárez, H., Becker, F., Klix, A., Pang, B. and Döring, T. (2018). "Neutron flux measurements on a mock-up of a storage cask for high-level nuclear waste using 2.5 MeV neutrons". In: *Journal of Radiological Protection* 38.3, pp. 881–891.

Saurí Suárez, H., Pang, B., Becker, F. and Metz, V. (2017b). "Monte-Carlo based comparison of the personal dose for emplacement scenarios of spent nuclear fuel casks in generic deep geological repositories". In: *atw - International Journal for Nuclear Power* 62 (6), pp. 384–390.

Conference papers

Saurí Suárez, H, Pang, B. and Becker, F. (2015). *Monte-Carlo Calculations of the radiation field in a rock salt horizontal emplacement gallery of an underground nuclear waste disposal facility.* Berlin, Germany.

Saurí Suárez, H, Pang, B., Becker, F., Geckeis, H. and Stieglitz, R. (2016). *Monte-Carlo based study of the depth-dose rate curve for employees in an underground nuclear waste disposal facility.* Hamburg, Germany.

Saurí Suárez, H., Pang, B., Becker, F. and Metz, V. (2017a). *Monte-Carlo based comparison of the personal dose for emplacement scenarios of spent nuclear fuel canisters in generic rock salt and claystone repositories.* Berlin, Germany.

Bibliography

Albert, A. et al. (2010). *Bautabellen für Ingenieure mit Berechnungshinweisen und Beispielen*. Ed. by A. Goris. 19th ed. Schneider. ISBN: 978-3-8041-5242-7.

Allisy, A., Jennings, W. A., Kellerer, A. M. and Müller, J. W. (1993). "ICRU Report 51: Quantities and Units in Radiation Protection Dosimetry." In: *Journal of the International Commission on Radiation Units and Measurements* os26 (2).

Allisy, A., Jennings, W. A., Kellerer, A. M., Müller, J. W., Rossi, H. H. and Seltzer, S. M. (1998). "ICRU Report 60: Fundamental Quantities and Units for Ionizing Radiation". In: *Journal of the International Commission on Radiation Units and Measurements* os31 (1).

ANDRA (2001). *Sur l'avancement des études & recherches relatives a la faisabilit é d'un stockage de d échets à haute activit é et à la vie langue en formation profond*. Tech. rep. Agence nationale pour la gestion des déchets radioactifs (ANDRA).

Appel, D. et al. (2002). *Auswahlverfahren für Endlagerstandorte. Emphelungen des AkEnd- Arbeitskreis Auswahlverfahren Endlagerstandorte*. Tech. rep. Arbeitskreis Auswahlverfahren Endlagerstandorte (AkEnd).

Batchelor, R., Gilboy, W.B., Parker, J.B. and Towle, J.H. (1961). "The response of organic scintillators to fast neutrons". In: *Nuclear Instruments and Methods* 13, pp. 70–82.

Bates, E.A., Driscoll, M.J., Lester, R.K. and Arnold, B.W. (2014). "Can deep boreholes solve America's nuclear waste problem?" In: *Energy Policy* 72, pp. 186–189.

Behrens, R. (2010). "Uncertaintis in external dosimetry: Analytical Vs. Monte Carlo Method". In: *Radiation Protection Dosimetry* 138.4, pp. 346–352.

Bernnat, W. and Mattes, M. (1995). *Calculation of neutron and gamma spectra and dose-rates in the environment of the AHE-experimental cask in the ASSE salt mine.* Research rep. Institut für Kerntechnik. und Energie-Wandlung e.V. KE6-FB-74E.

Beswick, J. (2008). *Status of technology for deep borehole disposal*. Tech. rep. UK Nuclear Decommissioning Authority (NDA). EPS International Contract No NP 01185.

BFE (2008). *Sachplan Geologische Tiefenlager. Konzeptteil*. Tech. rep. Schweizerische Eidgenossenschaft. Bundesamt für Energie (BFE). COO.2207.110.4.847888.

Bishop, W.P. and Hollister, C.D. (1974). "Seabed Disposal - Where to Look". In: *Nuclear Technology* 24.3, pp. 425–443.

BMJV (2001). *Verordnung über den Schutz vor Schäden durch ionisierende Strahlen (Strahlenschutzverordnung - StrlSchV)*. Ed. by Bundesministerium der Justiz.

BMUB (2015). *Programm für eine verantwortungsvolle und sichere Entsorgung bestrahlter Brennelemente und radioaktive Abfälle. (Nationales Entsorgungsprogramm)*. Tech.

rep. Bundesministerium für Umwelt, Naturschutz, Bau und Reaktorsicherheit (BMUB). Berlin, Germany.

BMWi (2015). *Forschung zur Entsorgung radioaktiver Abfälle: Förderkonzept des BMWi (2015-2018)*. Tech. rep. Bundesministerium für Wirtschaft un Energie und Karlsruher Institut für Technologie. Germany.

Bollingerfehr, W., Filbert, W., Lerch, C. and Tholen, M. (2011). *Endlagerkonzepte. Bericht zum Arbeitspaket 5 Vorläufige Sicherheitsanalyse für den Standort Gorleben.* Gesellschaft für Anlagen und Reaktorsicherheit (GRS) GmbH. ISBN: 978-3-939355-48-9. GRS-272.

Bollingerfehr, W., Filbert, W. and Reinhold, G. (2009). "Entwicklungsstand der Endlagerung wärmeentwickelnder Abfälle in Deutschland am Beispiel der Optimierung der Direkten Endlagerung ausgedienter Brennelemente". In: *Energie und Rohstoffe 2009 - Sicherung der Energie und Rohstoffversorgung: Tagungsband 9. - 12. September 2009, Goslar*. Deutscher Markscheider-Verein e.V. ISBN: 978-3869480152.

Bollingerfehr, W., Herklotz, Martin et al. (2011). *Entwicklung und Umsetzung von technischen Konzepten für Endlager in tiefen geologischen Formationen in unterschiedlichen Wirtsgesteinen (EUGENIA). Synthesebericht*. Tech. rep. DBE TECHNOLOGY GmbH. FKZ 02 E 10346.

Booth, T. E. et al. (2003). *MCNP - A General Monte Carlo N-Particle Transport Code. Volume I: Overview and Theory*. Ed. by S.M. Girard. Version 5. LA-UR-03-1987.

Brandy, P.V., Arnold, B.W., Freeze, G.A., Swift, P.N., Bauer, S.J., Kanney, J.L, Rechard, R.P. and Stein, J.S (2009). *Deep Borehole Disposal of High-Level Radioactive Waste*. Tech. rep. Sandia National Laboratories. SAND2009-4401.

Brasser, T., Herbert, H.J., Miehe, R. and Schmidt, G. (2008). *Endlagerung wärmeentwickelnder radioaktiver Abfälle in Deutschland. Anhang Wirtsgesteine. Potenzielle Wirtsgesteine und ihre Eigenschaften*. Gesellschaft für Anlagen- und Reaktorsicherheit (GRS) GmbH and Institut für angewandte ökologie. ISBN: 978-3-939355-22-9.

Bräuer, V. et al. (2011). *Description of the Gorleben site Part 4: Geotechnical exploration of the Gorleben salt dome*. Ed. by Bundesanstalt für Geowissenschaften und Rohstoffe. Hannover: Schweizerbart Sche Vlgsb. ISBN: 978-3-510-95988-4.

Bräuner, V., Reh, M., Schulz, P., Schuster, P. and Sprado, K. H. (1994). *Endlagerung stark wärmeentwickelnder radioaktiver Abfälle in tiefen geologischen Formationen Deutschlands: Untersuchung und Bewertung von Regionen in nichtsalinaren Formationen*. Tech. rep. Bundesantstalt für Geowissenschaften und Rohstoffe (BGR). Schreiben BMFT Az. 316 - 5555 - 67 - 7/91.

Burns, R.E., Causey, W.E., Galloway, W.E. and Nelson, R.W. (1978). *Nuclear Waste Disposal in Space*. Tech. rep. National Aeronautics and Space Administration (NASA). NASA Technical Paper 1225.

Burrows, T.W. (1988). *The Program RADLST*. Tech. rep. Brookhaven National Laboratory. BNL-NCS-52142.

Camberra (2016). *PIPS®*. URL: http://www.canberra.com/products/detectors/pdf/passivated%5C_pips%5C_C39313a.pdf (visited on 25/03/2017).

Chadwick, M.B. et al. (2011). "ENDF/B-VII.1 Nuclear Data for Science and Technology: Cross Sections, Covariances, Fission Product Yields and Decay Data". In: *Nuclear Data Sheets* 112 (12), pp. 2887–2996.

Chapman, N. and McCombie, C. (2014). "Towards a european regional geological repository". In: *Proceedings of the 15th International Conference on Environmental Remediation and Radioactive Waste Management ICEM2013*. Vol. I. American Society of Mechanical Engineers,U.S. ISBN: 978-0-7918-5601-7. Brussels.

Chen, L., Duveau, G., Poutrel, A., Jia, Y., Shao, J. F. and Xie, N. (2014). "Numerical study of the interaction between adjacent galleries in a high-level radioactive waste repository". In: *International Journal of Rock Mechanics and Mining Sciences* 71, pp. 405–417.

Comité Européen de Normalisation (2013). *EN 10149: Hot rolled flat products made of high yield strength steels for cold forming - Part 2: Technical delivery conditions for thermomechanically rolled steels*.

The Antartic Treaty (1959). National Academies Press. ISBN: 978-0-309-12720-2.

DBE-Tec (2016). *Flächenbedarf für Endlager für wärmeentwickelnde radioaktive Abfälle. Gutachten für Kommission Lagerung hoch radioaktiver Abfallstoffe, Kommissionsdrucksache K-MAT58*. Tech. rep. DBE TECHNOLOGY GmbH. TEC-09-216-G.

Drosg, M. (2017). *DROSG-2000: Neutron Source Reactions. Data files with computer codes for 59 accelerator-based two-body neutron source reactions*. Rev.9. International Atomic Energy Agency. IAEA-NDS-87.

Eckerman, K. F., Westfall, R. J., Ryman, J. C. and Cristy, M. (1994). "Availability of Nuclear Decay Data in Electronic Form, Including Beta Spectra Not Previously Published." In: *Health Physics* 64 (4), pp. 338–345.

Erhard, M., Sauvan, P. and Nolte, R. (2014). "Simulation of neutron production using MCNPX+MCUNED". In: *Radiation Protection Dosimetry* 161, pp. 1–4.

Filbert, W., Engelmann, H.J., Heda, M. and Neydek, J. (1995). *Direkte Endlagerung ausgedienter Brennelemente (DEAB) - Handhabungsversuche zur Streckenlagerung*. Tech. rep. 60. Deutsche Gesellschaft für den Bau und Betrieb von Endlagern für Abfallstoffe mbH (DBE).

Filbert, W., Tholen, M., Engelmann, H.J., Graf, R. and Brammer, K. J. (2011). "Disposal of Spent Fuel from German Nuclear Power Plants: The Third Option - Disposal of Transport and Storage Casks (Status)". In: *Proceedings of the WM2011 Conference*. Phoenix, U.S. ISBN: 978-0-9836186-0-7.

FZKA (2008). *40 Jahre Forschung und Entwicklung für die sichere Endlagerung hochradioaktiver Abfälle: Wo stehen wir?* Research rep. 11. Forschungszentrum Karlsruhe in der Helmholtz-Gemeinschaft (FZKA).

Geckeis, H. and Kienzler, B. (2012). *Arbeitspaket Individuelle Dosimetrie für Beschäftigte in Entsorgungsanlagen In: Vorhabensbeschreibung zur Bildung einer Forschungsplattform Entsorgungsoptionen für radioaktive Reststoffe: Interdisziplinäre Analysen und Entwicklung von Bewertungsgrundlagen.* Research rep. Niedersächsische Technische Hochschule, Braunschweig, Clausthal-Zellerfeld, Hannover.

Gens, A., Sanchez, M., L.D.N., Guimarães, Alonso, E.E., Lloret, A., Olivella, S., Villar, M.V. and Huertas, F. (2009). "A full-scale in situ heating test for high-level nuclear waste disposal: observations, analysis and interpretation". In: *Géotechnique* 59 (4), pp. 377–399.

Goorley, J.T. et al. (2013). *MCNP6^{TM} User's Manual Version 1.0.* Ed. by D.B. Pelowitz. LA-CP-13-00634, Rev. 0.

Guldbakke, M., Klein, H., Meister, A., Scheler, U., Unholzer, S., Pulpan, J. and Tichy, M. (1994). "Response Matrices of NE213 Scintillation Detectors for Neutrons". In: Farrar, H., Lippincott, E.P., Williams, J.G. and Vehar, D.W. *Reactor Dosimetry.* Astm Intl, pp. 280–289. ISBN: 978-0-8031-1899-7.

Hammer, J., Sönnke, J. and Mingerzahn, G. (2009). *EUGENIA Teil I: Grundlagen und Beispiele für Standortauswahlverfahren für HAW-Endlager in unterschiedlichen Wirtsgesteinstypen.* Tech. rep. Bundesland für Geowissenschaften und Rohstoffe (BGR). BMWi 9Y3215080000.

Hardy Stevenson and Associates Limited (2008). *The art of Nuclear Waste Management.* URL: https://hardystevensoninsights.com/2011/05/05/the-art-of-nuclear-waste-management/ (visited on 25/06/2017).

Helton, J. C. and Davis, F. J. (2002). "Illustration of Sampling-Based Method for Uncertainty and Sensitivity Analysis". In: *Risk Analysis* 22 (3), pp. 591–622.

Heuze, F.E. (1981). *On the Geotechnical Modeling of High-Level Nuclear Waste Disposal by Rock Melting.* Research rep. Lawrence Livermore Laboratory. University of California. UCRL-53183.

Hinga, K.R., G.R., Heath, Anderson, R. and Hollister, C. (1982). "Disposal of high-level radioactive wastes by burial in the sea floor". In: *Environmental Science & Technology* 16.1, pp. 28–37.

Hollister, C.D, Anderson, R. and Heath, G. R. (1981). "Subseabed Disposal of Nuclear Waste". In: *Science* 213.4514, pp. 1321–1326.

Hoth, P., Wirth, H., Reinhold, K., Bräuer, V., Krull, P. and Feldrappe, H. (2007). *Endlagerung radioaktiver Abfälle in tiefen geologischen Formationen Deutschlands: Untersuchung und Bewertung von Tongesteinsformationen.* Research rep. Bundesantstalt für Geowissenschaften und Rohstoffe (BGR).

HSK (2007). *Sachplan geologische Tiefenlager. Herleitung, Beschreibung und Anwendung der sicherheitstechnischen Kriterien für die Standortevaluation.* Tech. rep. Schweizerische Eidgenossenschaft. Hauptabteilung für die Sicherheit der Kernanlagen (HSK). HSK 33/001.

IAEA (1996). *Manual for Troubleshooting and Upgrading of Neutron Generators.* Ed. by International Atomic Energy Agency (IAEA). IAEA-TECDOC-913.

— (2003). *The Long Term Storage of Radioactive Waste: Safety and Sustainability. A Position Paper of International Experts.* Tech. rep. International Atomic Energy Agency (IAEA). IAEA-LTS/RW.

— (2010). *Classification Of Radioactive Waste - General Safety Guide: IAEA Safety Standards Series No. GSG-1.* International Atomic Energy Agency. ISBN: 978-92-0-109209-0.

ICRP (1997). *ICRP Publication 74: Conversion Coefficients for use in Radiological Protection against External Radiation.* SAGE Publications Ltd. ISBN: 978-0080427393.

— (2007). *ICRP Publication 103: Recommendations of the ICRP (Annals of the ICRP).* SAGE Publications Ltd. ISBN: 978-0702030482.

— (2012). *ICRP Publication 118: ICRP Statement on Tissue Reactions and Early and Late Effects of Radiation in Normal Tissues and Organs - Threshold Doses for Tissue Reaction in a Radiation Protection Context (Annals of the ICRP).* SAGE Publications Ltd. ISBN: 978-0702052279.

International Convention on the Prevention of Marine Pollution by Dumping of Wastes and Other Matter (1972).

Itasca Consulting Group Inc. (2009). *Flac3D Version 4.0. User's Guide.* Minneapolis, USA.

Janberg, K. and Spilker, H. (1998). "Status of the development of final disposal casks and prospects in Germany". In: *Nuclear Technology* 121, pp. 136–147.

Kastelein, J. and Codée, H.D.K (2005). "HABOG: One building for all high level waste and spent fuel in the Netherlands. The first year of experience". In: *European Research Reactor Conference (RRFM)*, pp. 174–180.

Kearns, J.J. (1967). "Terminal solubility and partitioning of hydrogen in the alpha phase of zirconium, Zircaloy-2 and Zircaloy-4". In: *Journal of Nuclear Materials* 22 (3), pp. 292–303.

Kellett, M. A., Bersillon, O. and Mills, R. W. (2009). *The JEFF-3.1/-3.1. 1 radioactive decay data and fission yields sub-libraries.* JEFF Report 20. Nuclear Energy Agency.

Kikuchi, M., Lackner, K and Quang Tran, M. (2012). *Fusion Physics.* International Atomic Energy Agency. ISBN: 978-92-0-130410-0.

Klix, A., Domula, A., Fischer, U., Gehre, D., Pereslavtsev, P. and Rovni, I. (2011). "Test facility for a neutron flux spectrometer system based on the foil activation technique

for neutronics experiments with the ITER TBM". In: *Fusion Engineering and Desing* 86, pp. 2322–2325.

Kockel, F., Krull, P., Fischer, M., Frisch, U., Heßmann, W. and Stiewe, H. (1995). *Endlagerung stark wärmeentwickelnder radioaktiver Abfälle in tiefen geologischen Formationen Deutschlands: Untersuchung und Bewertung von Salzformationen*. Tech. rep. Bundesanstalt für Geowissenschagten und Rohstoffe (BGR). Archive No. Hannover 111089.

Kursten, B., Smailos, E., Azkarate, I., Werme, L., Smart, N.R. and Santarini, G. (2003). *COBECOMA State of the art document on the COrrosion BEhaviour of COntainer MAterials. Final Report*. Tech. rep. EUROPEAN COMMISSION 5th EURATOM FRAMEWORK PROGRAMME 1998-2002. CONTRACT Nr. FIKW-CT-20014-20138.

LANS (2010). *A General Monte Carlo N-Particle (MCNP) Transport Code*. Los Alamos National Security (LANS). URL: https://mcnp.lanl.go (visited on 22/04/2017).

Leon Vargas, R., Stahlmann, J. and Mintzlaff, V. (2017). "Thermal impact in the geometrical settings in deep geological repositories for HLW with retrievability and monitoring". In: *16th International High-Level Radioactive Waste Management Conference, IHLRWMC2017*, pp. 664–670. ISBN: 978-1-51-084654-8.

Logan, S.E. (1974). "Deep Self-Burial of radioactive Wasters by Rock-Melting Capsules". In: *Nuclear Technology* 21.2, pp. 111–124.

Lurie, N., Harris, L. and Young, J.C. (1975). "Calculation of gamma-ray respose matrix for 5 cm NeE-213 organic liquid scintillation detector". In: *Nuclear Instruments and Methods* 129, pp. 543–555.

Macfarlane, A.M. and Ewing, R.C. (2006). *Uncertainty Underground Yucca Mountain and the Nation's High-Level Nuclear Waste*. The MIT Press. ISBN: 978-0-26-263332-1.

Nagra (2002). *Projekt Opalinuston. Synthese der geowissenschaftlichen Untersuchungsergebnisse. Entsorgungsnachweis für abgebrannte Brennelemente, verglaste hochaktive sowie langlebige mittelaktive Abfälle*. TECHNISCHER BERICHT 02-03.

Nakagawa, Tsuneo et al. (1995). "Japanese Evaluated Nuclear Data Library Version 3 Revision-2: JENDL-3.2". In: *Journal of Nuclear Science and Technology* 32 (12), pp. 1259–1274.

National Research Council (1996). *The Waste Isolation Pilot Plant: A Potential Solution for the Disposal of Transuranic Waste*. National Academies Press. ISBN: 978-0-309-05491-1.

Neerdaela, B. and Boyazisb, J.P. (1998). "The Belgium underground research facility. Status on the demonstration issues for radioactive waste disposal in clay". In: *Nuclear Engineering and Design* 176 (1-2), pp. 89–96.

Nucleonica (2014). *Nucleonica Nuclear Science Portal (www.nucleonica.com) Version 3.0.49*. Nucleonica GmbH. Karlsruhe, Germany.

Peiffer, F., McStocker, B., Gründler, D., Ewig, F., Thomauske, B., Havenith, A. and Kettler, J. (2011). *Abfallspezifikation und Mengengerüst, Basis Ausstieg aus der Kernenergienutzung. Bericht zum Arbeitspaket 3 Vorläufige Sicherheitsanalyse für den Standort Gorleben*. Tech. rep. Gesellschaft für Anlagen und Reaktorsicherheit (GRS) mbH. GRS-278.

Philberth, B. (1961). "Beseitigung radiöaktiver Abfallsubstanzen in den Eiskappen der Erde". In: *Schweizerische Zeitschrift für Hydrologie* 23.1, pp. 263–284.

Philberth, K. (1977). "The Disposal of Radioactive Waste in Ice Sheets". In: *Journal of Glaciology* 19.81, pp. 607–617.

Powering the Grid (2011). *Spain new HLW. Location: Villar de Cañas (Cuenca)*. URL: https://poweringthegrid.wordpress.com/2011/12/31/spains-new-hlw-location-villar-de-canas-cuenca/ (visited on 25/05/2017).

Pusch, Roland, Ramqvist, Gunnar, Knutsson, Sven and Yang, Ting (2015). "The Role of Crystalline Rock for Disposal of High-Level Radioactive Waste (HLW)". In: *Procedia Earth and Planetary Science* 15, pp. 526–535.

Rao, K.R. (2001). "Radioactive waste: The problem and its management". In: *Current Science* 81.12, pp. 1534–1546.

Rearden, B. T. and Jessee, M. A., eds. (2016). *SCALE Code System. Version 6.2*.

Reed, A. L. (2007). *Medical physics calculations with MCNP: A primer*. Tech. rep. Los Alamos National Laboratory. LA-UR-07-4133.

Reginatto, M., Wiegel, B., Zimbal, A. and Langner, F. (2004). *UMG package, version 3.3*.

Röhlig K.J. amd Walther, C. et al. (2014). *Entsorgungsoptionen für radioaktive Reststoffe: Interdisziplinäre Analysen und Entwicklung von Bewertungsgrundlagen (ENTRIA) Memorandum zur Entsorgung hochradiaktiver Reststoffe*.

Ruby, L. and Crawford, R.B. (1963). "Anisotropy Factors for the Determination of Total Neutron Yield from the D(d,n)He^3 and T(d,n)He^4 Reactions". In: *Nuclear Instruments and Methods* 24, pp. 413–417.

Rybalchenkoa, A.I., Pimenova, M.K., Kurochkina, V.M., Kamneva, E.N., Korotkevichb, V.M., Zubkovb, A.A. and Khafizovc, R.R. (2005). "Deep Injection Disposal of Liquid Radioactive Waste in Russia, 1963-2002: Results and Consequences". In: *Developments in Water Science* 52, pp. 13–19.

Scherzinger, J. et al. (2017). "The light-yield response of a NE-213 liquid-scintillator detector measured using 2-6 MeV tagged neutrons". In: *Nuclear Instruments and Methods in Physics Research Section A: Accelerators, Spectrometers, Detectors and Associated Equipment* 840, pp. 121–127.

Schön, J.H. (2011). *Physical Properties of Rock. A Workbook.* Vol. 8. ISBN: 978-0-44-453796-6.

Shultis, J.K and Faw, R.E. (2010). *An MCNP primer.* Tech. rep. Dept. of Mechanical and Nuclear Engineering Kansas State Universtity.

Siebert, B.R.L. and Schuhmacher, H. (1995). "Quality factors, ambient and personal dose equivalent for neutrons, based on the new ICRU stopping power data for protons and alpha particles". In: *Radiation Protection Dosimetry* 58, pp. 177–183.

Smailos, E., Schwarzkopf, W., Gago, J.A. and Azkarate, I. (1992). *Corrosion Studies on Selected Packaging Materials for Disposal of Heat-Generating Radioactive Wastes in Rock-Salt Formations.* Tech. rep. Insitut für Nukleare Entsorgungstecknik, Kernforschungszentrum Karlsruhe. KfK 5011.

Stahlmann, J., Leon Vargas, R. and Mintzlaff, V. (2015). *Generische Tiefenlagermodelle mit Option zur Rückholung der radioaktiven Reststoffe: Geologische und Geotechnische Aspekte für die Auslegung.* Research rep. TU-Braunschweig, Institut für Grundbau und Bodenmechanik, Germany.

StandAG (2017). *Gesetz zur Suche und Auswahl eines Standortes für ein Endlager für hochradioaktive Abfälle (Standortauswahlgesetz - StandAG).* BGBl. I S. 1074.

Thomauske, B.R. (2002). "Interim Storage of spent nuclear fuel in Germany: Situation, State of Licensing Procedure, Prospects". In: *Proceedings of Waste Management Conference.* Tucson USA.

U.S. Department of Energy (2014). *Assessment of Disposal Options for DOE-Managed High-Level Radioactive Waste and Spent Nuclear Fuel.* Tech. rep. United States of America. Department of Energy.

— (2015). *Bottle Manikin Absorption (BOMAB) Phantoms.* U.S. Department of Energy. URL: http://www.id.energy.gov/resl/phantom/bomab.html (visited on 01/09/2015).

Uyeda, S. (1984). "Subduction Zones: Their Diversity, Mechanism and Human Impacts". In: *GeoJournal* 4.8, pp. 381–406.

Vana, N., Hajek, M. and Berger, T. (2003). "Ambient dose equivalent H(d) An appropriate philosophy for radiation monitoring onboard aircraft and in space". In: *IRPA Regional Congress on Radiation Protection in Central Europe*, pp. 252–255. ISBN: 978-80-88806-43-1.

Wiarda, D., Dunn, M.E., Greene, N.M., Williams, M.L., Celik, C. and Petrie, L.M. (2016). *AMPX-6: A Modular Code System for Processing ENDF.*

Wilson, W.B. et al. (2002). *SOURCES 4C: A Code for Calculating (alpha,n), Spontaneous Fission, and Delayed Neutron Sources and Spectra.* Ed. by W.B. Wilson. American Nuclear Society / Radiation Protection and Shielding Division.

World Nuclear Association (2017). *Storage and Disposal of Radioactive Wastes.* Ed. by World Nuclear Association. URL: http://www.world-nuclear.org/information-

library/nuclear-fuel-cycle/nuclear-wastes/storage-and-disposal-of-radioactive-wastes.aspx (visited on 29/06/2017).

Zhang, Guoqing (2011). "Monte Carlo Simulation of Mixed Neutron-Gamma Radiation Fields and Dosimetry Devices". PhD thesis. Karlsruher Instituts für Technologie (KIT).